CCD operation and long-range coupling of spins in quantum dot arrays

Baart, Tim

DOI
10.4233/uuid:b82047dd-0a7b-4e1b-9d53-d6704d4eb616

Publication date
2016

Document Version
Final published version

Citation (APA)
Baart, T. (2016). *CCD operation and long-range coupling of spins in quantum dot arrays*. [Dissertation (TU Delft), Delft University of Technology]. https://doi.org/10.4233/uuid:b82047dd-0a7b-4e1b-9d53-d6704d4eb616

Important note
To cite this publication, please use the final published version (if applicable).
Please check the document version above.

CCD operation and long-range coupling of spins in quantum dot arrays

Baart, Tim

DOI
10.4233/uuid:b82047dd-0a7b-4e1b-9d53-d6704d4eb616

Publication date
2016

Document Version
Final published version

Citation (APA)
Baart, T. (2016). *CCD operation and long-range coupling of spins in quantum dot arrays*.
https://doi.org/10.4233/uuid:b82047dd-0a7b-4e1b-9d53-d6704d4eb616

CCD OPERATION AND LONG-RANGE COUPLING OF SPINS IN QUANTUM DOT ARRAYS

CCD OPERATION AND LONG-RANGE COUPLING OF SPINS IN QUANTUM DOT ARRAYS

Proefschrift

ter verkrijging van de graad van doctor
aan de Technische Universiteit Delft,
op gezag van de Rector Magnificus prof. ir. K.C.A.M. Luyben,
voorzitter van het College voor Promoties,
in het openbaar te verdedigen op maandag 23 mei 2016 om 12:30 uur

door

Timothy Alexander BAART

Ingenieur in de technische natuurkunde,
geboren te Rotterdam, Nederland

Dit proefschrift is goedgekeurd door de

promotor: Prof. dr. ir. L.M.K. Vandersypen

Samenstelling promotiecommissie:

Rector Magnificus,	voorzitter
Prof. dr. ir. L.M.K. Vandersypen,	Technische Universiteit Delft
Onafhankelijke leden:	
Prof. dr. ir. R. Hanson	Technische Universiteit Delft
Prof. dr. ir. K.L.M. Bertels	Technische Universiteit Delft
Prof. dr. J.M. van Ruitenbeek	Universiteit Leiden
Prof. dr. M.A. Eriksson	University of Wisconsin-Madison
Prof. dr. D. DiVincenzo	Aachen University

Printed by: Gildeprint

Front: Artist impression by Alex de Mulder

Back: Atomic-force-microscopy image measured by Delphine Brousse

Casimir PhD Series, Delft-Leiden 2016-12

ISBN 978-90-8593-254-3

An electronic version of this dissertation is available at
`http://repository.tudelft.nl/`.

CONTENTS

SUMMARY

This thesis describes a set of experiments aimed at controlling arrays of single electrons. Nowadays it is possible to capture and position single electrons at well-defined locations. Knowledge about the behaviour of electrons is an essential concept to describe and predict a rich variety of phenomena such as electricity, magnetism, chemical bonds, thermal conductivity and superconductivity. Not all details of these phenomena are yet understood, and this makes electrons a very interesting and relevant research topic.

There exist several ways to capture electrons, and in this thesis we focus on creating so-called quantum dots in a semiconductor host material (GaAs). We start with a wafer that consists of a thick layer of GaAs, and on top, a very thin layer of ~100 nm of AlGaAs. Due to different material properties of the two alloys, the interface of these two materials is an attractive place for electrons to reside. As a consequence, we end up with a two-dimensional sea full of electrons that is also referred to as a two-dimensional electron gas (2DEG). In order to end up with only a few electrons, we pattern metallic gates on top of the wafer. By applying negative voltages to these gates we can repel all the electrons from the 2DEG that are not required. Ideally, one can in this way end up with a single electron at the desired location. Such a confined region is called a quantum dot. It is currently possible in our lab to position up to ~4 of these quantum dots in a row, thereby creating an artificial chain of electrons. Such arrays form the starting point of most experiments described in this thesis.

It is already remarkable that it is possible to position single electrons. On top, we can also control and measure the tiny magnetic moment that an electron possesses: its 'spin'. This spin can either point parallel ('up'), or anti-parallel ('down') to the external magnetic field. This spin is not only a necessary concept to understand for example magnetism, it can also be envisioned as a useful asset for the purpose of a new form of computing. The spin state of an electron can be used a computational bit by assigning the bit value '0' to spin-up, and '1' to spin-down. Due to quantum mechanics, the laws of physics for objects at the small length-scale, an electron can even be spin-up and spin-down at *same* time (a so-called 'superposition'). Making use of this principle can give rise to an exponential increase in computational power using spins as quantum bits (qubits).

The first experiment in this thesis is aimed at reading-out and controlling the spin state of three electrons. The magnetic moment of an electron spin is too small to conveniently be measured directly. As a solution, a technique has been devised in 2004 that converts the spin information into charge information (spin-to-charge conversion). A change in charge is more practical to distinguish. When a quantum dot is tuned to the so-called 'read-out position', a spin-down electron has sufficient energy to leave the dot, whilst a spin-up electron stays inside the dot. A nearby charge sensor can detect whether an electron left or not. This technique requires that the 'read-out' occurs close to a charge sensor and in the vicinity of a reservoir where electrons can tunnel towards. It is impractical to position a charge sensor and reservoir close to every quantum dot. It

would be much better if instead the spins could be transferred towards the charge sensor. This approach is very similar to the way a classical charge-coupled-device (CCD) operates: a CCD has only one charge sensor to determine the content of each of the pixels (each pixel containing multiple electrons as the information carrier). In analogy to a bucket-brigade, it passes the contents of each pixel one by one to the charge sensor. This technology has allowed the creation of CCDs that can read out millions of pixels. In this experiment we have created a prototype CCD that operates at the *single* electron level, including the preservation of the spin-state: the Single-spin CCD. We demonstrate that it is indeed possible to sequentially read-out the three electrons spins by shuttling them one by one to the dot closest to the charge sensor. We report read-out of three spins with fidelities of 97% on average. Using electric-dipole spin resonance techniques, we could also selectively flip the spin state in each of the three dots, thereby writing the pixels of Single-spin CCD. This device was relatively small so it was hard to distinguish whether shuttling an electron influenced its spin state. To probe what would happen in larger arrays, we shuttled a single electron back and forth many times inside the triple-dot array. Up to 500 hops, equivalent to a distance of 80 μm, we observe negligible influence on the spin projection. The high fidelity with which the spin projection can be preserved upon shuttling between dots thus allows scaling the Single-Spin CCD concept to linear arrays of hundreds of dots. Suggestions are proposed to increase the read-out fidelities for larger arrays.

With the capability of reading out the triple-dot array, it was possible in the second experiment to study and control the behaviour of two distant spins inside a triple-dot array. We positioned one electron in each of the outer dots of the array, and left the middle dot unoccupied. At first sight one would not expect any interaction between these two distant spins. However, due to the superexchange mechanism the electrons can still interact by 'virtually' hopping to one another and back. In quantum dot systems we can tune how much of the electron wavefunction 'leaks' out into the neighbouring dot, this is described by the tunnel coupling. As a consequence, the left (right) electron can actually occupy the center dot for a short while and jump all the way to the right (left) electron and back. The rate of this co-tunneling process is strongly influenced by the nearest-neighbour tunnel couplings, and by how far detuned the middle-dot energy level is. Such long-range quantum coherence between distant spins allows one to perform a two-qubit gate at a distance, and it turns out that such non-nearest neighbour interactions are also an important feature to understand for example high-temperature superconductivity and the response of a DNA molecule to oxidative stress. In this experiment we have created a mixture of the anti-parallel spin state up-down and the parallel state up-up. Under influence of the superexchange mechanism the anti-parallel state will evolve into the state down-up and keep on oscillating between up-down and down-up. The parallel state will remain unchanged. We indeed report such oscillations for the anti-parallel spin state and measure the frequency of oscillations as a function of the middle dot detuning. This work provides a first experimental demonstration of strong coherent spin-spin coupling between two distant spins using a quantum mediator (the empty middle dot).

For the experiments described so far, tweaking the required voltages for the gates to capture single electrons was done by hand. This is a time-consuming process and

should ideally be automated in order to scale up this system. In the third experiment we designed a computer algorithm that is capable of capturing two electrons next to each other in a double dot with only minimal user input. The algorithm is benchmarked by creating three double dots inside a quadruple-dot array. At the end of the algorithm the system analyzes the data and concludes whether the single-electron regime has been attained. In the experiments described in this thesis the algorithm was successful for all three double dots. This provides a promising first step to automate the tuning of larger arrays. Future algorithms should also focus on setting the right dot parameters such as the tunnel coupling with neighbouring dots.

The fourth experiment is a continuation of the Single-spin CCD-experiment to demonstrate that it is possible to shuttle electrons throughout the array within the time the quantum information is preserved. The eventual goal is to be able to conserve a superposition spin state as it is being shuttled during the course of a quantum computation. The experiment is performed in a slightly larger system, a quadruple instead of a triple dot, and the tunnel couplings between neighbouring dots have been set to higher values. This allows us to demonstrate a spin shuttle of a single-electron spin from one side of the array to the other at high speed. The experiment indicates that we managed to shuttle an electron within at most 150 ns through the array. This upper bound is limited by the relaxation time in a so-called 'hot spot'. We have no clear indications that shuttling on a faster timescale of 3 ns induces errors, indicating that a coherent transfer could already be feasible in this system where the dephasing time is reported to be ~20 ns. In each case, 150 ns is fast enough in different host materials such as Si of Si/SiGe where this shuttling technique could in principle also be applied.

In the last part of this thesis concluding remarks are made and future steps are proposed.

Tim Baart

SAMENVATTING

Dit proefschrift beschrijft een verzameling experimenten welke gericht is op het gecontroleerd besturen van rijtjes enkele elektronen. Tegenwoordig is het mogelijk om enkele elektronen te vangen en te positioneren op goed gedefinieerde locaties. Kennis over het gedrag van elektronen is essentieel om een reeks aan fenomenen te beschrijven en te voorspellen. Voorbeelden zijn elektriciteit, magnetisme, chemische verbindingen, thermische geleiding en supergeleiding. Niet alle details van deze fenomenen zijn bekend, en om die reden zijn elektronen een zeer interessant en relevant onderzoeksonderwerp.

Er zijn verschillende methodes om elektronen te vangen, en in dit proefschrift concentreren we ons op het creëren van zogenaamde 'kwantum dots' in een halgeleider materiaal (GaAs). We beginnen met een wafer welke bestaat uit een dikke laag GaAs, waar vervolgens een heel dunne laag van ~100 nm AlGaAs op wordt gegroeid. Door de verschillende materiaaleigenschappen van deze twee legeringen, is het scheidingsvlak van de twee materialen een aantrekkelijke plek voor elektronen om te verblijven. Als gevolg daarvan ontstaat er een tweedimensionale zee vol met elektronen welke ook wel een tweedimensionaal elektron gas wordt genoemd (2DEG). Om ervoor te zorgen dat we slechts met een paar elektronen eindigen, plaatsen we metallische pootjes ('gates') bovenop de wafer. Door negatieve spanningen aan te sluiten op de deze gates kunnen we alle elektronen wegduwen uit het 2DEG welke we niet nodig hebben. In het ideale geval kan men op deze manier een enkel elektron vangen op de gewenste locatie. Men noemt zo'n gebied waar een elektron gevangen wordt een 'kwantum dot'. Het is in ons lab tegenwoordig mogelijk om ~4 kwantum dots op een rij te maken waardoor effectief een kunstmatige ketting van elektronen wordt gevormd. Zulke rijtjes vormen het beginpunt van de meeste experimenten in dit proefschrift.

Het is al noemenswaardig dat het mogelijk is om enkele elektronen nauwkeurig te plaatsen. Het is daarnaast mogelijk om het kleine magnetische moment van een elektron, zijn 'spin', te controleren en te meten. Deze spin kan parallel ('up') of anti-parallel ('down') aan het externe magneetveld staan. De spin is niet alleen een noodzakelijk concept om begrippen als magnetisme te begrijpen, het kan ook worden gezien als een waardevolle toevoeging om een nieuw type computer te maken. De spin toestand van een elektron kan gebruikt worden als computer bit door het toekennen van de bit waarde '0' aan spin-up, en '1' aan spin-down. Door de kwantummechanica, de wetten van de natuurkunde voor heel kleine objecten, kan een elektron zelfs spin-up en spin-down *tegelijkertijd* zijn (een zogenaamde 'superpositie'). Door gebruik te maken van dit principe kan een exponentiële toename in rekenkracht worden gerealiseerd door spins te gebruiken als quantum bits (qubits).

Het eerste experiment in dit proefschrift is gericht op het uitlezen en controleren van de spintoestand van 3 elektronen. Het magnetisch moment van een elektron spin is te klein om op een praktische manier direct gemeten te worden. In 2004 is een technische oplossing bedacht welke de spininformatie omzet in ladingsinformatie (spin-naar-

lading conversie). Een verandering in de lading is in de praktijk eenvoudiger te meten. Als een kwantum dot in de zogenaamde 'uitlees positie' is ingesteld, dan heeft een spin-down elektron wel genoeg energie om de dot te verlaten, terwijl een spin-up elektron in de dot blijft zitten. Een nabijgelegen ladingsdetector kan detecteren of een elektron al dan niet de dot heeft verlaten. Deze techniek vereist dat het uitleesproces plaatsvindt in de buurt van een ladingsdetector en in de nabijheid van een reservoir waar elektronen naar toe kunnen tunnelen. Het is niet praktisch om naast elke quantum dot een ladingssensor en reservoir te plaatsen. Het zou veel beter zijn als de spins zelf naar de ladingssensor verplaatst zouden kunnen worden. Deze benadering is vergelijkbaar met hoe een klassiek ladings-gekoppeld-apparaat (charge-coupled-device, CCD) werkt: een CCD heeft één ladingsdetector om de inhoud van elke afzonderlijke pixel te bepalen (elke pixel bevat een veelvoud aan elektronen als informatiedrager). In analogie met een emmer-brigade ('bucket brigade') verplaatst het de inhoud van elke pixel één voor één naar de ladingsdetector. Deze technologie heeft ervoor gezorgd dat er CCDs zijn gemaakt die eenvoudig miljoenen pixels kunnen uitlezen. In dit eerste experiment hebben we een prototype CCD gemaakt welke op het *enkele* elektron niveau werkt, met behoud van de spintoestand: een Enkele-spin CCD. We laten zien dat het inderdaad mogelijk is om sequentieel drie elektron spins uit te lezen door ze één voor één te verplaatsen naar de dot die het dichtst bij de ladingsdetector in de buurt zit. We behalen een detectie betrouwbaarheid van gemiddeld 97%. Gebruikmakend van elektrische dipool spin resonantie is het ook mogelijk om selectief de spin te draaien in elk van de drie dots. Dit komt overeen met het schrijven van de pixels van de Enkele-spin CCD. Het prototype was redelijk klein waardoor het moeilijk was om te onderscheiden of het verplaatsen van een elektron invloed had op de spintoestand. Om te bepalen wat er zou gebeuren in het geval van grotere rijen van elektronen, hebben we een enkel elektron veelvuldig heen en weer verplaatst in de 3 dots. Tot 500 hops, equivalent aan een afstand van 80 μm, observeren we een verwaarloosbare invloed op de spinprojectie. De grote betrouwbaarheid waarmee de spin projectie kan worden behouden tijdens het shuttlen tussen de dots staat het toe om het Enkele-spin CCD concept op te schalen naar lineaire rijen van honderden dots. Suggesties worden gegeven om de detectie betrouwbaarheid te vergroten voor grotere rijen.

Nu het gelukt was om een 3-dot rij uit te lezen, was de volgende stap om in het tweede experiment te bestuderen hoe twee spins op afstand in een 3-dot aan elkaar gekoppeld kunnen worden. Hiertoe hebben we een enkel elektron in elk van de buitenste dots geplaatst en de middelste dot leeg gelaten. Op het eerste gezicht zou men geen interactie verwachten tussen deze twee afgelegen spins. Echter, door het 'superexchange' mechanisme kunnen elektronen toch interacteren door 'virtueel' van de ene naar de andere dot te hoppen en weer terug. In kwantum dot systemen kunnen we precies instellen hoeveel van de elektron golffunctie in de nabijgelegen dot 'lekt'; dit wordt beschreven door de tunnel koppeling. Als gevolg daarvan kan het linker (rechter) elektron tijdelijk de middelste dot bezetten en geheel naar het rechter (linker) elektron springen en weer terug. De snelheid van dit co-tunneling proces wordt sterk beïnvloed door de naasteburen tunnel koppelingen, en door de hoogte van het energieniveau in de middelste dot. Zulke lange-afstand kwantumcoherentie tussen afgelegen spins zorgt ervoor dat men twee-qubit gates op een afstand kan uitvoeren, en het blijkt dat zulke niet-naaste-

buren interacties ook een belangrijke element zijn om bijvoorbeeld hoge-temperatuur supergeleiding en de reactie van DNA op oxidatieve stress te begrijpen. In dit experiment hebben we een mengsel van de anti-parallelle spin toestand up-down en de parallelle toestand up-up gemaakt. Onder invloed van het superexchange mechanisme zal de anti-parallelle spin toestand veranderen in down-up en continu oscilleren tussen up-down en down-up. De parallelle toestand zal onveranderd blijven. We rapporteren inderdaad zulke oscillaties voor de anti-parallelle toestand en meten de uitwisselingsfrequenties als functie van het energieniveau van de middelste dot. Dit experiment is de eerste experimentele demonstratie van sterke coherente spin-spin koppeling tussen twee afgelegen spins gebruikmakend van een 'quantum mediator' (de lege middelste dot).

Voor de zover beschreven experimenten zijn de benodigde spanningen op de gates om enkele elektronen te vangen met de hand ingesteld. Dit is een tijdrovend proces en zou idealiter geautomatiseerd worden om dit systeem op te kunnen schalen. In het derde experiment hebben we een computer algoritme gemaakt dat twee elektronen naast elkaar kan plaatsen in een dubbele dot met minimale gebruikersinvoer. Het algoritme wordt getest door drie dubbele dots te maken in een 4-dot rij. Aan het eind van het algoritme wordt de data geanalyseerd en bepaalt het systeem of het enkele-elektron gebied is bereikt. In de experimenten beschreven in dit proefschrift was het algoritme succesvol voor alle drie de dubbele dots. Dit is daarmee een belovende eerste stap in het automatisch instellen van grotere rijen elektronen. Toekomstige algoritmes zouden zich kunnen focussen op het correct instellen van dot eigenschappen zoals de tunnel koppeling met de naburige dots.

Het vierde experiment is een voortzetting van het Enkele-spin CCD werk om aan te tonen dat het mogelijk is om elektronen door een rij heen te verplaatsen in een tijdschaal waarbinnen de kwantuminformatie behouden blijft. Het uiteindelijke doel is om een superpositie spintoestand te behouden terwijl deze wordt verplaatst gedurende een kwantumberekening. Het experiment is uitgevoerd in een iets groter systeem, een 4-dot in plaats van een 3-dot, en de tunnel koppelingen tussen de naburige dots zijn op grotere waarden ingesteld. Dit zorgt ervoor dat we een spin shuttle kunnen maken waar een enkel-elektron spin van een kant van de rij naar de andere kant verplaatst kan worden met hoge snelheid. Dit experiment toont aan dat we een elektron binnen hooguit 150 ns door de rij heen konden verplaatsen. Deze bovengrens is gelimiteerd door de relaxatietijd van een zogenaamde 'hot spot'. We hebben geen duidelijke aanwijzingen dat shuttlen op een kortere tijdschaal van 3 ns fouten zou induceren. Dit geeft aan dat een coherente verplaatsing al mogelijk zou moeten zijn in dit systeem waar de levensduur van een superpositie ongeveer 20 ns is. In elk geval is 150 ns snel genoeg in andere materialen zoals Si of Si/SiGe waar deze shuttle-techniek in principe ook gebruikt kan worden.

In het laatste deel van dit proefschrift worden conclusies getrokken en aanbevelingen gedaan voor toekomstige experimenten.

Tim Baart

1

INTRODUCTION

1.1. FROM AMBER & FUR TO MANIPULATING SINGLE ELECTRONS

Creating static charge by rubbing amber with fur is one of humanity's first experiences with electricity. A charged rod of amber could attract light objects such as strands of hair or tiny pieces of paper. During a long period of time many experiments were performed to better understand the concept of electricity. This eventually led to the discovery by J.J. Thomson in 1897 that cathode rays consist of unique particles and these were called 'electrons' after the Greek word for amber [1]. Electrons turn out not only to play a role in electricity, but are also an essential concept to describe and predict a rich variety of other phenomena such as magnetism, chemical bonds, thermal conductivity and superconductivity [2]. Not all details of these phenomena are yet understood, and this makes electrons a very interesting and relevant research topic.

Significant progress in science has led to the capability of manipulating *single* electrons in modern laboratories. It is now for example possible to capture an electron at a well-defined location in a clean piece of semiconductor such as GaAs. By applying suitable electric fields we can push and pull the negative charge of the electron, thereby trapping an electron to the desired location. This man-made 'prison' for an electron is often referred to as a quantum dot. This is not just possible for one electron, but several of them can also be put in a row forming an array of quantum dots. It turns out that such arrays can form a useful asset to study the earlier described phenomena. Let's start with an example of electricity: it is possible to change the strength of the confinement of each dot by varying the applied electric fields. You can thereby influence how easy it is for an electron to jump from one dot the other. The jumping of an electron throughout an array of quantum dots is very similar to the microscopic description of a current-carrying wire (which consists of an array of atoms). By adjusting the confinement, one can *change* the behaviour of the array of quantum dots from an insulator to a conductor. The flexibility with which quantum dots can simulate different systems makes them a very helpful candidate to understand the underlying physics of the before-mentioned phenomena.

1

1.2. QUANTUM MECHANICS

For a complete understanding of the behaviour of electrons the classical picture of charged particles that move around is not enough. We need to take into account that at the length scale of microscopic objects, particles follow the rules of quantum mechanics. An important consequence of this new set of rules is that it is no longer possible to describe an electron just by its location and velocity at a known time t. Instead, an electron is described by its spatial spread using the so-called wavefunction $\Psi(\vec{r}, t)$. In this approach the electron is treated as a *delocalized* particle and the probability density to find the electron at position $\vec{r}$ at time t is given by $|\Psi(\vec{r}, t)|^2$. So it is no longer possible to say with 100% accuracy what the location of the electron is. The wavefunction does still evolve in a deterministic way according to the Schrödinger equation.

This leads to the interesting observation that an electron can effectively be in two places at the same time. So according to quantum mechanics, a single electron can be shared by two (or more) quantum dots instantaneously. The principle that an object can have two conflicting properties at the same time is called 'superposition'. If one measures the location of an electron in a superposition state, the wavefunction is postulated to collapse and you will get one location as answer.

Despite its counter-intuitive concepts, quantum mechanics is a very successful theory that can make accurate predictions that have been verified by experiments. It amongst others led to the development of nuclear energy, the laser, MRI-scanners and transistors: inventions that changed the lives of many people.

1.3. QUANTUM COMPUTATION AND SIMULATION

The quantum mechanical description strongly increased the complexity to simulate the properties of materials. It is no longer possible to assign a well-defined single property to the particles that constitute a material (such as its location), but instead, they can each be delocalized which requires a larger set of variables. However, it is possible to reverse this way of thinking as was done by Richard Feynman, and realize that quantum mechanical systems can be used to solve complex computational problems, or to simulate another quantum mechanical system [3].

To illustrate how computations could be performed, it is convenient to introduce another property of an electron: spin. The electron has an intrinsic angular momentum of spin $\frac{1}{2}$. It can be interpreted as a tiny magnetic moment that can point parallel or anti-parallel to an external magnetic field. In computer language, we could assign these two levels to a bit value of $|0\rangle$ and $|1\rangle$ respectively. In contrast to a classical bit, a so-called quantum bit (qubit) formed by an electron's spin can be both $|0\rangle$ and $|1\rangle$ at the same time due to the superposition principle. In practice an arbitrary superposition $|x\rangle = \alpha|0\rangle + \beta|1\rangle$ can be created with $|\alpha|^2 + |\beta|^2 = 1$. The main advantage of quantum computation is that when performing a computation $f(x)$ on a qubit that is in a superposition, the outcome is a superposition of both $f(|0\rangle)$ and $f(|1\rangle)$. So a single computation outputs the function f evaluated simultaneously for multiple input values. The situation becomes more promising when considering multiple input qubits: every qubit added will double the amount of possible input states. So n qubits allow the evaluation of 2^n input states. To double the computational power of a classical computer of 64 bits,

one needs to add another 64 bits. For a quantum computer adding just one qubit will suffice.

It is important to realize that the output of a quantum computation is a superposition. A measurement of this superposition will however only yield one possible outcome. The challenge is therefore to ask the right question to this superposition. Several algorithms have been devised for this purpose, examples are Shor's algorithm for integer factorization of a number [4] and searching an unstructured database using Grover's algorithm [5].

Besides representing 0's and 1's for the purpose of computation, qubits can also be used to simulate material properties. In the example of electrons captured in quantum dots, the confinement potential dictates the energy levels that the electron(s) inside the dot may occupy. These levels are very similar to the discrete levels an electron can occupy in an atom. For this reason, an array of quantum dots can be interpreted as an array of artificial atoms that could collectively behave as a material. Studying the behaviour of such arrays whilst changing the properties of the artificial atoms could help in the development of new materials.

1.4. QUBIT CANDIDATES

Using the spin state of an electron is certainly not the only qubit that can be made. A good qubit should satisfy the 5 (+2) DiVincenzo criteria [6]. The first 5 are related to computation, and the remaining 2 to communication. Besides electron-spin qubits, other candidates include: nitrogen-vacancy centers [7], superconducting qubits [8], atoms in optical lattices [9], ions in electrostatic traps [10], majorana fermions [11] and charge qubits [12].

At this point in time it is not yet clear which type or combination of qubit(s) is the most suitable to create a viable quantum computer/simulator. Research labs are exploring the pros and cons, and many ideas still need to be tested in practice. Along the way it is important to realize that the exploration of each qubit may have unexpected outcomes and will for sure be a good training for the minds of researchers.

The work in this thesis focuses on using electron spins in quantum dots as qubits in GaAs host material [13]. Due to the small magnetic moment of a spin, it is only weakly influenced by electric fluctuations in the environment. This makes it robust again changes in its qubit state which would lead to computation errors. Also, the design of quantum dots may be compatible with the highly advanced semiconductor industry which could give it a significant scaling advantage.

Although the lifetime of a superposition in GaAs is short compared to other host materials such as Si, GaAs currently still provided the most convenient platform to create arrays of multiple quantum dots due to well-developed fabrication techniques. Spin-qubit-related methods that have been developed in this thesis, can in principle be mapped onto long-lived qubits in Si when its fabrication techniques have become more mature.

1

1.5. THESIS OUTLINE

Finally, we give a brief outline of this thesis:

- **Chapter 2** gives a brief overview of the essential theoretical concepts that aid in the understanding of the experimental results in the later chapters. We describe how single electrons can be captured at well defined locations in space, and how the electron spins interact with the environment and with nearest and even next-nearest neighbour electron spins. It is also explained how the electron spin state can be measured accurately.

- **Chapter 3** discusses the recipe for device fabrication and describes details of the experimental setups that were used to obtain the experimental results.

- **Chapter 4** describes the first experimental realization of a so-called Single-spin CCD. It is a platform in which individual electrons spins are moved around in a controlled manner by analogy to a classical CCD. Using a triple-quantum-dot array, we read out three spins sequentially with read-out fidelities of 97% on average. We perform site-selective control of the three spins that enable writing of the CCD register. Finally, we show that shuttling an electron back and forth in the array hundreds of times, has negligible influence on its spin projection. This work forms the first demonstration of controlled single-electron transport with preservation of spin.

- **Chapter 5** presents measurements where two spins are coupled to each other that are separated by an empty quantum dot in between. The empty quantum dot acts as a mediator that induces a long-range interaction between the two distant spins. This works forms a first example of coherent coupling between two distant spins through a quantum mediator in the solid-state.

- **Chapter 6** reports on the computer-automated 'capturing' of single electrons inside quantum dots. The capturing of electron spins in previous chapters was done by tuning the correct gate voltages by hand and is a time-consuming process. In this chapter we describe a computer algorithm that can automatically create double quantum dots using minimal user input.

- **Chapter 7** presents a follow-up experiment of the Single-spin CCD where the aim is to shuttle an electron spin faster than the decoherence time. This experiment is performed inside a quadruple-dot device and shows that by increasing the tunnel couplings between dots we can shuttle an electron spin across four dots within less than 150 ns, and possibly even faster.

- **Chapter 8** concludes the thesis by discussing outstanding challenges in the field and possible directions for future research.

2

THEORY OF SPINS IN FEW-ELECTRON GaAs QUANTUM DOTS

This chapter describes the essential theoretical concepts that aid in the understanding of the experimental results described in the later chapters. First our system of choice for studying electrons in the solid state is introduced: laterally defined quantum dots in semiconductor heterostructures. We describe how single electrons can be confined in nanoscale space with great precision. Next, we explain how the spin state of the electron interacts with the environment. This includes interaction with the host material GaAs and with the nearest and even next-nearest neighbour electron spins. We end by describing how the spin state of an electron can be measured accurately.

2.1. LATERALLY DEFINED QUANTUM DOTS

Quantum dots are tiny islands in which charge is confined in all three directions. The number of charges confined on such an island can be controlled up to the single-electron number. Although quantum dots are larger than atoms, the dimensions of quantum dots (~1-100 nm) are still small enough to discern discrete energy levels at low temperatures. Quantum dots are often referred to as artificial atoms because their properties are quite similar to atoms. One advantage of quantum dots is that many of their properties, such as shape, charge number, coupling to neighbouring dots etc., can be changed by design or even tuned *in situ* at low temperature depending on the system used. This makes quantum dots a very interesting platform to study the behaviour of confined electrons. This is not only an interesting topic in itself, but may also provide to be a useful asset for the application of quantum simulation or computation.

Various approaches exist to create quantum dots, e.g.: self-assembled dots [14], quantum dots defined in nanowires [15, 16] or nanotubes [17, 18]. In this thesis we focus on quantum dots defined electrostatically by metallic gate electrodes inside a two-dimensional electron gas (2DEG) of a doped GaAs/AlGaAs heterostructure.

2.1.1. CREATION OF LATERAL QUANTUM DOTS

A schematic view of GaAs/AlGaAs heterostructure with Au-Ti gates patterned on the surface to define quantum dots is shown in Fig. 2.1. The 2DEG, confining the electrons in z-direction, is formed by growing two slightly different alloys onto each other: first a thick layer of GaAs (100's of μm), and next a thin (~100 nm) layer of $Al_xGa_{1-x}As$ where x is typically 0.3 for our experiments. GaAs and AlGaAs have the same crystal structure (Zinc-blende) and a very similar lattice constant which allows these alloys to be grown on top of each other almost perfectly using for example molecular beam epitaxy (MBE). They do have a different bandgap however, which together with some Si delta-doping of a thin slice of the AlGaAs is used to create the 2DEG. The electrons donated by the Si will diffuse to the GaAs side and will not be able to diffuse back because of the difference in bandgap of the two alloys: the conduction band in GaAs is lower in energy. As a consequence, these electrons stay in the GaAs side and leave positively charged Si-donors in the AlGaAs layer. These donors will create an attractive electric field confining the electrons to the interface of the GaAs/AlGaAs layer. The resulting confinement potential is modeled as a triangular potential well. At low temperatures only the lowest mode of the well is populated and the electrons can be treated as being fully confined in the z-direction. The confinement is so strong that ~90% of the 2DEG is confined in the first 20 nm of the well. Although restricted to move in the z-direction, the electrons can still move freely in the other two directions.

The state of the art in growth of GaAs/AlGaAs heterostructures is so good that they can be grown with very little defects which would induce electron scattering. It was typical to use wafers with mobilities above a few million cm^2/Vs for the work described in this thesis[1].

The 2DEG provides the starting point for creating lateral quantum dots and in Delft we fabricate metallic gates on top of the wafer to 'push' away all the electrons that we

[1] These wafers were supplied by Christian Reichl and prof. dr. Werner Wegscheider from ETH Zürich.

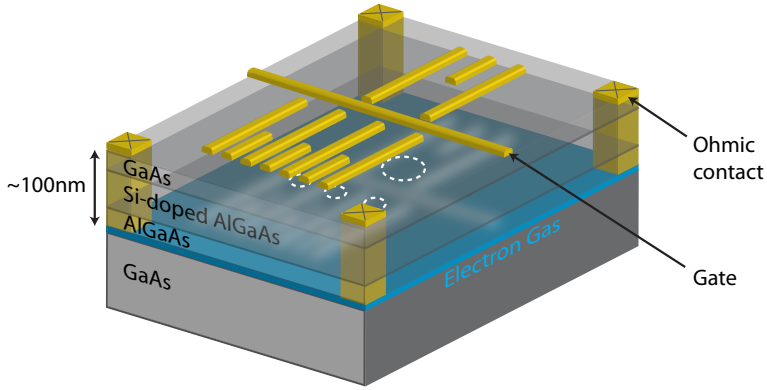

Figure 2.1: A schematic view of a GaAs/AlGaAs heterostructure with Au-Ti gates patterned on the surface to define a triple quantum dot with one charge sensor. Ohmic contacts to the 2DEG are depicted as vertical pillars that contact the 2DEG. White dashed circles indicate the positions of the formed quantum dots. Figure adopted from Ref. [19].

do not want such that we end up with a single electron at a well-defined location in space. Details of the device fabrication can be found in section 3.1. Due to the relatively low electron densities ($\sim 2 \cdot 10^{11}$ cm^{-2}), up to typically -1 V is required to deplete the 2DEG underneath a gate. Changing the voltages on the gates allows precise control of the number of electrons on each dot. A gate shared by two neighbouring quantum dots is typically used to set the overlap of the wavefunction of the two neighbouring electron spins: the tunnel coupling t. To probe the quantum dots, ohmic contacts are formed that create an electrical connection between the 2DEG and the outside world.

Tuning of quantum dots is now a routine process in labs around the world. Most quantum dots have still been tuned by hand though; a computer-automated version is described in Chapter 6.

2.1.2. CHARGE STABILITY DIAGRAMS OF MULTIPLE COUPLED QUANTUM DOTS

From the previous section it is clear that quantum dots can be created by setting the right gate voltages. The voltages should be tweaked such that the barriers surrounding the dot are sufficiently closed. In that regime the number of electrons on the dot can be treated as a well-defined classical integer number. This requires that the resistance of each barrier connecting the dot to the environment should be larger than the resistance quantum $\frac{h}{e^2}$ [20]. The resistance should also not be too high. To perform read-out of the spin state for example, there should still be sufficient coupling with the external reservoirs to be able to determine the spin state well within the T_1-time (see Section 4.6.1 for details).

A very useful tool to visualize the response of the quantum dots to changes in the gate voltages are so-called charge stability diagrams. These plot the response of a nearby charge sensor as a function of the voltages applied to the gates defining the quantum dots. If a single electron goes into or out of a dot, the charge sensor will already sense this. This subsection describes how to model and understand these diagrams for multiple

coupled quantum dots.

In a first approximation the behaviour of quantum dots can be modeled by assigning a voltage, capacitance and/or charge to each of the individual elements: dots, gates and source and drain reservoirs. Such a simplified electrical scheme is shown in Fig. 2.2 for a triple dot with one charge sensor. These quantities are then used to calculate the energy spectrum of the quantum using the constant interaction model [21, 22]. This model is based on two assumptions: (1) the Coulomb interaction felt by an electron in the dot with all other charges around is parametrized by a single, constant capacitance C. The capacitance is the sum of all the capacitances that connect to the dot, such as from the source, drain and gates, and the self-capacitance of the dot. Assumption (2) is that the single-particle energy-level spectrum is independent of the number of electrons. In this model each element can be assigned a voltage V_i, capacitance C_i and a charge Q_i. The total ground-state energy $U(N)$ of a dot with N electrons in the dot and voltages V_i applied is then given by:

$$U(N) = \frac{\left(-|e|(N-N_0)+\sum_i C_i V_i\right)^2}{2C} + \sum_{n=1}^{N} E_n(B), \tag{2.1}$$

where $-|e|$ is the electron charge, N_0 is the number of electrons in the dot attracted by the positive background charge originating from the donors for $V_i = 0$ and B the magnetic field. The first term describes how each of the gate voltages can each induce a continuous amount of charge on the dot and thereby fine tune the number of electrons on each dot (to be precise, the electrochemical potential of each dot). The second term is the sum of all the occupied single-particle energy levels $E_n(B)$ such as the different orbital and spin states (see section 2.2.1) an electron can occupy inside the dot. The shape of these orbitals, and therefore their energy, is influenced by confinement potential and the magnetic field. The spin states directly couple to the magnetic field. Only the second term of Eq. 2.1 makes the model non-classical.

We can now introduce a very useful quantity called the electrochemical potential of the dot $\mu(N)$. This is defined as:

$$\begin{aligned}\mu(N) &\equiv U(N) - U(N-1) \\ &= \left(N - N_0 - \frac{1}{2}\right)E_C - \frac{E_C}{|e|}\left(\sum_i C_i V_i\right) + E_N,\end{aligned} \tag{2.2}$$

where $E_C = \frac{e^2}{C}$ is the charging energy. The electrochemical potential tells how much energy is required to add an extra electron to the system. It depends linearly on the applied gate voltages which makes it a convenient quantity to describe electron tunneling. Figs. 2.3ab illustrate the electrochemical potential levels of a dot in the low-bias regime. This 'ladder' of levels can now be changed linearly by adjusting the gate voltages. Whenever a level in the dot lies within the bias window, current through the dots is possible. This gives rise to so-called Coulomb peaks in the measured current, see Fig. 2.3c.

In the case of multiple quantum dots in series, it is not always possible to measure the current through the array. The current will then only be high when the electrochemical potentials of all dots are aligned and lie within the bias window. This results in limited

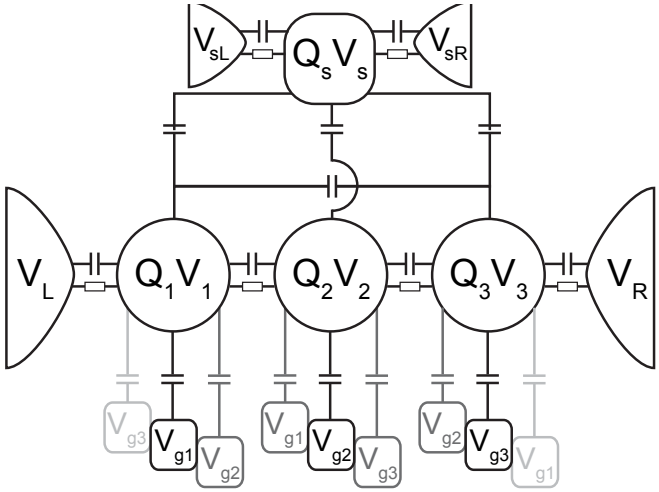

Figure 2.2: Simplified electrical scheme of a triple-dot quantum dot with one charge sensor. Lines connecting elements with a rectangular box indicate tunnel barriers. Figure adopted from Ref. [19].

information on the system. Instead, it can be more convenient to measure the response using an adjacent charge sensor. This could for example be a sensing dot (SD). The conductance of the SD can be tuned on the steep flank of a Coulomb peak. Small changes in the electrostatic environment will then result in a significant change in the conductance of the SD. More information on the precise tuning can be found in Chapter 6. Charge sensors are sensitive to all changes in the charge configuration and therefore provide more information than a transport measurement.

An example of a triple-dot charge stability diagram measured through charge sensing is shown in Fig. 2.4. The horizontal and vertical lines correspond to the charging of the left and right dot respectively. The charging lines of the middle dot are mostly faded. This can be understood from the fact that the middle dot is not directly coupled to a reservoir,

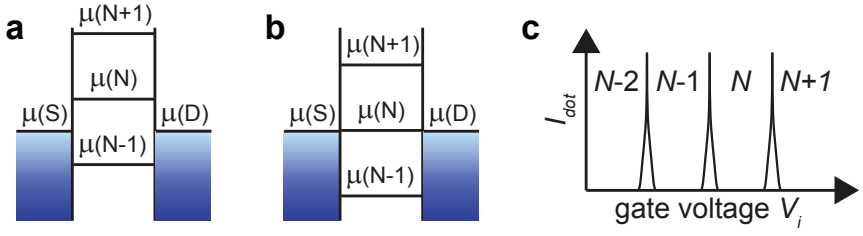

Figure 2.3: Quantum dot in the regime of low bias. (a,b) Electrochemical potential levels inside the dot. By changing the gate voltages this so-called 'ladder' can be moved up and down. (a) There is no available level within the bias window: transport through the dot is blocked and the dot is in the so-called Coulomb-blockade regime. (b) There is one level available within the bias window and resonant tunneling can occur. (c) Whilst changing a gate voltage, the ladder in (a) and (b) will move giving rise to alternating patterns of current and no current through the dot. The peaks in current are also referred to as Coulomb peaks.

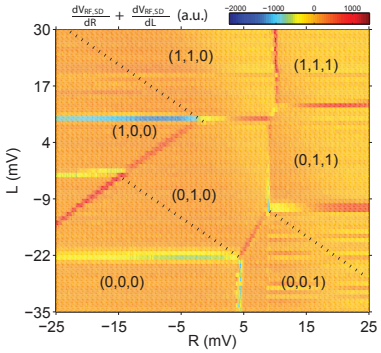

Figure 2.4: Triple-dot charge stability diagram measured by charge sensing. Displayed is the differentiated charge sensor response as a function of the two 'virtual gates' L and R (see Section 4.6.5). R is swept from positive to negative. The labels (n,m,p) denote the number of electrons in the left, middle and right dot respectively. The (0,0,0)-regime is identified by the lack of additional charging lines for more negative gates voltages. The fading of the middle dot charging lines, e.g. the blue horizontal line at $L \approx 8$ mV, can be explained by the fact that the middle dot is not coupled directly to a reservoir [23] (black dashed lines indicate their positions).

so that it can only load and unload through the left and or right dot [23]. In Fig. 2.4, gate R is swept from right to left. Starting in (0,1,0) for example, the middle dot can then only empty itself by first aligning with the left dot. This gives rise to the extended red line inside the (0,0,0)-regime. The charge stability diagram forms the basis for a spin qubit experiment in quantum dots by telling us which voltages need to be applied to achieve a specific charge operation.

2.2. SPINS IN QUANTUM DOTS

The previous section described how the number of electrons in each dot can be controlled up to the single-electron level. We will now describe the relevant theory for the spin states of these electrons. The spin state can be used as a quantum bit and much effort in the field of quantum dots is aimed at the purpose of quantum information processing. We start by describing the spin states in a single quantum dot, restricting ourselves to at most 2 electrons per dot. We next explain how the spin state is influenced by its environment in the heterostructure: the spin-orbit interaction and the hyperfine interaction. We end with a description of the two-electron spin states in tunnel-coupled quantum dots which form the basis for driving a two-qubit exchange gate.

2.2.1. SPIN STATES IN A SINGLE QUANTUM DOT

A single electron inside a quantum dot can be described by a two-level system consisting of the states $|\uparrow\rangle$ and $|\downarrow\rangle$. Under the influence of a magnetic field B, the $|\uparrow\rangle$ -state, which is parallel with the external field, will be the ground state. The energy difference between the two states is given by the Zeeman energy: $\Delta E_z = g\mu_B B$, where g is the electron g-factor (~ -0.4) and μ_B the Bohr magneton.

With two electrons inside a single quantum dot, there are four possible spin states. As electrons are fermions, their wavefunction should be asymmetric under influence of

the exchange operator which interchanges two particles. The wavefunction consists of both the spin and the orbital part. If two electrons occupy the same orbital, then the spin part should be asymmetric which is the spin singlet $|S\rangle = \frac{|\uparrow\downarrow\rangle - |\downarrow\uparrow\rangle}{\sqrt{2}}$. This state has total spin zero. If the electrons occupy a different orbital, there are three options for the spin state: the three triplets $|T_0\rangle = \frac{|\uparrow\downarrow\rangle + |\downarrow\uparrow\rangle}{\sqrt{2}}$, $|T_-\rangle = |\downarrow\downarrow\rangle$and $|T_+\rangle = |\uparrow\uparrow\rangle$. These states have spin 1 with $m_s = 0, -1, +1$ respectively.

Defining the energy of the singlet state to be $E(S)$, the energy of the triplet states can be written down as follows:

$$\begin{aligned} E(T_-) &= E(S) + E_{ST} - \Delta E_z \\ E(T_0) &= E(S) + E_{ST} \\ E(T_+) &= E(S) + E_{ST} + \Delta E_z, \end{aligned} \tag{2.3}$$

where E_{ST} is the so-called singlet-triplet splitting. E_{ST} consists of two terms: $E_{ST} = E_{\text{orb}} - E_K$. E_{orb} is the orbital level spacing. E_K consists of the reduction in Coulomb repulsion between the two electrons as they occupy different orbitals for the triplet states (on average the two electrons can then be further apart), and the asymmetry of the orbital part of the wavefunction also leads to a reduction in energy (the exchange energy) [24]. For in-plane magnetic fields E_{ST} is in general positive making the singlet the ground state of the system [25, 26]. This energy separation between the singlet and the triplet states is used to entangle two distant spins in Chapter 5.

2.2.2. SPIN INTERACTION WITH THE ENVIRONMENT

The magnetic moment of an electron spin is very small. As a consequence, the spin states are only weakly perturbed by the magnetic environment. Electric field fluctuations can only affect spins indirectly, so the spin state is typically only weakly influenced. For electron spins in quantum dots there are three main sources of interaction with the environment: (1) spin-orbit coupling, (2) hyperfine coupling with the nuclear spins of the host material and (3) exchange processes with electrons in the reservoirs. In the following discussion we assume that the tunnel coupling with the reservoirs is sufficiently closed such that mechanism (3) can be neglected (see section 4.6.3 for a detailed example where we do take mechanism (3) into account).

SPIN-ORBIT INTERACTION

The spin-orbit interaction (SOI) is an interaction of a particle's spin with its motion. An electron spin moving in a spatially-varying electric field $\vec{E}$ will experience an electric field that changes in time which generates a magnetic field that couples to the spin state of the electron. This effective magnetic field, $\vec{B}_{\text{SO}}$, is proportional to $\vec{E} \times \vec{p}$, where $\vec{p}$ is the momentum of the electron. This gives rise to an effective SOI Hamiltonian of the form $H_{\text{SOI}} \propto \vec{\sigma} \cdot \vec{B}_{\text{SO}}$, with $\vec{\sigma}$ the Pauli matrices. In the solid state, the spatially-varying electric field originates from the charged atoms in the lattice.

In AlGaAs/GaAs heterostructures there are two origins for the local electric fields originating from the crystal. (1) GaAs lacks bulk inversion symmetry leading to the Dresselhaus contribution [27]. (2) At the heterointerface of AlGaAs/GaAs there is a strong asymmetric confining potential (structural inversion asymmetry). This is the Rashba

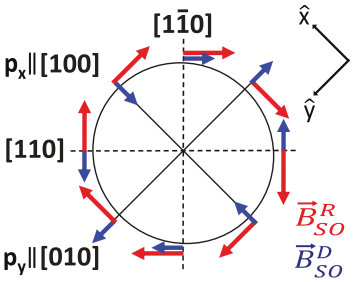

Figure 2.5: The spin-orbit field $\vec{B}_{\mathrm{SO}}$ acting on an electron spin moving in a 2DEG with momentum $\vec{p}$ is shown by red (Rashba) and blue (Dresselhaus) arrows. The Rashba and Dresselhaus term are chosen to be different in modulus and $\alpha < 0$ and $\beta > 0$. Figure adopted from Ref. [30].

term [28]. For growth in the z-direction, (001), the linear terms of the SOI in two dimensions are given by:

$$H^{\mathrm{2D}}_{\mathrm{SOI}} = \beta\left(-p_x\sigma_x + p_y\sigma_y\right) + \alpha\left(-p_y\sigma_x + p_x\sigma_y\right), \tag{2.4}$$

where x and y point along the crystallographic directions (100) and (010) respectively, β describes the strength of the Dresselhaus term which depends on material properties and on $\langle p_z^2 \rangle$, and α describes the strength of the Rasbha term that is material specific and depends on the confining potential. α and β do not necessarily have the same sign [29], and in our experience their signs are actually different for the heterostructures that we used. The effect of Eq. 2.4 is depicted schematically in Fig. 2.5. From this figure it becomes clear that B_{SO} strongly depends on the direction of motion. This is used to choose the right orientation of the quantum dot gate pattern with respect to the crystal axis. An example is shown in Chapter 4 where the [1$\bar{1}$0] axis is used for electric-dipole spin resonance (EDSR) (requiring strong SOI), whilst the [110] axis is used to shuttle spin states with minimal influence of SOI.

SOI couples states that contain both different orbital and different spin parts [31]. As a result, the eigenstates of the system become admixtures of spin and orbital states [32]. Although pure spin states do not couple to electric fields, the orbital part will couple to electric fields. Through SOI, electric field fluctuations can now lead to spin relaxation which is characterized by a T_1-time. In experimental setups that have sufficient filtering on the measurement electronics (see section 3.2.2), the dominant source of electric field fluctuations is from phonons in the GaAs substrate. Phonons can induce electric fields in two ways: (1) they either inhomogeneously deform the lattice leading to spatial variations in the band gap which gives rise to changes in the electric field, or (2) homogeneous strain leads to electric fields in piezoelectric material such as GaAs. The expected T_1-time can be derived based on the phonon density of states at the energy splitting of the spin states ΔE_z ($\propto \Delta E_z^2$), and how strong the phonons couple to the spin-orbit perturbed eigenstates which is determined by the electric-field amplitude of the phonons. T_1 is predicted to vary with ΔE_z^{-7} for coupling to deformation potential phonons (1), and ΔE_z^{-5} for coupling with piezoelectric phonons (2) [32]. At low energy (below ~ 0.6 meV in GaAs) piezoelectric phonons are dominant leading to the experimentally observed

$T_1 \propto \Delta E_z^{-5}$ [26]. This relation describes the trade-off between on the one hand wanting to work at high magnetic fields where it is easier to distinguish spin-up and spin-down (see section 2.3), and on the other hand wanting a large spin lifetime.

Besides the relaxation time T_1, qubits can also be characterized by the timescale during which the phase of a superposition is preserved. This time scale is called the dephasing time denoted by T_2^*. This timescale is in first order not limited by SOI [33]. T_2^* is however strongly influenced by the hyperfine interaction which we will describe next.

HYPERFINE INTERACTION

An electron spin in GaAs is surrounded by atoms whose nuclei have non-zero spin. Through the hyperfine coupling, the electron spin and the nuclear spins will interact. The Hamiltonian for the Fermi contact hyperfine interaction for an electron in contact with N nuclear spins is given by

$$H_{\mathrm{HF}} = \sum_k^N A_k \vec{I}_k \cdot \vec{S}, \tag{2.5}$$

where $\vec{I}_k$ and $\vec{S}$ are the spin operator for nuclues k and the electron spin respectively [34]. The coupling strength, A_k, depends on the overlap of the electron wavefunction with the k^{th} nuclear spin. For our dots N is typically $\sim 10^6$.

It can be convenient to model the effect of all nuclear spins combined as one effective magnetic field B_N. This field is typically called the Overhauser field. The Hamiltonian can then be rewritten as:

$$H_{\mathrm{HF}} = g\mu_B \vec{B}_N \cdot \vec{S} \tag{2.6}$$

The magnitude of the nuclear field $B_N = \frac{\sum_k^N A_k \vec{I}_k}{g\mu_B}$ is maximum when all spins are fully polarized. This would correspond to ~5 T in GaAs [35]. In typical experimental conditions the nuclear spins are however almost fully unpolarized. There will be a small polarization along the external field with a magnitude that can be derived from the Boltzmann distribution. Around this small polarization, there will be Gaussian distribution with width $\sigma_N = \frac{B_{N,max}}{\sqrt{N}} \approx 5$ mT in all three directions [36].

In typical experiments we apply an external magnetic field of several Tesla setting the quantization axis and the precession rate for the electron spin. The transverse components of the hyperfine field, $B_N^{x,y}$, influence the precession rate only to second order and can be neglected for practical purposes. The longitudinal component, B_N^z, has a significant influence on the precession rate however. If $B_N^z = 5$ mT, the precession rate is increased by 28 MHz ($g = -0.4$), causing the spin to pick up an extra π-rotation in just 18 ns.

At large magnetic fields B_N^z fluctuates on a timescale much slower than the electron spin dynamics: ~seconds versus nano- to milliseconds [26]. At any given time, the nuclear field thus assumes a random quasi-static value drawn from a Gaussian distribution. The lack of knowledge of the effective instantaneous field results in a measured dephasing time $T_2^* \approx 40$ ns [37].

When moving to more than one dot, the difference in Overhauser field between the dots can be used to drive transitions between different spin states [38]. The spins acquire

a different phase depending on which dot they occupy which leads to coherent transitions between the T_0 and S state. The same is true if the Zeeman energy in the dots is different due to spatially varying g-factors; this is used in Chapter 5.

The interplay between the electron spin and the nuclear spins is an interesting field on its own [39–41]. In the work described in this thesis the hyperfine interaction is mostly seen as a source of uncertainty in the qubit frequency, which makes it hard to drive a single-electron spin coherently. Solutions to that problem include moving to a different host material with less to no nuclear spins, such as Si [42], or Si/SiGe [43]; or applying dynamical decoupling schemes to compensate for the slowly fluctuating nuclear spin bath [40].

2.2.3. TWO-ELECTRON SPIN STATES IN TUNNEL-COUPLED QUANTUM DOTS

So far we have only discussed spin states of uncoupled quantum dots. The situation becomes more interesting when dots also become coupled to one another which can give rise to entanglement between spins of distinct quantum dots. One way to couple dots is by allowing the electron spin to delocalize over more than one dot. In this way the wavefunction of two electrons can start overlapping. This form of coupling is called tunnel coupling. In this section we will start by describing the effect of tunnel coupling on the spin states for nearest-neighbour dots, and explain how it can be used to drive a two-qubit gate called the exchange gate. In Chapter 5 we demonstrate that it is also possible to effectively tunnel couple next-nearest-neighbour quantum dots. We will end the discussion by deriving an approximate expression for this 'long-range' tunnel coupling.

NEAREST-NEIGHBOUR COUPLED QUANTUM DOTS

We will focus on the situation of two electrons inside a double quantum dot. This is a typical regime for many double dot experiments. Electrons can be moved between the dots by changing the detuning ϵ of the electrochemical potentials in the dots by using gate voltages. For two electrons in a double dot, the detuning is given by $\epsilon = \mu_l(1,1) - \mu_r(0,2)$, where μ refers to the electrochemical potential of the ground state for that charge state.

The spin states for a double dot in the (0,2) (or (2,0)) configuration have already been described in section 2.2.1 and can be written as:

$$\begin{aligned} S(0,2) &= \frac{|\uparrow_2\downarrow_2\rangle - |\downarrow_2\uparrow_2\rangle}{\sqrt{2}} \\ T_-(0,2) &= |\downarrow_2\downarrow_2\rangle \\ T_0(0,2) &= \frac{|\uparrow_2\downarrow_2\rangle + |\downarrow_2\uparrow_2\rangle}{\sqrt{2}} \\ T_+(0,2) &= |\uparrow_2\uparrow_2\rangle\,, \end{aligned} \tag{2.7}$$

where the subscripts denotes in which dot the electron resides. As in the single dot case, the triplet states are detuned from the singlet state by E_{ST}. At finite magnetic field the $T_-(0,2)$ and $T_+(0,2)$ are further detuned by $\pm\Delta E_z$.

The spin states for the (1,1) configuration are very similar, only now the two electrons

each occupy their own dot. The states are then described by:

$$\begin{aligned} S(1,1) &= \frac{|\uparrow_1\downarrow_2\rangle - |\downarrow_1\uparrow_2\rangle}{\sqrt{2}} \\ T_-(1,1) &= |\downarrow_1\downarrow_2\rangle \\ T_0(1,1) &= \frac{|\uparrow_1\downarrow_2\rangle + |\downarrow_1\uparrow_2\rangle}{\sqrt{2}} \\ T_+(1,1) &= |\uparrow_1\uparrow_2\rangle \end{aligned} \tag{2.8}$$

In this case, the singlet-triplet splitting is not determined anymore by the orbital level splitting as each electron resides in its own dot where they can both occupy the lowest orbital. The energy spectrum is now strongly influenced by the strength of the coupling between charge states (1,1) and (0,2) which is given by the matrix element $\sqrt{2}t_c$. In the absence of the hyperfine interaction and/or spin-orbit coupling, the tunnel coupling is spin-conserving. Therefore, only the singlet (triplet) (1,1)-state will hybridize with the singlet (triplet) (0,2)-state. This gives rise to an avoided crossing that is characterized by a tunnel splitting $2\sqrt{2}t_c$. At $\epsilon = 0$, the eigenstates are no longer given by S(1,1) or S(0,2), but instead by hybridized bonding and anti-bonding states [22]:

$$\begin{aligned} |\psi_B\rangle &= -\sin\frac{\theta}{2}e^{-i\phi/2}S(1,1) + \cos\frac{\theta}{2}e^{i\phi/2}S(0,2) \\ |\psi_A\rangle &= \cos\frac{\theta}{2}e^{-i\phi/2}S(1,1) + \sin\frac{\theta}{2}e^{i\phi/2}S(0,2) \end{aligned} \tag{2.9}$$

with $\tan\theta = 2\sqrt{2}t_c/\epsilon$. The energy difference between $|\psi_B\rangle$ and $|\psi_A\rangle$ is given by $\sqrt{\epsilon^2 + (2\sqrt{2}t_c)^2}$. The orbital level splitting in GaAs is typically much larger than t_c, which shifts the anticrossing of the triplet states to a higher detuning than the singlet states. The energy diagram at finite magnetic field is shown in Fig. 2.6. A very interesting consequence of this diagram is the ability to tune the singlet-triplet splitting by changing the detuning. This splitting can be expressed as the difference in energy between the $T_0(1,1)$ and the hybridized $S(1,1)/S(0,2)$ state which yields an effective exchange interaction J. Around $\epsilon \approx 0$ this splitting is given by:

$$J = \frac{\sqrt{\epsilon^2 + (2\sqrt{2}t_c)^2}}{2} + \frac{\epsilon}{2} \tag{2.10}$$

Strictly speaking the term exchange only refers to the difference in Coulomb energy between states whose orbital wave function differ in their symmetry. So symmetric for a spin singlet and asymmetric for a spin triplet. In the double dot case, this splitting can also be significantly influenced by the hybridization with the (0,2)-state. The resulting energy difference enters the Hamiltonian in the same way as the 'standard' exchange energy: $H_J = J\vec{S}_1 \cdot \vec{S}_2$ [13].

To understand why this tunable exchange energy can be so convenient, it is helpful to define a Bloch sphere as depicted in Fig. 2.6. The eigenstates of the exchange energy S and T_0 are at the North and South pole, split by J. The eigenstates of the gradient in Zeeman energy between the dots, $\Delta E_{z,dots}$, are the poles along the x-axis. This gradient

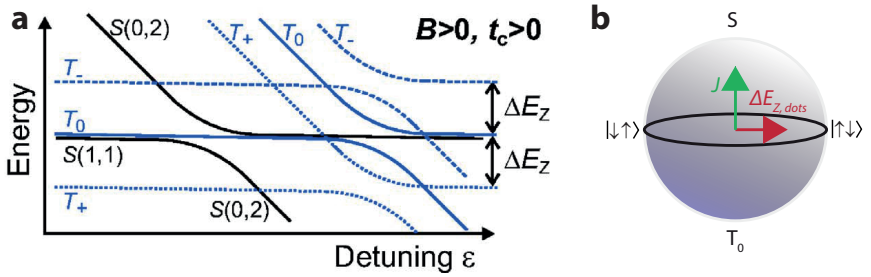

Figure 2.6: (a) Energies of the two-spin states in a double quantum dot as a function of detuning ϵ between the outer dots at finite magnetic field. Figure adopted from Ref. [26]. (b) Bloch sphere representation of a double dot qubit with control axes J and ΔE_z.

can arise from different g-factors in each dot (see for example Chapters 4 and 5), or from a gradient in the hyperfine field [44]. The precession of the spin state is described by a rotation along the vector sum of the two axes J and $\Delta E_{z,dots}$.

One could now for example initialize the spin state to $|\uparrow\downarrow\rangle$ by turning off J by going to negative detuning. To approximately swap the spin state to $|\downarrow\uparrow\rangle$, you should turn on J to a value much larger than $\Delta E_{z,dots}$ for a time $\approx \hbar\pi/J$. If it is not possible to make J very large, you can still reach each point of the Bloch sphere by concatenating several pulses [45]. In practice the turn-on time of J is also not infinitely fast due to hardware restrictions: it is not possible to change gate voltages instantaneously. The finite risetime can also be taken into account as shown in Chapter 5.

All in all, single qubit rotations combined with the two-qubit exchange gate, are sufficient to create a universal set of gates for quantum computation [46].

NEXT-NEAREST-NEIGHBOUR COUPLED QUANTUM DOTS

In the previous section we derived that tunnel coupling two neighbouring dots has a significant influence on the spin states and gives the experimentalist a 'knob' to turn on/off interactions between qubits. The intuitive picture behind this scheme is that we can *in situ* change the overlap of the wavefunction of two electrons and thereby the effective exchange energy. The 'portion' of wavefunction outside a quantum dot leaking into the next neighbour decays exponentially with the distance. This severely restricts the strength of coupling between more distant qubits. Instead of having to repeatedly swap neighbouring qubits, it would be very beneficial if one could use a more 'long range' approach to couple qubits. A common approach to achieve long-distance coupling is achieved by using a quantum bus. There are many ways proposals for creating such a quantum bus (see Chapter 5). One of the options is by using an empty quantum dot and this has experimentally been achieved in Chapter 5. The underlying mechanism is called superexchange (SE). In this section we will derive an approximation for the resulting effective tunnel coupling t_{SE} between two distant quantum dots mediated by such an empty dot. The resulting t_{SE} can then be utilized in a similar way as described for nearest-neighbour qubits to drive a two-qubit gate.

The Hamiltonian describing the experiment with just the outer dots of a triple dot array occupied, can be described in the basis $|\psi_1^0\rangle = |200\rangle$, $|\psi_2^0\rangle = |101\rangle$ and $|\psi_3^0\rangle = |110\rangle$

as:

$$H = \begin{pmatrix} -\epsilon/2 & 0 & t_l \\ 0 & \epsilon/2 & t_r \\ t_l & t_r & -\delta \end{pmatrix}$$

The matrix elements are defined as follows:

- ϵ is the detuning between the outer dots
- δ is the detuning of the middle dot with respect to the average of the outer dots
- t_l is the tunnel coupling between the (200) and (110) state
- t_r is the tunnel coupling between the (110) and (101) state

For simplicity we will assume in the following that $t_l = t_r = t$. Using first-order perturbation theory the new eigenstates can be expressed as:

$$\begin{aligned} |\psi_1^1\rangle &= |200\rangle + \frac{t}{\delta - \frac{\epsilon}{2}} |110\rangle \\ |\psi_2^1\rangle &= |101\rangle + \frac{t}{\delta + \frac{\epsilon}{2}} |110\rangle \\ |\psi_3^1\rangle &= |110\rangle - \frac{t}{\delta - \frac{\epsilon}{2}} |200\rangle - \frac{t}{\delta + \frac{\epsilon}{2}} |101\rangle \end{aligned} \tag{2.11}$$

Using this step we assume[2] that $\delta - \frac{\epsilon}{2} \gg t$ and $\delta + \frac{\epsilon}{2} \gg t$. The perturbed Hamiltonian, H', can then be expressed as $H' = U^\dagger H U$, where the unitary matrix is given by:

$$U = \begin{pmatrix} 1 & 0 & -\frac{t}{\delta - \frac{\epsilon}{2}} \\ 0 & 1 & -\frac{t}{\delta + \frac{\epsilon}{2}} \\ \frac{t}{\delta - \frac{\epsilon}{2}} & \frac{t}{\delta + \frac{\epsilon}{2}} & 1 \end{pmatrix}$$

Applying this unitary transformation results in:

$$H' = \begin{pmatrix} -\epsilon'/2 & t_{SE} & t_l' \\ t_{SE} & \epsilon'/2 & t_r' \\ t_l' & t_r' & -\delta' \end{pmatrix},$$

where ϵ', δ' denote renormalized detunings; t_l', t_r' are proportional to $\frac{t^3}{\delta^2}$ and can be neglected; and the effective tunnel coupling between the outer dots is given by:

$$t_{SE} = \frac{t^2}{\delta - \frac{\epsilon^2}{4\delta}} \tag{2.12}$$

The result of Eq. 2.12 can now be utilized in a similar way as was done for describing the exchange gate for nearest-neighbours. In this case, J_{SE} can be turned on (off) by for example bringing the empty level of the middle dot closer to (further away from) the energy levels of the outer dots.

[2] The experiment in Chapter 5 was partially performed outside the range of validity of the above approximation. Simulations shown in that Chapter were therefore performed by numerically solving the Schrödinger equation.

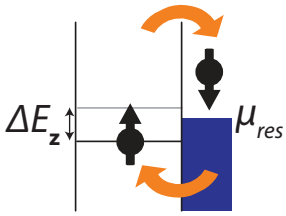

Figure 2.7: Energy diagram depicting spin-to-charge conversion for the so-called 'Elzerman' method. By aligning the spin levels around μ_{res}, a $|\downarrow\rangle$ has enough energy to tunnel out of the dot into the reservoir, whilst a $|\uparrow\rangle$ does not. Whether an electron tunneled out of the dot can be registered using a nearby charge sensor. Note that both spin species have the same Fermi energy.

2.3. SINGLE-SHOT SPIN DETECTION

So far the discussion has been about how electron spins can be captured, how they interact with the environment, and how the spin can be changed. We will end by describing how the spin state itself can be measured in a single-shot manner (only one copy of the electron is available, so no averaging). The magnetic moment of an electron is very small (μ_B) which makes it hard to measure directly using a magnetometer. However, it is possible to correlate the spin state of an electron with different charge states of the quantum dot through a technique called spin-to-charge conversion. It is more straightforward to measure the charge present on a quantum dot as was seen in section 2.1.2. There exist several ways to perform spin-to-charge-conversion, and here we will highlight two of them: (1) energy-selective readout in the so-called 'Elzerman way' [47], and (2) in a manner based on the principle of Pauli Spin Blockade (PSB) [48]. Option (1) is used throughout this thesis to determine the spin state. Option (2) is proposed in Chapter 4 as a possible improvement.

2.3.1. 'ELZERMAN' READ-OUT

In section 2.2.1 we observed that the $|\uparrow\rangle$ and $|\downarrow\rangle$ state differ in energy by ΔE_z. The spin levels can be leveled around the electrochemical potential of the reservoir μ_{res} as depicted in Fig. 2.7. A $|\downarrow\rangle$ has enough energy to tunnel out of the dot into the reservoir, whilst a $|\uparrow\rangle$ does not. An electron leaving the dot can be detected using a nearby charge sensor such as a sensing dot. After some time which depends on the tunnel rate with the reservoir, the dot will be filled again with a $|\uparrow\rangle$. This method requires an external magnetic field that is significantly larger than the thermal broadening of the reservoir. A detailed discussion on the read-out fidelity of this approach is described in section 4.6.1.

2.3.2. PAULI SPIN BLOCKADE READ-OUT

An alternative way to convert spin to charge consists of performing a parity check of two neighbouring spins. Using the energy diagram of Fig. 2.6 one can create a pulse scheme that starts in the charge state (1,1), and next pulses to the (0,2)-state. Under the right conditions, only anti-parallel spin states will enter the (0,2)-regime, while parallel spin states remain in the (1,1) charge state. The outcome of such a pulse, (1,1) or (0,2), can once again be distinguished using a charge sensor [29, 49].

The details of such a scheme are as follows: for the parallel spin states, $T_-(1,1)$ and $T_+(1,1)$, the tunnel transition to (0,2) is forbidden as the $T_-(0,2)$ and $T_+(0,2)$ are much higher in energy because of the Pauli exclusion principle. This effect is termed Pauli Spin Blockade and results in a charge sensor signal corresponding to (1,1) for the parallel states. The anti-parallel state $S(1,1)$ can tunnel into $S(0,2)$ directly. The other anti-parallel state $T_0(1,1)$ cannot tunnel directly, however, due to the nuclear fields the $T_0(1,1)$ and $S(1,1)$ will rapidly mix and any $S(1,1)$-portion will quickly decay to $S(0,2)$ [50, 51]. Therefore, both anti-parallel spin states will result in a (0,2) charge sensor signal.

3

DEVICE FABRICATION AND EXPERIMENTAL SETUP

This chapter discusses the recipe for device fabrication and describes details of the experimental setups that were used to obtain the experimental results.

3.1. DEVICE FABRICATION

Starting from a wafer as described in section 2.1, the following steps need to be taken in the cleanroom facility to create laterally defined quantum dots:

1. Clean the wafer.
2. Optically inspect the wafer for 'cracks'. Typically each wafer has cracks several cm long with height differences of ~50 nm. Adjust alignment markers (step 3) in such a way as to avoid fabricating across cracks.
3. Dice the wafer.
4. Deposit alignment markers using electron-beam lithography (ebeam). These markers form the corner stones of each unit cell of a device. The following ebeam steps can then be aligned with respect to these markers, see Fig. 3.1a.
5. Define and etch a mesa. As a result, the 2DEG is removed everywhere where it is not required. This has several benefits: it reduces current leakage from large surface areas of the gate to the 2DEG, it reduces damping of high frequency signals in the 2DEG (including possible heating effects) and it disconnects the ohmic contacts from one another, see Fig. 3.1b.
6. Create ohmic contacts to the 2DEG, see Fig. 3.1c. In this way currents through the qubit array and sensing dot can be measured for e.g. charge stability diagrams or spin detection.
7. Pattern the fine gates. These gates are the nano- and microscale pattern that create the dot array, see Fig. 3.1d.
8. Pattern the large gates. These gates are continuations of the fine gates to the bonding pads such that external wire bonds can be attached, see Fig. 3.1e.

Details of this recipe can be found in the Appendix A. Once a batch is finished (typically in the form of an array of identical devices), we dice it using a Disco Dicer into individual devices. A device is then glued onto a printed circuit board (PCB) using either PMMA (quadruple-dot device) or two-component glue (triple-dot device). Electrical connections between the bond pads of the device and the PCB are made using wire bonds (aluminium wire), see Fig. 3.1f. The triple-dot device described in this thesis has been fabricated by F.R. Braakman, the quadruple-dot device by T.A. Baart. It took multiple batches of samples made on different wafer material to find stable samples (i.e. with no charge switches). In our experience different parts of the wafer can give very different results: stable devices on one part, do not guarantee stable devices on another quarter of the same wafer. During the etching of the mesa or the annealing of the ohmic contacts, variations in device behaviour are already observed. The etch rates and ohmic contacts' resistances (room temperature) can vary across the wafer. Screening the samples for stable QPC-behaviour at 4K using a dipstick can be time-saving before cooling down in a dilution refrigerator that does not have a fast sample loader. We unfortunately do not have a tool to predict at room temperature how stable devices will be at low temperature.

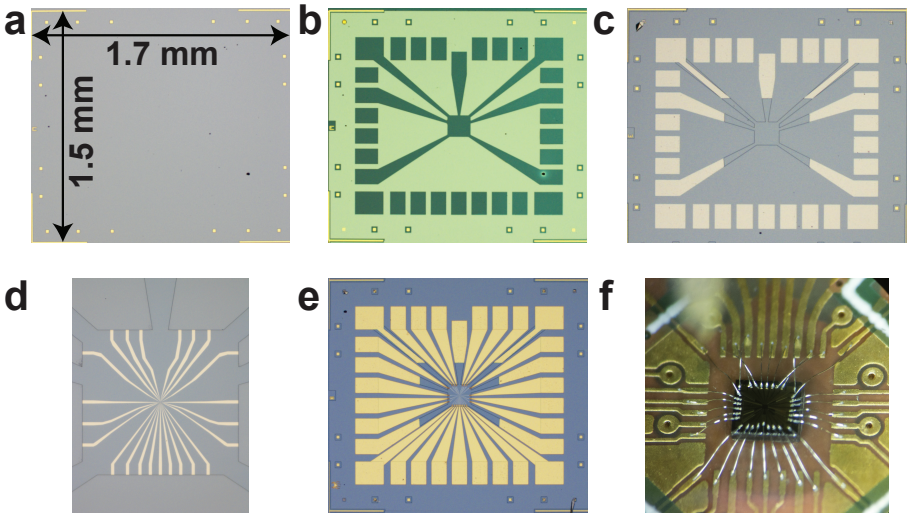

Figure 3.1: (a-e) Optical pictures of the sample after performing several of the steps of the fabrication recipe. (a) Step 4: deposit alignment markers. (b) Step 5: etch mesa. (c) Step 6: create ohmic contacts to the 2DEG. (d) Step 7: pattern the fine gates defining the qubit array. (e) Step 8: pattern the large gates with bond pads. (f) The quadruple-dot sample is glued upon a PCB. Electrical connections between sample and PCB are made using a wirebonder.

We lack statistics to specify the yield of fabrication that delivers stable samples, but at the moment it can best be described as low. Future improvements on this issue would be very beneficial to help this field forward. Currently the feedback loop between growing a wafer and measuring an actual device is slow. It can easily take more than one year before a grower receives feedback on the wafer they have made. When a stable device has been found, we tend to measure it for more than two years; thereby blocking any further feedback. Currently several growers are building low-temperature measurement setups to characterize devices themselves and thereby speed up the feedback loop.

3.2. EXPERIMENTAL SETUP

In this section the essential parts of an experimental setup to perform spin-qubit experiments are described: (1) dilution refrigerators to sufficiently suppress thermal excitations and (2) the measurement electronics to probe the physics that occurs at the quantum dots.

3.2.1. DILUTION REFRIGERATORS

In order to bind electrons to a well-defined 2DEG and create lateral quantum dots it is essential to cool down the samples to low temperatures so that thermal excitations are suppressed. This regime can be attained for temperatures on the order of 1 K. For most experiments we also want to perform single-shot read-out of the spin states through spin-to-charge conversion (section 2.3). This last requirement gives the upper bound for the temperature of the electrons in the reservoir. Their thermal energy should be sig-

nificantly smaller than the Zeeman energy: $4k_BT < g\mu_B B$. For typical fields of ~ 4 T this requires electron temperatures below 250 mK. The samples are therefore cooled down in dilution refrigerators. The triple-dot device in a Oxford Kelvinox 400HA wet system to a base temperature of ~ 45 mK[1] and the quadruple-dot device in a Oxford Triton 400 dry fridge to a base temperature of ~ 15 mK (for both fridges with cryogenic amplifier at the 4K-stage turned on). The lattice phonons of the semiconductor are thermalized to the base temperature. The electrons in the 2DEG will however be hotter. This is due to thermal contact of the 2DEG with warmer parts of the setup through measurement wires and electrical interference reaching the sample through the wiring. To lower the electron temperature the wires are thermally anchored at several stages inside the fridge and electrically filtered (details can be found in section 3.2.2). The triple-dot sample is protected from 4K radiation of the inner vacuum chamber (IVC) by mounting the device inside a copper can that is connected to the mixing chamber (MC) plate via the cold finger, see Fig. 3.2b. In the triple-dot experiments the electron temperature was measured to be ~ 75 mK. The quadruple-dot sample is also mounted inside a metal can (the IARPA-puck) which is connected to the MC-plate to shield against radiation. In addition this copper can is surrounded by a metal shield that is connected to the still shield (~ 650 mK). The electron temperature of the quadruple-dot device has not been measured accurately but single shot read-out worked properly at 3.5 T indicating that electron temperature should be ≤ 250 mK.

The Kelvinox system is equipped with a superconducting magnet that can run up to 14 T, the Triton up to 10 T.

3.2.2. MEASUREMENT ELECTRONICS

The measurement electronics form an essential element in performing proper experiments. The challenge is to design the electronics in such a way that the measurement bandwidth is large enough to detect (and manipulate) spin states before the qubit has relaxed (or dephased), whilst on the other hand limiting back-action from the measurement electronics that could influence the qubit state. Broadly speaking we need the following elements for our experiments: (1) A PCB is used as an interconnect between the sample and the external control wires. (2) DC-electronics (a) to bias the gates such that we can create lateral quantum dots. And (b) the ability to perform transport measurements to determine for example the pinch-off values of the gates and to start the creation of single dots (see for example Chapter 6). (3) High-frequency pulses to quickly (~ns) change the electrochemical potential in the dots and also microwave signals to perform EDSR to change the spin state or photon-assisted tunneling measurements to determine tunnel couplings. (4) Radio-frequency (RF) reflectometry to probe the conductance of the charge sensors with high measurement bandwidth. This allows us to measure charge stability diagrams in a fast way, and perform single-shot readout of the spin states with high read-out fidelity.

[1] At the start of the experiments the Kelvinox 400HA had a base temperature ~ 100 mK (no cryogenic amplifier installed). This required large magnetic fields and consequently leads to large Larmor frequencies of the electron spin (>20 GHz). The attenuation of coax lines and PCB is very high at such large frequencies (>20 dB) making it hard to drive the electron spin. The T_1 will also be low [26] which reduces a.o. read-out fidelities. The solution was to replace the old coax lines made from Nb with NbTi coax lines which have a lower heat conductivity. Details are described in section 3.6 of Ref. [52].

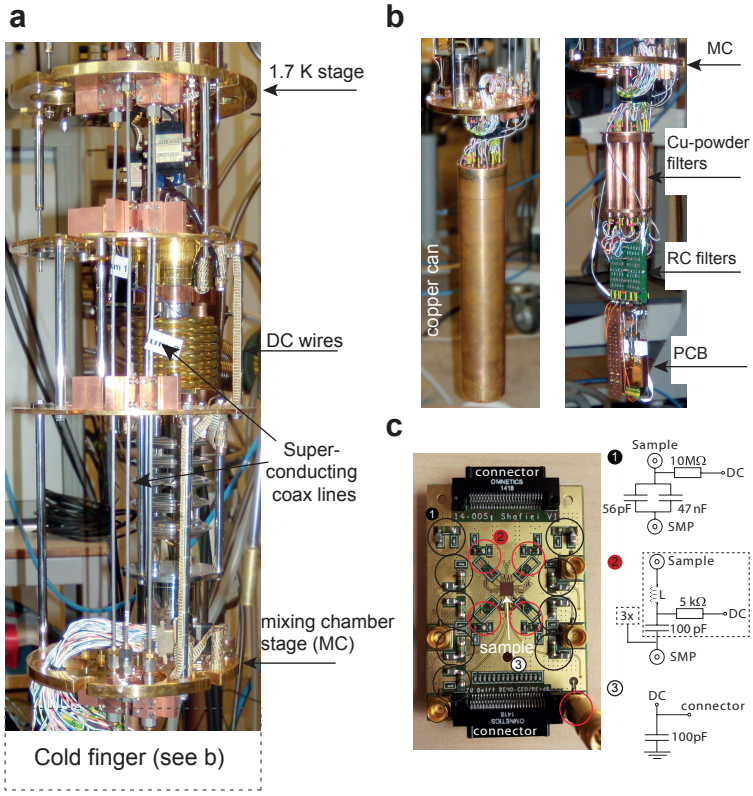

Figure 3.2: (a) Insert of the Oxford Kelvinox 400HA refrigerator from the 1.7K-stage to the mixing chamber. (b) Cold finger with (left) and without (right) the copper can. RC-filters, Cu-power filters and PCB are all positioned inside the copper can. (c) PCB used for the quadruple-dot measurements. The sample (not shown on picture) is connected through wire bonds with the PCB. DC lines are filtered with 100 pF (3) to ground to reduce cross-talk between the waveguides on the PCB and the DC-lines. 9 high-frequency lines (1) are connected via bias-tees. RF-readout (section 3.2.2) is done by multiplexing 4 lines, each with their own inductor value L (2).

(1) PRINTED CIRCUIT BOARD (PCB)

Fig. 3.2c shows a PCB[2] used for the quadruple-dot experiment before the sample is glued[3]. This PCB has 48 DC lines that are each filtered with 100 pF to ground. Up to 9 high-frequency lines can be connected using the SMP connectors. These lines are combined with a DC-bias using the bias-tees each with a RC-time constant of ~ 470 ms. This allows us to apply fast pulses, up to microwave frequencies, to the same gates that are used to define the lateral quantum dots. The settling time of 470 ms is a trade-off between tuning-speed of the lateral quantum dots versus maximum total length of pulses

[2] This PCB has been designed in collaboration with Raymond Schouten, Rogier van den Berg and Mohammad Shafiei.

[3] For the triple-dot device we used a different PCB. Its characteristics are very similar (same bias-tee values etc.) except for fewer high-frequency lines (4) and DC-wires (31). The high frequency connectors are 2x SMA and 2x SMK instead of SMP.

without significant distortions.

For RF-readout we split one coax line into four LC-tank circuits that are each connected to a different ohmic contact. Using frequency multiplexing we can read out the conductance of each individual sensing dot, see section 3.2.2 for details.

(2) MEASUREMENT ELECTRONICS: DC

Most of the DC-measurement electronics and filters were designed and home-built by Raymond Schouten and the electronics workshop of the Delft University of Technology (DEMO). Fig. 3.3 shows a schematic of the electrical scheme used for the triple-dot measurements. The DC-electronics consist mainly of (1) digital-to-analog converters (DACs), (2) optically isolated voltage sources and (3) current-to-voltage (IV) converters.

The gates of our samples are biased using 16bit DACs providing voltages from -2 V to 2 V with a resolution of ~ 60 μV. For the plunger gates we combine two DACs of which one DAC is voltage-divided by a factor of 100 to give a resolution of ~ 600 nV. This allows for very precise tuning of the electrochemical potential of the dots. The DC-electronics are all galvanically isolated from a large part of the measurement setup, including the measurement computer. Communication between the DACs and the computer occurs via an optical fibre. External measurement equipment, such as a Keithley multimeter, are connected via opto-couplers. The DC-electronics are battery-powered.

DC-wires going to the sample are filtered in several stages. At room temperature they first go either through a Pi-filter[4] or through a capacitive feedthrough[5]. The Pi-filters operate from 10 MHz (5 dB attenuation) to 10 GHz (70 dB attenuation). Next they go through Cu-powder filters that are capable of attenuating frequencies at the higher end of the spectrum (more than 60 dB for frequencies in the range 1-50 GHz). A Cu-powder filter consists of a 2 m long wire wound up in a tube filled with copper powder. High frequency signals are attenuated via eddy currents created inside the copper grains. The final stage of filtering is either a second-order RC-filter with a cut-off frequency of 20 Hz for wires connected to the gates, or a first-order RC-filter with a cut-off frequency of 1.3 MHz for the wires connected to the ohmic contacts. The wires are thermally anchored at several stages and fixed to the fridge to minimize vibration-induced voltages by triboelectric effects or flux-induced currents due to imperfect twisted pairs.

To minimize the heat load, the DC-wires going to the sample are thin and from the 1.7K-plate to the MC they are superconducting wires resulting in a very small heat conductivity. For the high temperature part of the DC-wire two types of materials have been used: constantan and copper. The constantan wires have a lower heat conductivity than copper, but as a trade-off their resistance is higher: 117 Ω versus 5 Ω respectively. The constantan wires are connected to the gates. The copper wires are used to contact the ohmic contacts in order to reduce the Johnson noise in the wire. We also sacrificed part of the filtering of these wires to reduce the capacitance which limited the measurement bandwidth using our room temperature IV-converter[6]. These so-called fast lines can then be used for single-shot measurements with a bandwidth of ~ 40 kHz [53]. However,

[4] TUSONIX-4209-003LF-FILTER, PI-SECTION, 1500 pF, 350 V, 10 A

[5] TUSONIX-2499-003-U2MO-101KLF-FILTER

[6] Note that as a result of line capacitance, the output voltage-noise of the IV-converter increases as a function of frequency.

during the course of experiments we added the ability of performing RF-readout which was superior to the fast lines and therefore these lines were not used anymore for spin detection.

Transport measurements through the qubit array or through a sensing dot are performed by applying a bias voltage between two ohmic contacts ($\sim 500\ \mu$V) and measuring the current through them using an IV-converter. Several of the ohmic contacts of the triple-dot device were directly connected to the cold ground with the aim of achieving lower electron temperatures. These were then used as the drain of the current path. By biasing the ground of the IV-converter we could then effectively bias, and measure the current, through one ohmic contact. The voltage source is referenced with respect to the ground at cold to reduce effects of thermal voltage differences. We use twisted pairs for current-carrying wires to minimize the surface area of the loop that may pick up magnetic interference.

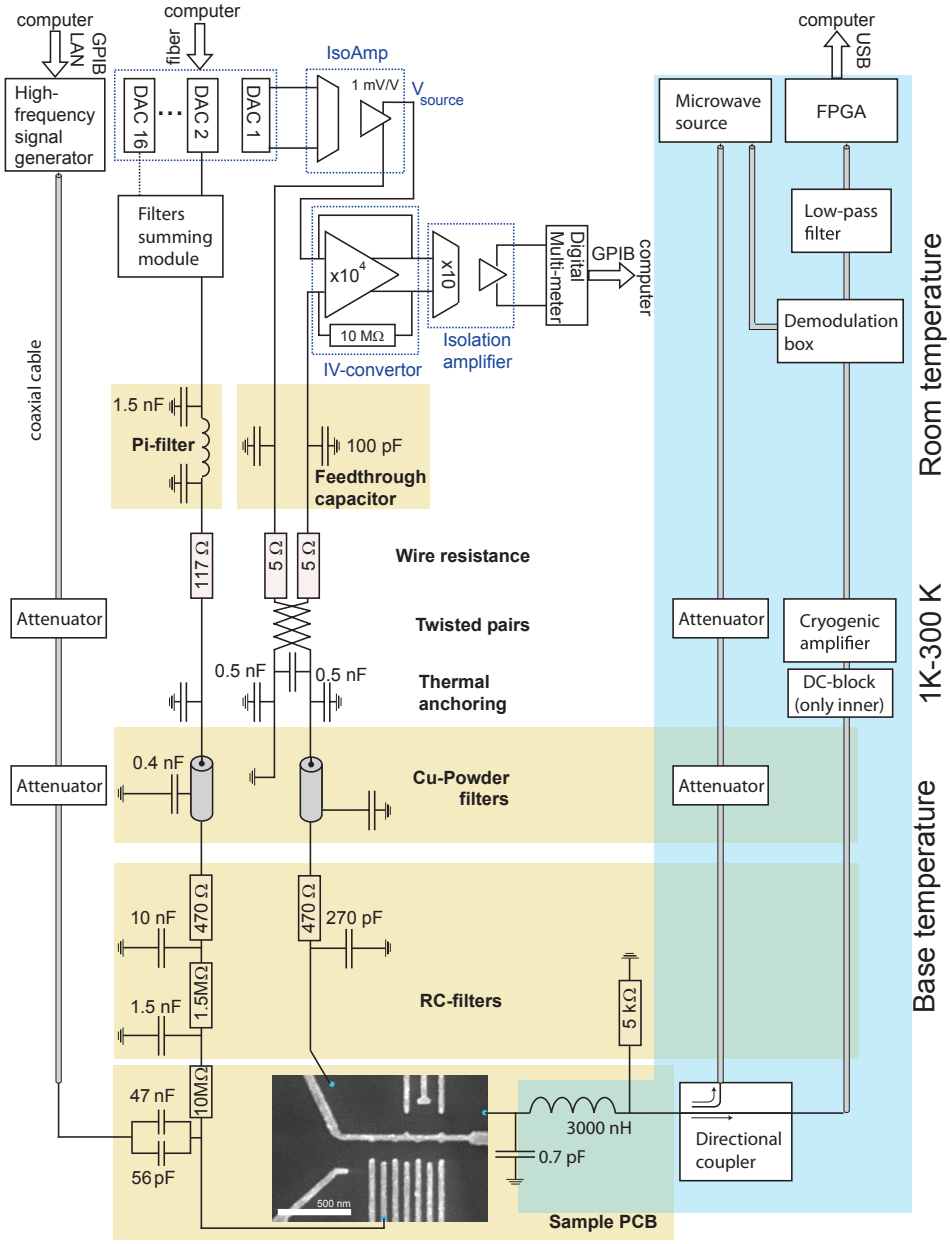

Figure 3.3: Schematic overview of the electric circuit of the triple-dot measurement setup. A very similar approach is used for the quadruple-dot. The main difference is that the Cu-powder filters have been replaced by a series of 4 Pi-filters at the MC-stage for each DC-line: a Mini-Circuits LFCN-5000, LFCN-2750, LFCN-1450 and LFCN-80 Pi-filter.

(3) MEASUREMENT ELECTRONICS: RF

The high frequency lines are used to either apply microwaves up to 40 GHz, or apply fast pulses down to the ns-timescale. These signals are added to the DC-bias using the bias-tees on the PCB. In the Kelvinox setup there are four coax lines. They consist of three parts: (1) semi-rigid Keycom ULT-05 from room temperature to 1.7 K (outer diameter 2.2 mm; inner conductor: silver-plated brass; outer conductor: stainless steel (SUS304) with a 5 μm layer of copper). The outer conductor has been thermally anchored at the 4 K and 1.7 K stages of the fridge. At the 1.7 K stage we additionally use attenuators[7,8] to (a) anchor the inner conductor and (b) reduce thermal noise coming from room temperature to the Johnson noise at the 1.7 K plate. You typically need 20 dB of attenuation if the temperature changes by a factor of 100. (2) 34 mm long superconducting Keycom NbTi coaxes from the 1.7 K plate to the MC-plate. The outer part of the coax is anchored in all stages from the 1.7 K plate to the MC. The inner part is anchored at the MC-plate using 3 dB attenuators. The value of 3 dB is a compromise: it is too low to fully reduce the Johnson noise coming from 1.7 K, but more attenuation would limit the possible signal range from the AWG and/or microwave source too much. (3) 40 cm flexible tin-plated copper coaxes are used from the MC to the PCB connectors. The quadruple-dot setup consists of a similar approach only with the addition of 4 coax lines that are attenuated with 40 dB in total.

Voltage pulses are created using an arbitrary waveform generator (AWG): Tektronix AWG5014. The output of the AWG is filtered with a low-pass filter[9].

Coax lines connected to the MW-source (HP83650A) are filtered with a DC-block[10] (both outer and inner conductor). This is to prevent ground loops and block low-frequency noise coming from the generator into the sample. Coax lines connected to the AWG do not have such a DC-block as the pulses used are also in the low-frequency range.

(4) READ-OUT REFLECTOMETRY SETUP

At the start of work described in this thesis we used a room-temperature IV-converter to perform charge- and spin-detection measurements. The detection bandwidth of this system was limited by the low-pass filter formed by the parasitic capacitance of the DC wire and the Cu-powder filter of about 1 nF, and the input impedance of the IV-converter (1 kΩ). This limited the bandwidth to $\mathrm{BW}_{\mathrm{det}} = 1/(2\pi RC) \approx 160$ kHz. The operation speed was not limited by $\mathrm{BW}_{\mathrm{det}}$ however, but by voltage noise in the system that increased as a function of frequency. In first approximation the voltage noise at the input of the amplifier (v_i) is frequency independent. The voltage noise at the output is given by $Z_{\mathrm{feedbackresistor}}/Z_{\mathrm{input}} \cdot v_i$, where Z_{input} is formed by the impedance connected to the input of the amplifier. Z_{input} includes the parasitic capacitance of the line, which already

[7] Two 20 dB Agilent attenuators with V-connectors and two 20 dB XMA attenuator with SMA connectors, type number 2682-460-20.

[8] Practical advice: before changing the attenuators do check if they work at 4 K by immersing them in liquid helium. Even though the attenuators are specified to work at low temperature, several of them became superconducting.

[9] SBLP-300+ Mini-Circuits

[10] Pasternack PE8227

at low frequencies (~ 15 Hz) has a similar impedance as the feedback resistor. The measured signal therefore typically had to be low-pass filtered at around 40 kHz.

In order to operate with a higher measurement bandwidth we decided to move to RF-readout using a *RLC* tank circuit [54]. The R is formed by the charge sensor, the L by an inductor and the C by the parasitic capacitance, C_p, of connections between the inductor and the sample. Combined they allow to either absorb of reflect a specific carrier wave RF-frequency (~100 MHz) depending on the conductance of the charge sensor; details will be described below. The reflected carrier wave is amplified and subsequently demodulated with a local oscillator wave at the carrier frequency to create the two quadratures of the charge sensor signal.

By using a low-impedance (50 Ω) high-frequency amplifier the capacitance of the cabling between the SD and the amplifier becomes unimportant [55]. If the used coax cables have the same impedance of 50 Ω, then the total impedance of coax cables and amplifier remains purely real and 50 Ω. Moreover, encoding the information on top of a carrier wave at high frequency has another advantage. During the demodulation stage, we only extract a signal of finite bandwidth (~MHz) around the carrier frequency. So any noise or interference coupling in outside that range, such as 50 Hz-interference, $1/f$-noise originating from the amplifier, or slow mechanical vibrations that are converted to electrical noise (e.g. through the triboelectric effect) will be filtered out. Using RF-readout we managed to achieve ~1 MHz measurement bandwidth which was very beneficial to achieve high read-out fidelities and faster measurements in general.

Matching Circuitry

At radio frequencies the physical dimensions of the measurement wires have the same order of magnitude as the electrical wavelength. It is therefore no longer possible to model the system using a lumped element approach as signals behave like electromagnetic waves that can scatter and reflect in the network. When a wave travels through a transmission line and hits a resistor (e.g. a sensing dot), part of the wave is reflected back in the coaxial cable. The complex voltage reflection coefficient Γ that describes the amplitude and phase of this reflected wave is given by:

$$\Gamma = \frac{Z_L - Z_0}{Z_L + Z_0}, \tag{3.1}$$

where Z_L is the impedance of the load, typically the charge sensor, and Z_0 the impedance of the transmission line. From this equation it follows that all power is absorbed by the charge sensor if $Z_L = Z_0$. The sensing dot typically has the largest charge sensitivity, $\frac{dZ}{dq}$, at the flank of a Coulomb peak which corresponds to a resistance of roughly 125 kΩ. Using a normal set of coax lines with $Z_0 = 50$ Ω, one would end up with a system that always reflects the wave and has a poor signal-to-noise ratio (SNR).

The aim is to maximize the product of the power delivered to the charge sensor, κ, and $\frac{dZ}{dq}$ [56]. As a solution one can use a so-called matching circuit to transform an arbitrary Z_L into an equivalent impedance of 50 Ω, such that the charge sensor can be used at its optimal $\frac{dZ}{dq}$. One of the most straightforward examples of such matching circuit consists of a capacitor and an inductor (see Fig. 3.4a) and is often referred to as LCR network. On resonance, $\omega \approx \frac{1}{\sqrt{LC}}$, the equivalent impedance of the load and the

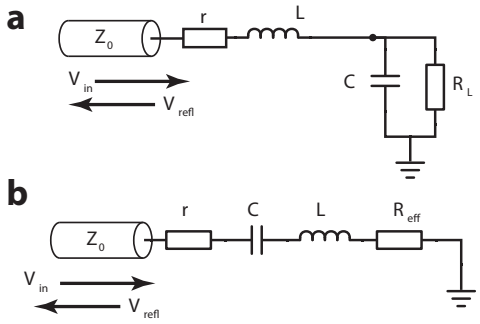

Figure 3.4: (a) A LCR network to match an arbitrary load R_L to a transmission line. r represents a resistance to model losses in the matching circuit. (b) At resonance, this circuit can be simplified using the series approximation.

matching circuit combined can be approximated by:

$$Z_{\text{eq}} = \frac{L}{RC} \equiv R_{\text{eff}} \tag{3.2}$$

The circuit can then be simplified using the series approximation as shown in Fig. 3.4b. With a proper choice of L and C, it is in principle possible to match any arbitrary load. When this is the case, all the power is dissipated in the purely resistive load. A simple way to model losses in the matching circuit is by adding a series resistance r. Z_{eq} then becomes:

$$Z_{\text{eq}} = \frac{L}{RC} + r \tag{3.3}$$

For typical experimental conditions the value of C is roughly 0.5 pF requiring $L \approx 3\ \mu$H to match a sensing dot of 125 kΩ at a frequency of 120 MHz. Commercially available surface mount inductors (SMD) consist of a coil of copper wire and are available over a very broad range. Unfortunately such SMD inductors have a drawback for L larger than ~1 μH. As the resistive copper wire gets larger, the losses r increase and the self-resonance frequency (SRF) of the inductor decreases which only allows one to do reflectometry at low frequencies. For example, a *CoilCraft* 1008CS inductor of 3.3 μH has a SRF of 110 MHz making it unsuitable to match a sensing dot when using similar frequencies for the detection. As a solution we fabricated superconducting spiral inductors made of NbTiN on a substrate of quartz[11]. These resonators ideally have $r = 0$ and high SRFs. Details of the spiral inductor recipe can be found in Appendix B. An optical image of such an inductor is shown in Fig. 3.5. We have verified that these inductors work in high magnetic field, a critical requirement for spin qubit experiments. We have performed single-shot read-out in fields up to 8 T using these inductors. We do notice that as the magnetic field is increased, that the resonance frequency decreases by roughly ~1 – 3 MHz/T and that the SNR tends to decrease. We did not observe any SRF up to the

[11] Quartz has a relatively low dielectic constant of $\epsilon = 3.78$ and low loss tangent of $\tan\delta = 0.0001$ making it a suitable substrate material.

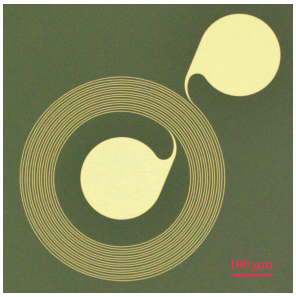

Figure 3.5: An optical microscope image of a NbTiN inductor on a quartz substrate. The turns are 2 μm wide and spaced by 4 μm. By varying the number of turns, inductors can be made ranging from 20 nH to 8 μH. The large pads have a radius of 100 μm and are used for bonding.

GHz regime.

RF-readout setup

The right (blue) side of Fig. 3.3 depicts the RF-readout part of the setup. Details are as follows: The amplifier is a SiGe low noise cryogenic CITLF2 amplifier from the Caltech Microwave Research Group. We installed a DC-block[12] before the input of the amplifier to physically disconnect the inner conductor of amplifier and the coax connected to the sample in order to reduce thermal contact. The directional coupler[13] is mounted on the MC. The incoming carrier wave is attenuated by a 20 dB attenuator[14] at 1-4 K and another 20 dB at the MC. Combined with the directional coupling factor of 15 dB this gives a total attenuation of 55 dB for the carrier wave. The reflected signal is demodulated by a home-built demodulator. Fig. 3.6 shows the schematic diagram of a demodulator that can demodulate two separate carrier waves allowing one to read-out two charge sensors simultaneously.

Practical tips & tricks

During the development of the RF-readout at Delft we encountered several practical challenges. We summarize the main points here including their solutions.

- In the beginning we used silver paint to glue the spiral inductors on the PCB. This conductive glue however was a significant source of signal loss so do not use conductive glue but for example PMMA instead.
- If the resistance of the ohmic contacts is large in DC-measurements (~1 MΩ), it is still possible that the RF-readout works even though one may at first sight expect that all the signal will be reflected. This may be explained by a shunt capacitance somewhere along the ohmic contact that has a high DC-impedance.
- Bonding the sample to the tank circuit typically adds 0.15 pF of capacitance to the C_p of the PCB.

[12] Pasternack PE8210
[13] Mini-Circuits ZEDC-15-2B
[14] XMA 2682-6460-20 Cryo

- The power sent to the sample should typically be between -85 to -105 dBm. The exact value is chosen to be the highest power for which no back-action was observed on the spin or charge state.

Future improvements
Changing from DC- to RF-readout increased our measurement bandwidth by a factor 25, allowing us to perform a variety of new experiments. In order to improve the system further, it is important to investigate what currently limits the measurement bandwidth. This is something that still needs to be done. Depending on the outcome, possible improvements could include:

- Adding a varactor diode to the tank circuit to allow in situ tuning of the capacitance [56]. Before the cooldown we estimate as well as possible what L and C_p will be at low temperature[15], and we assume the charge sensor will work optimally at 125 kΩ. It is hard to estimate these parameters accurately though, and it would be very beneficial if one can change C in situ at low temperature to always ensure the matching condition for the most sensitive charge sensor tuning. This can be achieved by adding a varactor diode to the tank circuit.

- Increase the signal bandwidth by working at higher frequencies. Current experiments are performed with carrier waves with a frequency of ~100 MHz and tank circuit quality factors of 20 to 40 limiting the signal bandwidth to ~5 MHz. Increasing the resonance frequency would allow a larger signal bandwidth, and also gives room to multiplex more signals on one coaxial line. There are several ways to increase the resonator frequency. (1) C_p can be reduced for example by bonding directly from the inductor to the sample. In this way you can skip the transmission line between the inductor and the sample. (2) Design more complex tank circuits using for example two inductors. By selecting the right value of the second inductor, it is possible to cancel excess capacitance at resonance [57]. (3) Using terminated transmission lines (stubs) in the vicinity of the sample to match the charge sensor. Experimental work shows that a QPC channel can be matched at 3 GHz [58].

3.2.3. REMOTE CONTROL OF THE INSTRUMENTS

All the measurement electronics were controlled through the QTlab environment. QTlab is a IPython-based measurement environment developed by Pieter de Groot and Reinier Heeres[16]. We have developed Python modules to perform the experiments described in this thesis.

[15] We currently estimate C_p based on 4 K measurements of the LC-resonance of the PCB without sample. Based on previous cooldowns, we then estimate what the C_p becomes including the bonded sample at mK temperatures.

[16] available at `http://qtlab.sourceforge.net/`

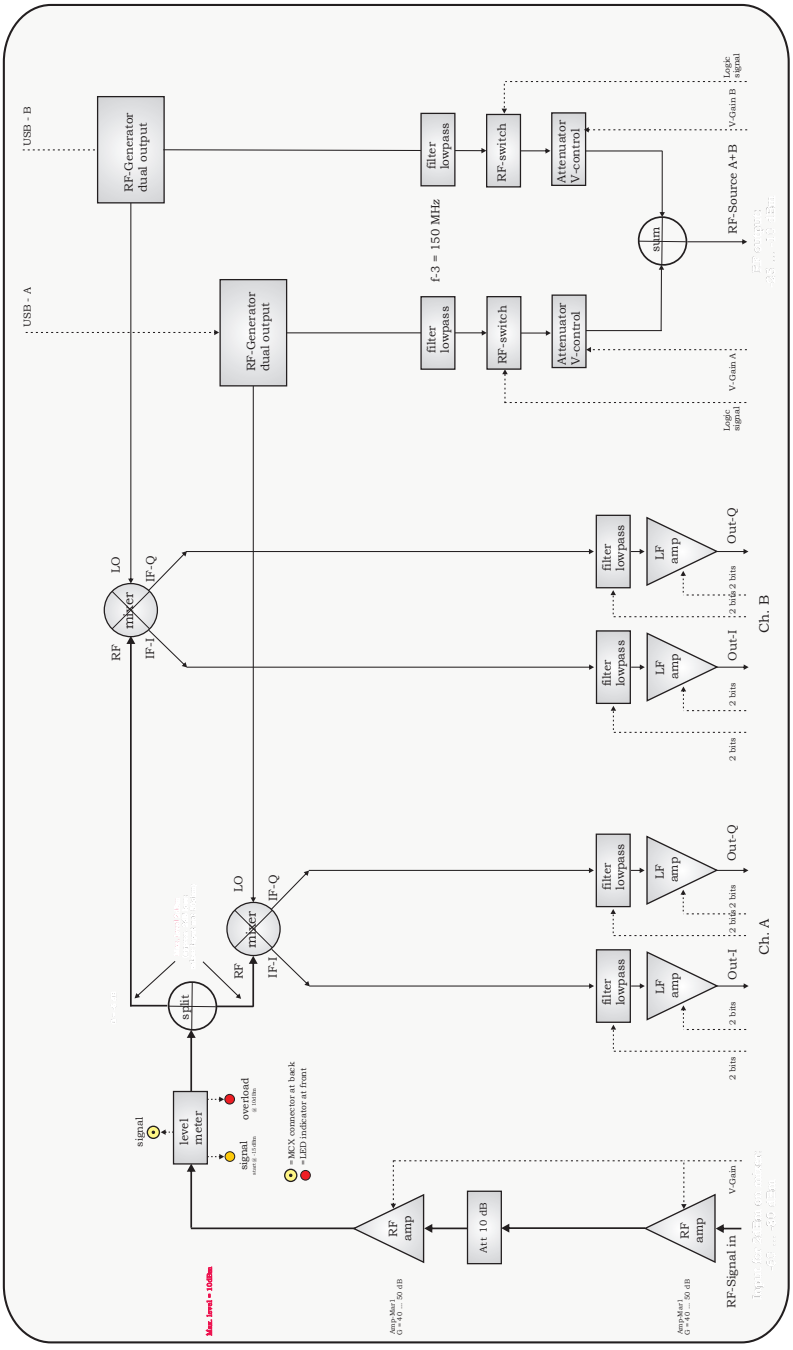

Figure 3.6: Schematic of the demodulation part of the RF-readout setup. This is an example of a double demodulator that can send, and demodulate two separate carrier waves. It outputs both the quadratures for each carrier wave. This box has been home-built by Ruud van Ooijik and Raymond Schouten and was used in the quadruple-dot experiments. The triple-dot experiments used a similar box supporting only one carrier wave.

4

SINGLE-SPIN CCD

T.A. Baart, M. Shafiei, T. Fujita, C. Reichl, W. Wegscheider and L.M.K. Vandersypen

Spin-based electronics or spintronics relies on the ability to store, transport and manipulate electron spin polarization with great precision [59–62]. In its ultimate limit, information is stored in the spin state of a single electron, at which point also quantum information processing becomes a possibility [63, 64]. Here we demonstrate the manipulation, transport and read-out of individual electron spins in a linear array of three semiconductor quantum dots. First, we demonstrate single-shot read-out of three spins with fidelities of 97% on average, using an approach analogous to the operation of a charge-coupled-device (CCD) [65]. Next, we perform site-selective control of the three spins thereby writing the content of each pixel of this "Single-Spin CCD". Finally, we show that shuttling an electron back and forth in the array hundreds of times, covering a cumulative distance of 80 μm, has negligible influence on its spin projection. Extrapolating these results to the case of much larger arrays, points at a diverse range of potential applications, from quantum information to imaging and sensing.

This chapter has been published as T.A. Baart, M. Shafiei, T. Fujita, C. Reichl, W. Wegscheider and L.M.K. Vandersypen, Single-spin CCD, *Nature Nanotechnology* **11**, 330-334 (2016).

4.1. INTRODUCTION

Past experiments have shown *macroscopic* spin transport over distances exceeding 100 μm in clean bulk 2D semiconductors [66, 67]. Furthermore, controlled single electron transport through semiconductor nanostructures [21] is now routine, with applications ranging from current standards to sensors and digital electronics [68]. Also the controlled transfer of individual electrons between nanostructures separated by several micron has been realized [69, 70]. However, the key combination of single-electron transport and spin preservation over large distances remains to be demonstrated.

A promising platform for moving around individual spins in a controlled manner is provided by analogy to a CCD [65]. In a CCD, pockets of electrical charge are passed on along a capacitor array that acts as a shift-register, similar in spirit to a bucket-brigade. The pockets of charge arrive sequentially at the end of the array, where they are detected via a charge amplifier. This simple concept has enabled CCD camera's containing millions of pixels with applications from consumer electronics to astronomy [71]. The creation of an analogous device that can operate and detect single spins would have powerful and diverse applications as well. For instance, it would not only enable reading out the outcome of a large quantum simulation or computation performed in a 2D array of spins [64, 72], but also could be used for coherent imaging at the single photon level [73, 74] or magnetic field sensing with 200 nm spatial resolution, using each single spin as a local probe. We term such a device a Single-Spin CCD. Its operation requires the ability to shuttle spins one by one along a chain of sites without disturbing the spin states, and to record the state of the spin at the end of the chain.

4.2. OPERATING A PROTOTYPE SINGLE-SPIN CCD

We have created a prototype Single-Spin CCD using a linear triple quantum dot array. The array is formed electrostatically in a 2D electron gas (2DEG) 85 nm below the surface, see Fig. 4.1a. Gate electrodes fabricated on the surface of a GaAs/AlGaAs heterostructure (see Methods) are biased with appropriate voltages to selectively deplete regions of the 2DEG and define the linear array of three quantum dots. Each dot is initially occupied with one electron, and each of the three electrons constitutes a single spin-$\frac{1}{2}$ particle. The sensing dot (SD) next to the quantum dot array is used for non-invasive charge sensing using radiofrequency (RF) reflectometry to monitor the number of electrons in each dot [75]. An in-plane magnetic field B_{ext} = 3.51 T is applied to split the spin-up (↑) and spin-down (↓) states of each electron by the Zeeman energy ($E_Z \approx 87$ μeV) defining a qubit in each of the dots. The electron temperature is 75 mK.

The CCD is initialized by loading ↑-spins from the right reservoir to every dot as described by the schematic diagrams of Fig. 4.1b, which are implemented via the pulse sequence depicted by the arrows in Figs. 4.1cd. Once the desired spin manipulation has been performed (see below) in the (1,1,1)-regime, the read-out sequence is started. This sequence follows the reverse path from the loading sequence, with the addition of three read-out positions that are denoted by green circles. As in a CCD, the three electrons are pushed sequentially to the read-out site at the end of the chain. First, the right dot is tuned to the position of green circle nr. 3 in Fig. 4.1d. At this position, an excited spin-↓ electron is allowed to tunnel to the reservoir, whilst a ground state spin-↑ electron will

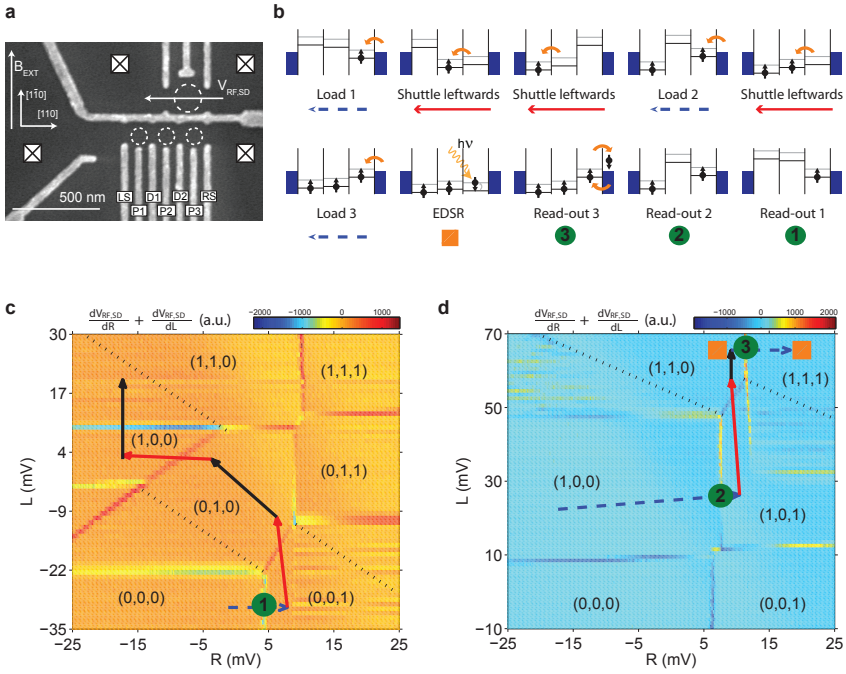

Figure 4.1: Linear array of three quantum dots and Single-Spin CCD operation. **a** SEM image of a sample nominally identical to the one used for the measurements. Dotted circles indicate quantum dots, squares indicate Fermi reservoirs in the 2DEG, which are connected to ohmic contacts. The RF reflectance of the SD is monitored in order to determine the occupancies of the triple dot. **b** Read from left to right and top to bottom. The CCD is initialized by loading three electrons from the right reservoir and shuttling them to their final position (analogous to a shift-register). We load ↑-spins by ramping slowly through the charge transition lines with the right reservoir (slow compared to the tunnel rate with the reservoir). Single-spin manipulation can be performed through EDSR. Read-out occurs using spin-selective tunneling. **c,d** Charge stability diagram of the triple dot for two different values of M (**c** M = -42 mV, **d** M = -56 mV). L, M and R are linear combinations of the voltages applied to gates P_1, P_2 and P_3, allowing us to partially compensate for cross-capacitances (see Additional Material 4.6.5). L, M and R therefore couple mostly to the left, middle and right dot respectively. The occupancy of each dot is denoted by (n,m,p) corresponding to the number of electrons in the left, middle and right dot respectively. The fading of the middle dot charge transition lines can be explained in a similar way as in Ref. 23 (black dotted lines indicate their positions). The pulse sequence for loading and read-out is indicated in the charge stability diagrams via arrows, see also panel b. From panel c to d, we pulse M keeping L and R the same.

remain in the dot. The nearby sensing dot is used to record whether or not the electron tunneled out, revealing its spin state [47]. Next, we adjust the gate voltages to shuttle the center electron to the right dot for read out, at the position of green circle nr. 2. Afterwards we shuttle the left spin through the center dot to the right, and complete the three-spin read-out at the position of green circle nr. 1 in Fig. 4.1c. Details can be found in the Additional Material 4.6.2.

We test the operation of the Single-Spin CCD by preparing various combinations of the eight three-spin populations ↑↑↑ through ↓↓↓. To do so, we implement site-selective manipulation of each of the three spins exploiting the small difference in g-factors be-

tween the dots (Fig. 4.2i) combined with adiabatic inversion of the spins using electric dipole spin resonance (EDSR) [76]. This amounts to 'writing' the qubits of the Single-Spin CCD. After loading ↑↑↑, we create in this way the spin states ↓↑↑, ↑↓↑ or ↑↑↓ and subsequently vary the waiting time in the (1,1,1)-configuration. During that time, the populations evolve as the spins relax back to the ground state ↑↑↑.

Figs. 4.2a-h show the eight three-spin-probabilities as a function of the waiting time for the three initial state preparations. In addition, data are shown where random spins are injected in each of the three dots. We see that the data follow closely the expected behavior (see caption), shown as solid lines, indicating proper operation of the Single-Spin CCD.

This is the first demonstration of reading out multiple spins through the same reservoir. Read-out fidelities are on average 98.2 (±0.5)% for spin-up and 95.8 (±0.3)% for spin-down (see Additional Material 4.6.1).

4

4.3. STUDYING THE EFFECT OF SHUTTLING A SPIN ACROSS A LARGE DISTANCE

Next we examine the effect of shuttling electrons between dots on their spin projection. We anticipate three mechanisms that could in principle cause the spin-projection to change: (i) charge exchange with the reservoirs, (ii) spin-orbit (SO) interaction and (iii) hyperfine interaction with the nuclear spins of the quantum dot host material. Mechanism (i) is suppressed by applying precisely tuned pulse sequences and keeping the tunnel barriers of the reservoirs sufficiently closed. For the present gate voltage settings, we estimate this error to be $< 10^{-5}$ per hop along the array (Additional Material 4.6.3). The SO-interaction (ii) could affect the spin state, in a deterministic way, as it propagates through the array [77, 78]. The direction of movement with respect to the crystal axis determines the magnitude and direction of the SO-field. We expect the SO-interaction to be largest for motion along the $[1\bar{1}0]$ axis and minimal along the interdot axis [110] [30, 33], see (Fig. 4.1a). Furthermore, the small SO-field still originating from movement along this interdot axis will be *parallel* to the external field and therefore will not influence the spin projection. The hyperfine interaction (iii) can cause random flips arising from the instantaneous unknown difference in perpendicular (relative to B_{ext}) hyperfine field, $\delta B_{\perp}$, between neighbouring dots. This effect is suppressed by the large B_{ext} and estimated to be $< 1 \cdot 10^{-6}$ per shuttle event assuming $\delta B_{\perp}$ <7 mT (see Additional Material 4.6.3). In future experiments, mechanisms (ii) and (iii) can be further suppressed by transferring the spin from one dot to the other adiabatically compared to the Zeeman splitting.

To verify experimentally whether it is possible to shuttle electrons while preserving their spin projection, we simulate a very large array using the triple dot device. Using the charge states from Fig. 4.1c, we load one random electron in the (0,0,1)-state and shuttle it back and forth many times to (1,0,0) by passing through (0,1,0) as depicted schematically in Fig. 4.3b. Each run of going back and forth constitutes a total of four jumps from one dot to the other. In Fig. 4.3a, we vary both the total time spent in the CCD, t_{CCD}, and the number of interdot hops, n_{hops}, and read out the spin at the end. Up to 20, 70 and 350 hops, for a t_{CCD} of 2, 7 and 35 ms respectively, the time between jumps is longer than

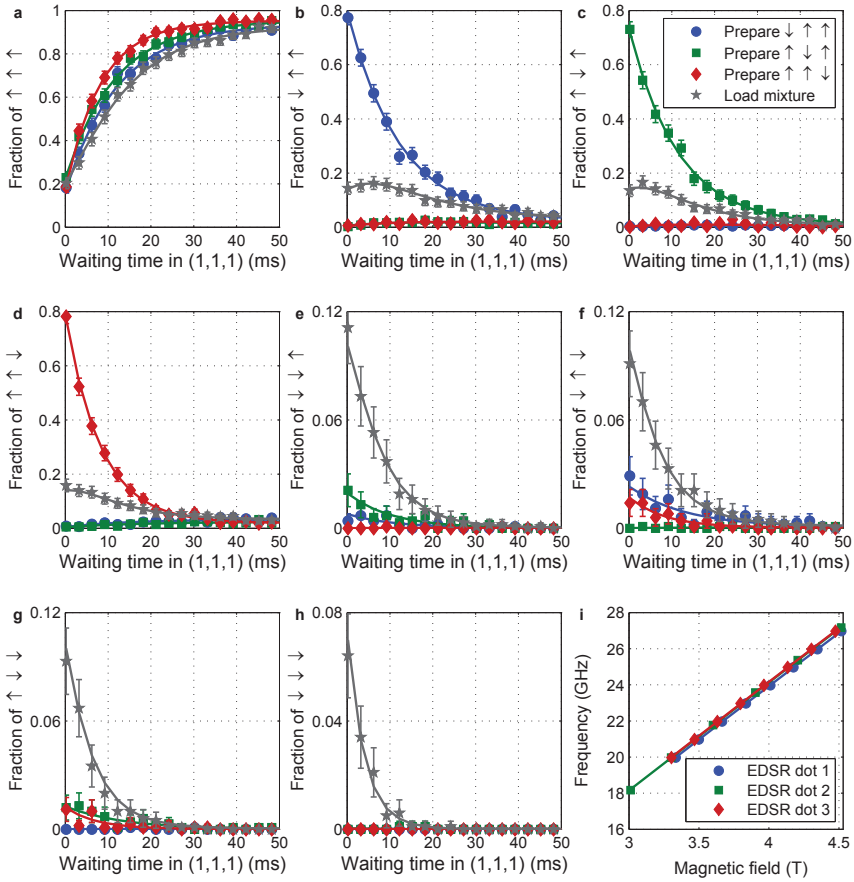

Figure 4.2: Writing and reading out the Single-Spin CCD. a-h, Measured three-spin populations as a function of waiting time between state preparation and read-out for four different state preparations. Starting from ↑↑↑ (> 95% initialization efficiency), states ↓↑↑ (blue) and ↑↑↓ (red) are prepared by EDSR in the (1,1,1)-regime. State ↑↓↑ (green) is created by applying EDSR in the (1,1,0)-regime, and then loading the third ↑-spin. For the fourth state preparation, the gate voltages are not ramped but pulsed across the relevant charge transitions, so that electrons with random spin will occupy the three dots. The contrast is limited to 0.8 mostly by imperfect adiabatic inversion and not by the read-out fidelities. Each datapoint is an average of 999 measurements (error bars two s.d.). Solid lines are products of the calculated single-spin probabilities based on the individual T_1 and initial spin-down probability of each dot. The fact that they overlap with the corresponding three-spin probabilities demonstrates that no (unintended) correlations were introduced between the spins. **i** Resonance frequency for each dot i as a function of the magnetic field. A fit of the form $f_{res} = \frac{g_1^i \mu_B B}{h} + \frac{g_3^i \mu_B B^3}{h}$ [52], with μ_B the Bohr magneton, h Planck's constant, gives $g_1^1 = -0.430 \pm 0.001$, $g_1^2 = -0.434 \pm 0.003$ and $g_1^3 = -0.434 \pm 0.002$. Despite similar g_1-factors in dot 2 and 3, time-variations of the local nuclear field still give rise to stable configurations where we can selectively address the two dots (see Additional Material 4.6.6, also for g_3^i)

the timescale on which the transverse component of the local nuclear field is randomized, which is the nuclear spin coherence time (~100 μs for the nuclear spins [26]). This

prevents coherent error accumulation as an electron repeatedly hops between the same dots. In that case, the effect of moving back and forth in the triple dot is the same as traversing successive dots in the same direction. For a larger number of hops and a fixed t_{CCD}, the hopping rate is increased and correlations may build up, although we have no indication of such an effect occurring in the present experiments. Fitting the data for each t_{CCD} to a linear curve gives an average change in the spin-down fraction ranging between $-1.7 \cdot 10^{-6}$ and $+8.3 \cdot 10^{-6}$ per hop (see Additional Material 4.6.3). We compare the measured spin state after shuttling many times, with the spin state measured after the electron has shuttled back and forth only once in exactly the same total amount of time. The latter effectively constitutes a weighted T_1 measurement over the three dots. The fact that the triangular symbols in Fig. 4.3a fall exactly on the weighted T_1 decay, indicates that there is no sign of spin flips other than through spontaneous relaxation, even after more than 500 hops. Taking an interdot distance of 160 nm, this corresponds to a total distance of about 80 μm.

4.4. SCALABILITY

An important question to address is the scalability of this approach. A single SD is not capable of recording charge stability diagrams, such as in Fig. 4.1c, for arrays much larger than 3 dots. However, by implementing dispersive gate sensors [79], one can first detect the required charge transitions to implement the shuttle scheme without requiring additional SDs. This approach is also well suited to 2D arrays. The data of Fig. 4.3a shows that in the current experiment, the bottleneck for improving the read-out fidelities is not the shuttling of the spins itself, but rather relaxation while waiting for read-out. More specifically, the limiting factors for this experiment are the times it takes to read out (~130 μs), empty a dot (~75 μs) and the time allowed for shuttling to the next dot (~10 μs). The black curves in Fig. 4.3c show the predicted spin-down fidelity as a function of the CCD-length, extrapolated based on the present numbers.

With a few technical improvements involving additional pulse lines, larger interdot tunnel couplings, and a somewhat lower magnetic field, tunneling and emptying can occur on a ns timescale, the read-out time can be halved and the T_1 can be doubled (Additional Material 4.6.4). This would give fidelities as shown in red in Fig. 4.3c. They allow one to read out 50 spins with > 83% fidelity.

The read-out time can be shortened more dramatically via the inclusion of Pauli spin blockade (PSB) in the read-out scheme. PSB allows one to distinguish whether two neighboring spins are parallel or anti-parallel [29, 48]. PSB read-out within 1 μs for a fidelity of 97% has been demonstrated in GaAs dots [80]. To implement this method in future experiments for read-out of a number of spins in as many dots, we suggest to add from the right an empty dot and a dot occupied by one electron, which will act as an ancillary reference spin. In this way one can quickly initialize the reference spin in the $\uparrow$-state on the rightmost dot using a so-called hot-spot where spins relax on a sub-μs timescale [81, 82]. Then we shuttle the first spin to be read out to the empty dot next to the reference spin and determine its spin using PSB. After discarding one of the spins, we reinitialize the remaining spin to be spin-up again and repeat the procedure until the whole chain of spins has been read out. This procedure significantly reduces the read-out time, leading to the blue curve in Fig. 4.3c, with fidelities above 88% for arrays of

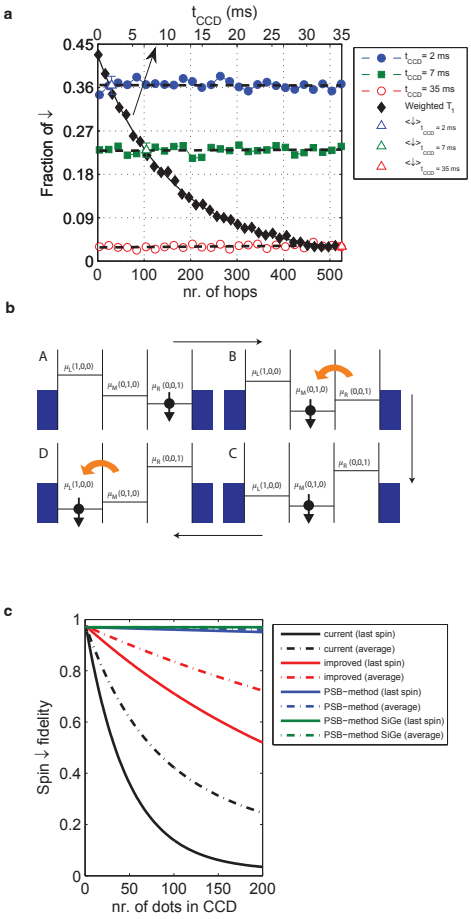

Figure 4.3: Preservation of the spin-projection during shuttling. a Circles and squares: measured spin-down probability after n_{hops} interdot hopping events for three values of the total time t_{CCD}. Black dashed lines are linear fits to the data. Diamonds: measured spin-down probability after shuttling back and forth just *once*, as a function of the total shuttling time, t_{CCD}. The decay time constant represents a weighted T_1 over all three dots ($T_{1,\text{weighted}} = 10.6 \pm 0.5$ ms). Triangles depict the average value of the shuttling data (circles and squares) for each value of t_{CCD} (error bars two s.d.). **b** Schematic representation of the tunneling of a spin back and forth inside the CCD array. Arrows depict the backwards trajectory from the right to the left dot. Reversing this pathway returns the spin to the right dot. There are two separate stages with the electron in the middle dot, to prevent charge exchange with the reservoirs (see Additional Material 4.6.2). **c** Estimated spin-down measurement fidelity as a function of the length of the Single-Spin CCD for the current settings, improved conditions as described in the main text and for the proposed PSB-scheme in GaAs and SiGe. Solid lines indicate the fidelity for the spin that is read out last, dashed lines the average fidelity for the whole array. The spin-up fidelity is independent of the CCD size.

1000 spins. Moving to a different host material such as Si or SiGe, T_1-times can reach seconds [82, 83], boosting fidelities further (green curve). For such large T_1-times, we estimate that the read-out fidelity of the last spin that is read out in an array of 1000 dots,

will decrease by only 0.07% compared to the read-out fidelity of the first spin.

The high fidelity with which the spin projection can be preserved upon shuttling between dots thus allows scaling the Single-Spin CCD concept to linear arrays of hundreds of dots. Two-dimensional arrays would be a natural next step. This would require either the use of weak spin-orbit materials like silicon, or accounting for (predictable) spin-orbit induced rotations along at least one direction. Finally, in materials with negligible hyperfine coupling, such as ^{28}Si enriched substrates [42], not only the spin projection but also the spin phase is expected to be preserved during shuttling. Such coherent single-spin shuttles allow qubits to be moved in the course of a quantum computation, an essential tool for powerful quantum computing architectures [64, 84].

4.5. METHODS

The experiment was performed on a GaAs/$Al_{0.25}Ga_{0.75}As$ heterostructure grown by molecular-beam epitaxy, with a 85-nm-deep 2DEG with an electron density of $2.0 \cdot 10^{11}$ cm^{-2} and mobility of $5.6 \cdot 10^6$ cm^{2}V^{-1}s^{-1} at 4 K. The metallic (Ti-Au) surface gates were fabricated using electron-beam lithography. The main function of gates *LS* and *RS* is to set the tunnel coupling with the left and right reservoir, respectively. D_1 and D_2 control the interdot tunnel coupling and P_1, P_2 and P_3 are used to set the electron number in each dot. The device was cooled inside an Oxford Kelvinox 400HA dilution refrigerator to a base temperature of 45 mK. To reduce charge noise the sample was cooled while applying a positive voltage on all gates (ranging between 0 and 350 mV) [85]. The device was tuned in the single-electron regime. The tunnel coupling at zero detuning between dot 1 and 2 was measured to be 0.8 GHz and 0.5 GHz between dot 2 and 3 using photon-assisted tunneling [86]. Gates P_1, P_2, P_3 and D_2 were connected to homebuilt bias-tees (RC = 470 ms), enabling application of d.c. voltage bias as well as high-frequency voltage excitation to these gates. RF reflectometry of the SD was performed using an LC circuit matching a carrier wave of frequency 110.35 MHz. The inductor is formed by a microfabricated NbTiN superconducting spiral inductor with an inductance of 3.0 μH. The power of the carrier wave arriving at the sample was estimated to be -99 dBm. The carrier signal is only unblanked during read-out. The reflected signal was amplified using a cryogenic Weinreb CITLF2 amplifier and subsequently demodulated using homebuilt electronics. Real time data acquisition was performed using a FPGA (DE0-Nano Terasic) programmed to detect tunnel events using a Schmidt trigger. The microwaves were generated using a HP83650A connected to P_2 via a homemade bias-tee at room temperature. Voltage pulses to the gates were applied using a Tektronix AWG5014 (0-100% risetime = 5 ns).

4.6. ADDITIONAL MATERIAL

4.6.1. CALCULATION OF THE FIDELITIES

In this part we discuss how we obtain the read-out fidelities from the data. We follow a similar approach as discussed in [53] but extend the method to more dots, and incorporate some minor differences to comply with the CCD-scheme. We denote single spin read-out fidelity as F_i^j where j denotes the dot in order of the read-out (1 is the rightmost dot for the current sample, 2 is the center dot, and 3 the leftmost dot), and $i \in \{\uparrow, \downarrow\}$.

ANALYTIC EXPRESSIONS FOR THE FIDELITY

We start with the fidelity for the spin-up state, $F_\uparrow^j = 1 - \alpha^j$, where α^j is the probability that a step is detected in the SD signal although there was a spin-up electron in the quantum dot. This can occur if the SD signal exceeds the threshold even though the electron stayed in the dot (referred to as a signal processing error), or if the electron tunnels out of the dot due to thermal or electric field fluctuations. We can determine α^j directly for each quantum dot by initializing in the spin-up state and successively reading it out. In this case, the fraction of the cases where a spin-up electron is declared spin-down directly gives α^j. This method assumes perfect initialization and thus gives an upper bound on α^j. α^j might be slightly different for the different dots due to differences in the tunnel barrier with the right reservoir for each charge state, the length of the read-out stages, the thresholds and the signal heights. Except for these slight differences, $F_\uparrow^j$ is independent of the size of the array. There are two effects that may influence a spin-up state during the read-out sequence: (1) back-action from the SD or (2) thermal excitation. In the CCD scheme, each electron will experience a similar amount of back-action from the SD (an electron far away in an array will not yet experience back-action). Thermal excitation is negligible for the current energy scales: $E_z \approx 90\ \mu$eV and $k_B T \approx 6.5\ \mu$eV. In thermal equilibrium, an initially perfect spin-up electron will have a probability of $\sim 10^{-6}$ to be in the spin-down state (Boltzmann distribution). This is a negligible correction for our current spin-up fidelities. These fidelities are likely limited by thermal broadening and/or electrical noise.

Next, we estimate the fidelity for the spin-down state based on the relaxation time T_1^j, the duration of the read-out stage, T_R^j, the electron tunneling rates (denoted by $\Gamma_\sigma^{i,j}$, where $\sigma \in \{\text{in}, \text{out}\}$ represents tunneling in or out of the quantum dot) and an analysis of the measurement bandwidth.

The spin-down fidelity for the first dot, $j = 1$, is $F_\downarrow^1 = \Xi^1 + \Lambda^1$. Ξ^j describes the probability that a spin-down electron tunnels out during the read-out stage before it relaxes. Λ^j describes the probability that a spin-down electron relaxes during the read-out stage, but still tunnels out because of the nonzero $\Gamma_{out}^{\uparrow,j}$.

First we assume infinite measurement bandwidth. In that case Ξ^j can be defined as

follows:

$$\Xi^j = \int_0^{T_R^j} \Gamma_{out}^{\downarrow,j} P_\downarrow(t)\,dt \tag{4.1}$$

where $\Gamma_{out}^{\downarrow,j} P_\downarrow(t)$ is the probability density function for a spin-down electron to tunnel out at time t. The probability for the electron to be spin-down, $P_\downarrow(t)$, or spin-up, $P_\uparrow(t)$, at time t follows from rate equations: (1) $\frac{dP_\uparrow}{dt} = -\Gamma_{out}^{\uparrow} P_\uparrow + (1/T_1)\,P_\downarrow$ and (2) $\frac{dP_\downarrow}{dt} = -(\Gamma_{out}^{\downarrow} + 1/T_1)P_\downarrow$. These equations describe the probabilities *before* the read-out event occurred (after which a spin-up electron will fill the dot with rate $\Gamma_{in}^{\uparrow,j}$). The initial conditions are $P_\uparrow(t=0) = 0$ and $P_\downarrow(t=0) = 1$. From this we find

$P_\uparrow(t) = \frac{1}{1+T_1(\Gamma_{out}^{\downarrow} - \Gamma_{out}^{\uparrow})}(e^{-\Gamma_{out}^{\uparrow} t} - e^{-(\frac{1}{T_1}+\Gamma_{out}^{\downarrow})t})$ and $P_\downarrow(t) = e^{-(\frac{1}{T_1}+\Gamma_{out}^{\downarrow})t}$.

4

Next we add the measurement bandwidth to the calculation. A tunnel event leads to a pulse in the SD signal. The duration of this pulse is determined by $\Gamma_{in}^{\uparrow,j}$. A pulse with duration τ will be detected with probability $B^j(\tau)$, which depends on the measurement bandwidth (see below). Therefore the probability that a pulse which is caused by an electron that tunnels out is detected is:

$$\Xi^j = \int_0^{T_R^j} \Gamma_{out}^{\downarrow,j} P_\downarrow(t)\,dt \int_0^{\infty} \Gamma_{in}^{\uparrow,j} e^{-\Gamma_{in}^{\uparrow,j}\tau} B^j(\tau)\,d\tau \tag{4.2}$$

We can extend the limit of the second integral to ∞ because we also count events where an electron did not yet tunnel back during the read-out time as spin-down. Eq. (4.2) assumes that we detect every electron leaving the dot with a 100% probability. This assumption is not correct for tunnel events occurring very close to the end of the read-out stage. Based on the measured bandwidth (see below) we can assume that every electron leaving the dot at least 0.7 μs before the end of the read-out stage will be detected. This gives the following lower bound for Ξ^j:

$$\Xi^j = \int_0^{T_R^j - 0.7\mu s} \Gamma_{out}^{\downarrow,j} P_\downarrow(t)\,dt \int_0^{\infty} \Gamma_{in}^{\uparrow,j} e^{-\Gamma_{in}^{\uparrow,j}\tau} B^j(\tau)\,d\tau \tag{4.3}$$

At the end of each read-out we always empty the right dot before going to the next read-out position so subsequent read-out stages always have the same charge configuration.

The probability that a spin-down electron relaxes during the read-out stage before it could tunnel out but that nevertheless a step is detected due to the spin-up electron tunneling out is given by

$$\Lambda^j = \int_0^{T_R^j - 0.7\mu s} \Gamma_{out}^{\uparrow,j} P_\uparrow(t)\,dt \int_0^{\infty} \Gamma_{in}^{\uparrow,j} e^{-\Gamma_{in}^{\uparrow,j}\tau} B^j(\tau)\,d\tau \tag{4.4}$$

where $\Gamma_{out}^{\uparrow,j} P_\uparrow(t)$ is the probability density function that the initial spin-down electron has relaxed to spin-up before tunneling out (recall we consider here the case that $P_\uparrow(t=0)=0$).

The spin-down fidelity for dots with $j>1$ are additionally affected by relaxation during the previous read-out stages including the emptying of all dots $< j$, and the time it takes to shuttle from their position in the array to the read-out position, which adds a shuttling time. The total waiting time before the j^{th} dot is read-out is denoted by T_{wait}^j. This relaxation occurs with probability $\eta^j = \int_0^{T_{wait}^j} \frac{1}{T_1^j} e^{-t/T_1^j} dt$. Therefore the spin down fidelity for the quantum dots with $j>1$ is

$$F_\downarrow^j = (\Xi^j + \Lambda^j)(1-\eta^j) + \eta^j \alpha^j \tag{4.5}$$

The last term accounts for the case that the spin down electron of the j^{th} dot relaxes to spin up during T_{wait}^j but in the end is still detected as spin down. For the experiment the following values were used: $T_R^1 = T_R^2$ =130 μs, T_R^3 =300 μs, T_{wait}^2 = 222.15 μs and T_{wait}^3 = 514.3 μs. These values were chosen to optimize the sum of the three spin-down fidelities, whilst keeping the spin-up fidelity high.

Note on the choice of T_1^j: as we are transferring some of the spin states throughout the array, they will also experience different T_1's depending on their location. In the current scheme each spin is waiting most of the time in its starting dot, so for the calculation of η^j we take T_1^j. During the read-out itself, so for the calculation of Ξ^j and Λ^j we always use $T_1^j = T_1^1$. Fig. 4.4 shows the three measured T_1^j.

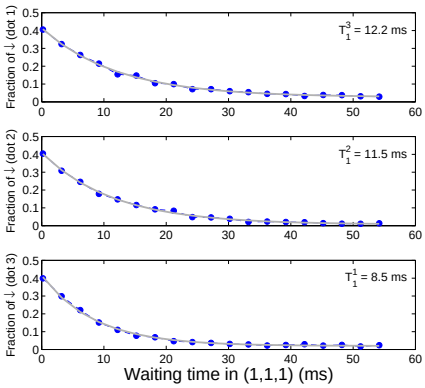

Figure 4.4: Single dot relaxation as a function of waiting time in (1,1,1). Each datapoint is an average of 2000 measurements. Grey lines are a fit to $p^j \cdot e^{-t/T_1^j} + \alpha^j$.

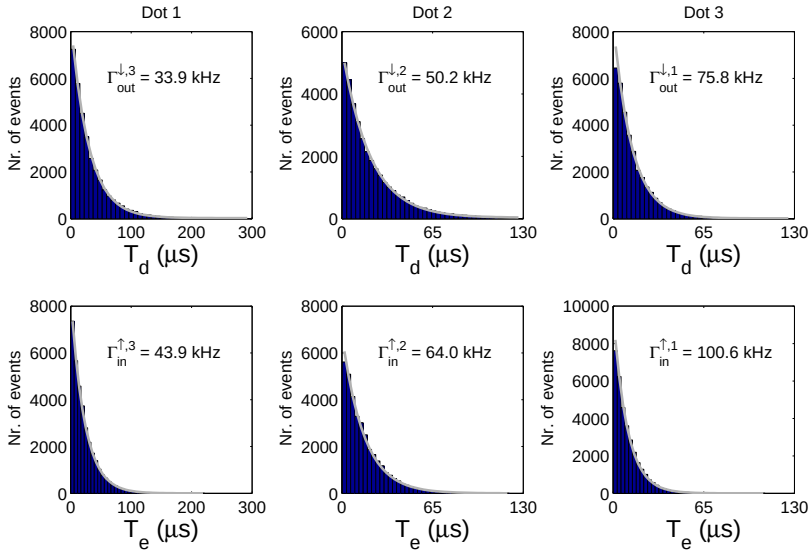

Figure 4.5: Top row: histograms showing the distribution of the time T_d it takes a spin-down electron to tunnel out at the read-out position of each respective dot for the measurement shown in Fig. 4.4. The line is an exponential fit from which we determine the decay rate given by $\Gamma^{\downarrow,j}_{out} + \frac{1}{T_1^j}$. Bottom row: histograms showing the distribution of the time T_e it takes a spin-up electron to tunnel back into the empty dot. The grey line is an exponential fit from which we can extract the decay rate given by $\Gamma^{\uparrow,j}_{in}$.

DETERMINATION OF THE TUNNEL RATES

For calculating the spin-down read-out fidelities, various tunneling rates need to be known. We can obtain $\Gamma^{\downarrow,j}_{out}$ and $\Gamma^{\uparrow,j}_{in}$ from the measurements of the histograms of the time it takes a spin-down electron to tunnel out (T_d^j) and of the time it takes a spin-up electron to tunnel back into the quantum dot (T_e^j), see Fig. 4.5. We estimate $\Gamma^{\uparrow,j}_{out}$ from the measured value of α^j, which characterizes the spin up fidelities and can be expressed as

$$\alpha^j = \int_0^{T_R^j - 0.7\mu s} \Gamma^{\uparrow,j}_{out} e^{-\Gamma^{\uparrow,j}_{out} t} dt \int_0^{\infty} \Gamma^{\uparrow,j}_{in} e^{-\Gamma^{\uparrow,j}_{in} \tau} B^j(\tau) d\tau + \epsilon^j \tag{4.6}$$

Here ϵ^j is the signal processing error which is found to ≤ 0.1 % (to be discussed in the section on the characterization of the measurement bandwidth).

CHARACTERIZATION OF THE MEASUREMENT BANDWIDTH

The signature of a spin-down electron tunneling out of the dot followed by a spin-up electron tunneling back into the dot is a pulse in the SD signal. Due to the finite measurement bandwidth, we can only detect pulses of sufficient duration and we therefore miss a fraction of the actual tunnel events. We characterize the measurement bandwidth by simulating such electron tunneling events by applying a rectangular pulse to P_3 with

duration τ and amplitude A. The triple dot is tuned deep into Coulomb blockade such that the applied pulse cannot result in a charge transition of any of the quantum dots. Due to the capacitive coupling of P_3 to the SD, a rectangular pulse will be created in the SD signal. The amplitude A is chosen such that the height of the pulse in the SD signal equals the signal from electron tunneling events for each respective read-out stage. The pulse duration is varied from 0.0 to 1.0 μs. Fig. 4.6 shows the probability of detecting an event of duration τ, $B^j(\tau)$, as a function of the pulse duration for each of the three read-out channels. Using the formulas derived in *Analytic expression for the fidelity* we calculate the fidelities numerically by using the measured probabilities $B^j(\tau)$; the result is shown in Table 4.1. The fraction of the detected events at $\tau = 0$ s gives the signal processing error, ϵ^j, which corresponds to the fraction of traces in which an event is detected in the SD signal due to noise in the SD-signal during the read-out stage.

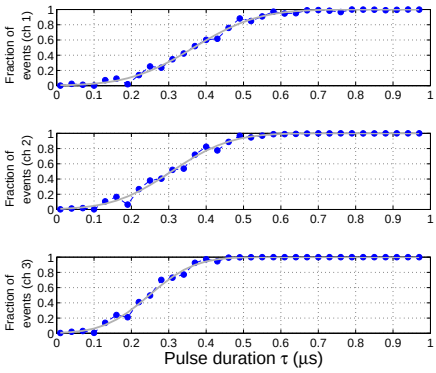

Figure 4.6: The probability of detecting a pulse with duration τ for each of the three read-out channels ($B^j(\tau)$). Every read-out stage is monitored by a separate input channel of the FPGA. The output of the demodulation box is low-pass filtered at 1 MHz. The sensitivity of the SD to the three different read-out stages is slightly different as they occur at different detunings of the plunger gates. Each datapoint is an average of 1000 measurements.

dot nr.	T_1 (ms) (worst,best)	Spin-down fidelity (%) (worst,best)	Spin-up fidelity (%) (worst,best)	Orbital splitting (meV)
1	12.2 (11.4, 13.1)	94.1 (93.8, 94.5)	97.4 (96.7, 98.0)	2.0
2	11.5 (10.9, 12.2)	95.8 (95.6, 96.1)	99.3 (98.8, 99.9)	1.8
3	8.5 (8.0, 9.0)	97.4 (97.3, 97.5)	98.0 (97.6, 98.4)	1.0

Table 4.1: Read-out fidelities per dot. Values in brackets show the error margins based on the fits. For completeness the orbital splitting in each of the three dots was also measured using pulsed spectroscopy [87].

4.6.2. DETAILED INFORMATION OF THE APPLIED PULSE SEQUENCE

In this section we give detailed information on the applied pulse sequences. Fig. 4.7 shows the same charge stability diagram as Fig. 4.1cd from the main text with additional labeling. For the CCD-protocol two operating points for gate M were used: M = -42 and M = -56. These two points combined give access to all the required charge states and are not unique. There is a window of several mV for both M-points that would give access to the same set of charge states. For the current settings each charge state has a well-defined and not too small region in the L,R-space. Table 4.2 gives an explanation including the details of the relevant pulse stages. Two general comments:
(1) To correct for slow variations in the dot levels as a function of time (hours timescale), we always calibrate the three read-out stages before each longer measurement such as a complete T_1 decay (~20.000 datapoints taken after one calibration run, which takes about half an hour).
(2) The wait time after each interdot shuttle event is set long enough to ensure full transfer of the electron. This is determined by the interdot tunnel rates at those specific detunings, which we measured to be >1 MHz (measurement limited by measurement bandwidth). Future work could incorporate adiabatic transfer of the electron from one dot to the other which can ensure faster elastic shuttling compared to the inelastic shuttling used in the current experiment.

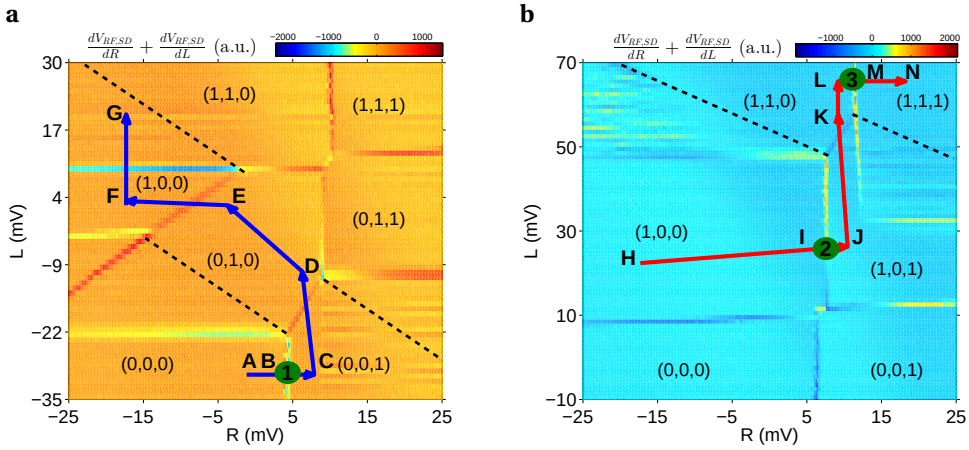

Figure 4.7: Charge stability diagram for **a** M = -42 and **b** M = -56 from Fig. 4.1cd from the main text with added details for the pulse sequence.

Stage(s)	Purpose and details
A	Emptying stage (lasting 1 ms) during which all dots are emptied.
B → C	Loading an electron from the right reservoir into the right dot. We ramp from B to C in 600 μs to load a ↑-electron, or pulse from B to C to load an electron with random spin.
C → D	Shuttle electron from the right to the middle dot. Waiting time at D is 10 μs.
D → E	Preparing to shuttle to the next dot. Waiting time at E is 1 μs.
E → F	Shuttle electron from the middle to the left dot. Waiting time at F is 10 μs.
F → G	Preparing to pulse into the other M-plane. Waiting time at G is 1 μs.
G → H	Pulse into the other M-plane. Waiting time at H is 10 μs.
H → I	Preparing to load a new electron into the right dot. Waiting time at I is 1 μs.
I → J	Loading an electron from the right reservoir into the right dot. We ramp from I to J in 400 μs to load a ↑-electron, or pulse from I to J to load an electron with random spin.
J → K	Shuttle electron from the right to the middle dot. Waiting time at K is 10 μs.
K → L	Preparing to load a new electron into the right dot. Waiting time at L is 1 μs.
L → M	Loading an electron from the right reservoir into the right dot. We ramp from L to M in 400 μs to load a ↑-electron, or pulse from L to M to load an electron with random spin.
M → N	Optional stage to perform EDSR deeper into (1,1,1) to prevent photon-assisted tunneling with the reservoirs during the applied FM-burst.
Read-out stage 3	Gate voltage pulses larger than ~2 mV produce a spike in the RF-read-out signal. To prevent false events, we therefore first pulse to a position close to the read-out stage (2 mV more positive in R) and wait for 2 μs. Only then, the RF-signal is unblanked and next we pulse into the read-out configuration for 130 μs.
L	Empty the right dot for 70 μs.
L → K → J	Shuttle the center electron to the right dot. Waiting time at J is 10 μs.
Read-out stage 2	Similar as Read-out stage 3.
I	Empty the right dot for 100 μs.
I → C	Path of I to C through all intermediate points with similar times as for the loading sequence.
Read-out stage 1	Similar as Read-out stage 3, except we now stay in the read-out configuration for 300 μs.
Compensation stage	At the end of the pulse sequence we add a compensation stage of 10-45 ms that ensures that the total DC-component of the pulse is zero. This prevents unwanted offsets of the dot levels due to the bias tees.

Table 4.2: Detailed explanation of the applied pulse sequence as described by Fig. 4.7. Unless noted otherwise, we always apply pulses from one point to the other. The total duration of this sequence varies between 3.3 and 54 ms, not including the compensation stage at the end.

4.6.3. ESTIMATION OF THE ERROR RATE DURING SHUTTLING

In the main text we give estimates for the error rate during shuttling caused by (A) charge exchange with the reservoir and (B) random spin flips caused by the hyperfine interaction. In this subsection we will derive the models used to quantify these errors.

CHARGE EXCHANGE WITH THE RESERVOIR

Fig. 4.8 shows the pulse scheme of the multiple shuttling experiment in more detail. The probability that pulsing from A to B will be successful (i.e. the electron is fully transferred to B) can be calculated as follows:

$$P_{A\to B}(t_{shuttle}) = \int_0^{t_{shuttle}} \Gamma_{A\to B} e^{-\Gamma_{A\to B} t} dt \tag{4.7}$$

where $t_{shuttle}$ is the time the electron waits in B before going to C, and $\Gamma_{A\to B}$ is the interdot tunnel rate between the middle and right dot at that specific detuning. In this experiment the waiting time at each point A, B, C, D is equal to $t_{shuttle} = \frac{t_{CCD}}{1.5 \cdot n_{hops}}$.

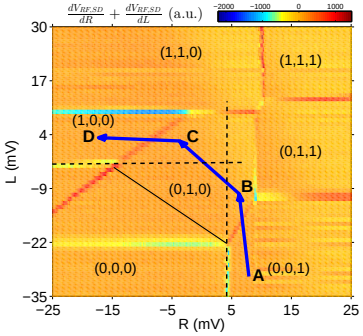

Figure 4.8: Pulse scheme for the multiple shuttling experiment. We first load a random spin at position A from the right reservoir. Next we go back and forth to A by applying the following pulse sequence: A→B→C→D→C→B→A. Each run of going back and forth corresponds to four interdot tunnel events. The black dashed lines are extensions of the dot-reservoir charge transition lines.

In the case that the electron was not successfully transferred to (0,1,0) at B, an error might occur when we continue pulsing to C. Pulsing from B to C crosses the extension of the right dot-reservoir charging line (dashed vertical line in Fig. 4.8). This implies that the following two processes can occur to the electron that is still in the right dot whilst the detuning has already been pulsed to C: (1) the electron will shuttle from the right to the middle dot with rate $\Gamma_{A\to C}$, (2) the electron will tunnel out to the right reservoir with rate $\Gamma_{reservoir,R}$, and a new electron is eventually loaded, but its spin will not be correlated with that of the initial electron, introducing an error. The probability that an error occurs going from B to C can therefore be expressed as:

$$P_{error,B\to C} = \frac{\Gamma_{reservoir,R}}{\Gamma_{A\to C} + \Gamma_{reservoir,R}} \tag{4.8}$$

Leading to:

$$P_{error,A\to C} = (1 - P_{A\to B}(t_{shuttle})) \cdot P_{error,B\to C} \tag{4.9}$$

In the following, we will neglect the possibility that none of the above two processes occurred at C. We will also neglect the possibility of an unsuccessful tunnel event from $C \rightarrow D$. This would lead to a second-order correction to the error in the reversed pathway $D \rightarrow B$. The reversed pathway can then be expressed in a similar way as eq. (4.9). We measured that $\Gamma_{reservoir,R} \approx 20$ kHz, $\Gamma_{reservoir,L} \approx 10$ kHz and $\Gamma_{A\rightarrow B}, \Gamma_{D\rightarrow C}, \Gamma_{D\rightarrow B} > \Gamma_{A\rightarrow C} > 1$ MHz (lower bound, limited by the measurement bandwidth). The error should therefore be dominated by the path going from A to C. To get an upper bound for the error, we will assume from now on that $P_{error} = P_{error,A\rightarrow C} = P_{error,D\rightarrow B}$ and $\Gamma_{A\rightarrow B} = \Gamma_{A\rightarrow C} = \Gamma_{D\rightarrow B} = \Gamma_{D\rightarrow C}$.

To calculate the measurement outcome at the end of the shuttling sequence, we only have to keep track of the last error in each measurement run. If an electron is exchanged for example twice during a run, we will eventually only measure the spin state of the last electron that entered.
Depending on when the last error occurred, we load a spin-down electron with probability $P_{load,\downarrow}$. Its spin state will decay with $T_1 = T_{1,weighted}$. Please recall that P_{error} is equal to the error per *two* hops as we neglect errors in the processes $C \rightarrow D$ and $B \rightarrow A$.

$$P_{\downarrow}(n_{hops}, t_{CCD}) = P_{load,\downarrow}\left((1-P_{error})^{n_{hops}/2} e^{-t_{CCD}/T_{1,weighted}}\right) + P_{load,\downarrow}\left(\sum_{k=1}^{k=n_{hops}/2} P_{error}(1-P_{error})^{k-1} e^{-(t_{CCD}\cdot\frac{(k-1)}{n_{hops}/2})/(T_{1,weighted})}\right) \tag{4.10}$$

The first term describes the process of no error occurring. The second term adds up all the possible errors starting from the last error happening in the final stage, $k = 1$, till the first stage, $k = n_{hops}/2$.

It was only possible to measure a lower bound for $\Gamma_{A\rightarrow C} > 1$ MHz. Fig. 4.9 plots the outcome of eq. (4.10) for the same values of t_{CCD} as in the main text, Fig. 4.3a, for two different values of $\Gamma_{A\rightarrow C} = \Gamma_{D\rightarrow B}$: 1 MHz and 2 MHz. Each curve is fitted linearly to extract a change in the spin-down fraction per hop. This linear approximation is only valid for our current regime of small error rates. For large error rates the spin-down fraction will increase non-linearly and eventually form a plateau at the value of $P_{load,\downarrow}$.
The fitted change in the spin-down fraction per hop is $< 10^{-8}$ for $t_{CCD} \geq 7$ ms, so we only quote the values for $t_{CCD} = 2$ ms: $18 \cdot 10^{-6}$ ($\Gamma_{A\rightarrow C} = 1$ MHz) and $0.5 \cdot 10^{-6}$ ($\Gamma_{A\rightarrow C} = 2$ MHz). The experimentally measured values are given in Table 4.3.

t_{CCD} (ms)	change in spin-down fraction per hop
2	-1.7 (-25,21) $\cdot 10^{-6}$
7	4.6 (-15,24) $\cdot 10^{-6}$
35	8.3 (-0.97,18) $\cdot 10^{-6}$

Table 4.3: The measured change in spin-down fraction per hop measured from the data in Fig. 4.3a of the main text. Values in between brackets indicate the 95% confidence interval of the linear fit.

Based on this simulation we can conclude that charge exchange with the reservoir is a negligible effect for $t_{CCD} = 7$ and 35 ms and the probability to successfully shuttle

from A to B or D to C will approach 1. For the case of t_{CCD} = 2 ms, the slope extracted from the simulation is within the error bars of the experimentally measured value. It is not clear whether charge exchange with the reservoir is already the limiting mechanism here. Finally, we note that when shuttling electrons along longer arrays, charge exchange with the reservoirs will be negligible, if most dots in the array are in fact not coupled to reservoirs.

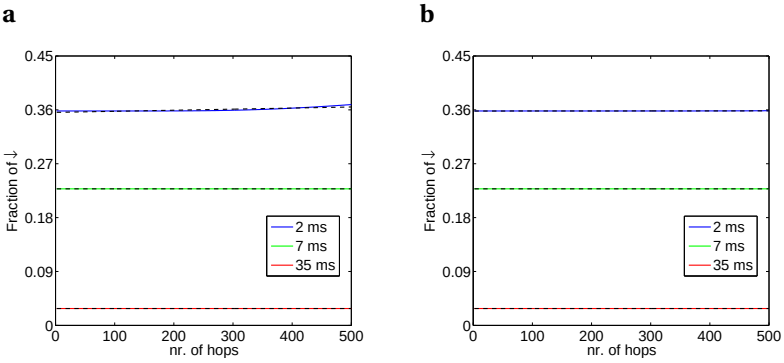

Figure 4.9: Outcome of eq. (4.10) for the same values of t_{CCD} as the main text Fig. 4.3a for two different values of $\Gamma_{A\to C} = \Gamma_{D\to B}$: **a** 1 MHz and **b** 2 MHz. In both cases $\Gamma_{reservoir,R}$ = 20 kHz. Each curve is linearly fitted (dashed lines) to extract a change in the spin-down fraction per hop.

RANDOM SPIN FLIPS CAUSED BY THE HYPERFINE INTERACTION

To estimate the error rate caused by the hyperfine interaction we describe what happens to a spin that starts in the spin-up state in the first dot. A similar reasoning applies to a spin that starts as spin-down.

The spin-up state in the first dot can be described as a Bloch vector with length 1 and an angle $\theta_1 = \arctan(B_{N1,\perp}/B_{ext})$ w.r.t to B_{ext} where $B_{N1,\perp} = \sqrt{\left\langle \left(B_N^{x,y}\right)^2 \right\rangle} \approx 5$ mT is the magnitude of the local nuclear field orthogonal to B_{ext} inside dot 1. In the next dot, the spin will experience a different nuclear field: $B_{N2,\perp}$. The Bloch vector will now start rotating along a new axis given by $\theta_2 = \arctan(B_{N2,\perp}/B_{ext})$ w.r.t to B_{ext}. In the current experiment, the timing jitter on the tunnel events is at least 1 ns (due to the finite interdot tunnel rate). This jitter is large compared to the spin precession rate of 50 ps and leads to the loss of phase information after each hop. The Bloch vector can therefore be modelled as a vector with length $\cos(\theta_2 - \theta_1)$ pointing at an angle of θ_2 w.r.t B_{ext}. For small angles $\Delta\theta = \theta_2 - \theta_1 \approx \arctan((B_{N2,\perp} - B_{N1,\perp})/B_{ext}) = \arctan((\sqrt{2}B_{N1,\perp})/B_{ext})$. Repeating this n_{hops} times gives a final Bloch vector with length $(\cos(\Delta\theta))^{n_{hops}}$ at an angle θ_{finaldot}. The probability to be in the ground state of the last dot, and thus to be measured as spin-up, is then given by:

$$P_\uparrow = 0.5 + 0.5 \cdot (\cos(\Delta\theta))^{n_{hops}} \approx 1.0 - \frac{(1-\cos(\Delta\theta)) \cdot n_{hops}}{2} \tag{4.11}$$

In the last step of the equation we apply the approximation that $\cos(\Delta\theta) \approx 1$. The error per hop is then estimated by $\frac{(1-\cos(\Delta\theta))}{2} = 1 \cdot 10^{-6}$.

4.6.4. SUGGESTED IMPROVEMENTS TO INCREASE THE READ-OUT FIDELITIES

This section covers the details of the described improvements for the current experiment as mentioned in the Discussion of the main text.

IMPROVING THE CURRENT GAAS EXPERIMENT

We suggest the following to improve the current GaAs experiment (without yet including PSB). To decrease the read-out time we can add a pulsed line to the SD. This allows us to always set the SD to the most sensitive point for each separate read-out position, which should easily improve the measurement bandwidth by a factor of two and thereby reduce the required read-out time by a factor of two. To decrease the emptying-time we propose to add a pulsed line to *RS*, so the tunnel rate between right dot and reservoir can be switched between fast (for emptying) and moderate (for read-out). Combined with larger interdot tunnel couplings both the emptying and the shuttling can take place on the ns timescale. Much faster shuttling would violate the adiabaticity condition, i.e. excitations to higher orbital states would occur [64]. The final improvement involves lowering the magnetic field to 3.0 T (which would require to slightly reduce the electron temperature in order to maintain high read-out fidelities), which already doubles the T_1 time [26]. These improvements combined give the red curve of Fig. 4.3c of the main text. The exact parameters used are: spin-down fidelity of the first dot being read-out is 97,4%, T_1 = 20 ms, read-out time = 65 μs, emptying time of the rightmost dot = 2 ns and shuttling time = 2 ns.

INCLUDING PSB TO THE EXPERIMENT

GaAs-experiment: by including PSB in the measurement scheme we can reduce the read-out time from 65 μs to 1 μs for a read-out fidelity of 97%. We assume a initialization time of 1 μs by using the hot spot. The values for the other parameters are the same as for the red curve. This gives the blue curve of Fig. 4.3c of the main text. By moving to Si/SiGe we change the T_1 to 3 seconds leading to the green curve.

4.6.5. VIRTUAL GATES *L*, *M* AND *R* AND THE USAGE OF 'FAST HONEYCOMBS'

'Virtual gates'

To control the electron number inside each dot we change the voltages on gates P_1, P_2 and P_3. In practice each gate couples capacitively to all three dots. Changing for example P_1 which couples mostly to dot 1, will therefore also influence dot 2 and 3. To make selective control of each dot easier it is convenient to correct for this cross-capacitive coupling. This can be done by measuring the cross-capacitance matrix for the three gates recording the influence of each gate on every dot. Inverting this matrix allows you to create honeycomb diagrams with vertical and horizontal charge transitions in a so-called 'virtual gate'-space. In such a 'virtual gate'-space, the real gates P_1, P_2 and P_3 have been replaced by linear combinations of the three gates which allow the user to change the chemical potential in one dot, without changing it in the neighboring dot.

For this experiment the exact relation between P_1, P_2 and P_3 and the 'virtual gates' *L*, *M* and *R* used is given by:

$$\begin{pmatrix} L \\ M \\ R \end{pmatrix} = \begin{pmatrix} 1.56 & 0.0 & 0.40 \\ 0.0 & 1.56 & 0.0 \\ 0.20 & 0.51 & 1.05 \end{pmatrix} \begin{pmatrix} P_1 - P_{1,\text{offset}} \\ P_2 - P_{2,\text{offset}} \\ P_3 - P_{3,\text{offset}} \end{pmatrix}$$

With $P_{1,\text{offset}} = 23.99$ mV, $P_{2,\text{offset}} = 61.01$ mV, $P_{3,\text{offset}} = -111.6$ mV. This set of virtual gates did not perfectly correct for cross-capacitances, as the capacitances turn out to slightly vary themselves with the gate voltages. Working with virtual gates does however give one large freedom to take slices at any angle through the 3D honeycomb diagram that satisfy the requirements for the experiment.

'Fast honeycombs'

All charge stability diagrams shown in this work have been taken in so-called 'fast honeycomb' mode. Using the bias-tees connected to P_1, P_2 and P_3 it is possible to step one of them 'slowly' using a DAC and apply a triangular ramp on the other using the AWG. This significantly speeds up the measurements compared to stepping both gates using DAC's. We have always plotted the reverse sweep, i.e. the voltage on horizontal axis is swept from positive to negative (with a rate of 100 mV/44 ms). The fading of the middle dot charging line can be explained through the small interdot tunnel couplings. Fig. 4.10 depicts the same stability diagram as in Fig. 4.1 of the main text over a larger scan range.

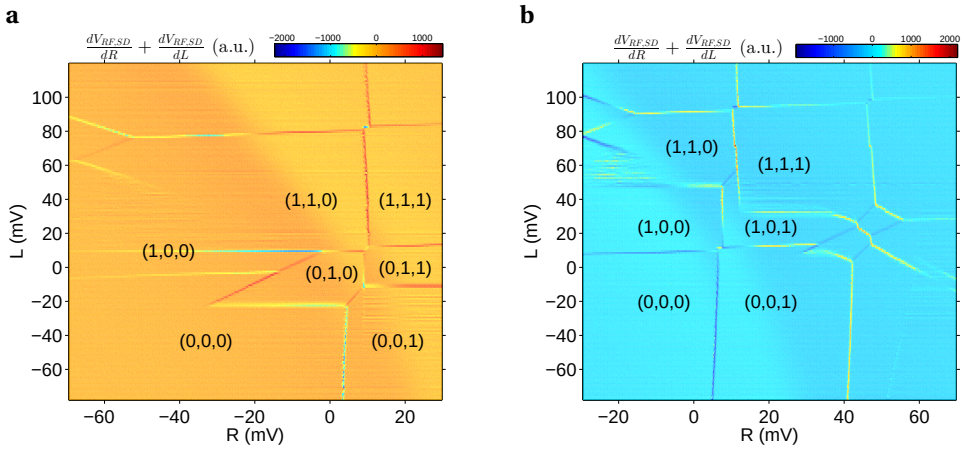

Figure 4.10: Charge stability diagram for **a** M = -42 and **b** M = -56 shown over a larger range than in Fig. 4.1cd.

4.6.6. EDSR SPECTRA OF EACH DOT AND SPIN-DOWN INITIALIZATION EFFICIENCIES

Fig. 4.11 shows EDSR spectra for each dot measured in a similar way as in [52]. Despite similar g_1-factors, time-variations of the local nuclear field still give rise to stable configurations where we can selectively address dot 2 and 3 in the (1,1,1)-regime. To perform such a measurement, the read-out sequence is started and then we manually tune the EDSR-frequency until we find a value that only addresses dot 3. We managed to find configurations stable for more than 30 minutes. We suspect there is some interplay between the electron and nuclear spins that leads to these stable points [39]. This requires further study that is outside the scope of this paper. For completeness Table 4.4 gives an overview of the measured g-factors in each dot.

Although we use adiabatic passage to create the spin-down states, the initialization efficiency is still limited on average to 76%. We attribute this non-perfect efficiency to two causes: (1) to achieve selective addressing of dot 2 and 3 (which are closest in g-factor) we on purpose slightly detune from the ideal spin-orbit mediated EDSR (SO-EDSR) resonance condition to prevent cross-talk. (2) At 3.51 T, the three hyperfine-mediated-EDSR resonance conditions are detuned by only 26 MHz to 46 MHz from the SO-EDSR condition [76]. Each resonance frequency by itself is capable of (partially) inverting the spin during a frequency chirp. The used FM-depth of 60 MHz could thus sometimes span several resonances that partially cancel each other.

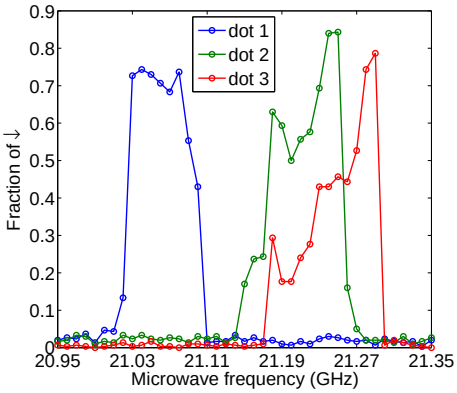

Figure 4.11: EDSR spectra for each dot. We load ↑↑↑ inside (1,1,1) and apply a frequency-modulated(FM)-burst to adiabatically invert the spin(s). Afterwards we read out the spin state. Each datapoint is an average of 300 measurements. FM-depth = 60 MHz, burst time = 500 μs. Power applied to the gate is -29 dBm (excluding corrections for coax attenuation). The frequency is stepped from 21.35 GHz to 20.95 GHz

dot nr.	g_1	g_3
1	-0.4304 (-0.4292, -0.4316)	0.0001853 (0.0001109, 0.0002596)
2	-0.4337 (-0.4307, -0.4368)	0.0001695 (-0.0000205, 0.0003595)
3	-0.4344 (-0.4328, -0.4361)	0.0001762 (0.0000711, 0.0002814)

Table 4.4: Measured g-factor in each dot based on fits of the form $f_{res} = \frac{g_1^i \mu_B B}{h} + \frac{g_3^i \mu_B B^3}{h}$ to the data of Fig. 4.2i) of the main text. Values in brackets indicate the 95% confidence interval.

4.6.7. T_1 MEASUREMENTS PERFORMED FOR DIFFERENT CHARGE STATES IN THE HONEYCOMBS

To further verify the proper operation of the single spin CCD we have also performed T_1 measurements where we do not vary the waiting time in (1,1,1) as shown in Fig. 4.2 of the main text, but instead change the waiting time in different charge states. In Fig. 4.12 we measure the T_1 decay of the spins by first loading three random spins in (1,1,1), and next vary the waiting time in (i) (1,0,1) or (ii) (1,0,0). In case (i) the right spin has already been read out before the waiting time, so its spin state will not change as a function of waiting time. The spin that was originally in the center dot is moved to the right dot before the waiting time, so it will now experience a T_1 time that is more similar to T_1^1. Case (ii) shows no time-dependence for the center and right spin, and does show the T_1 decay as expected for the left dot.

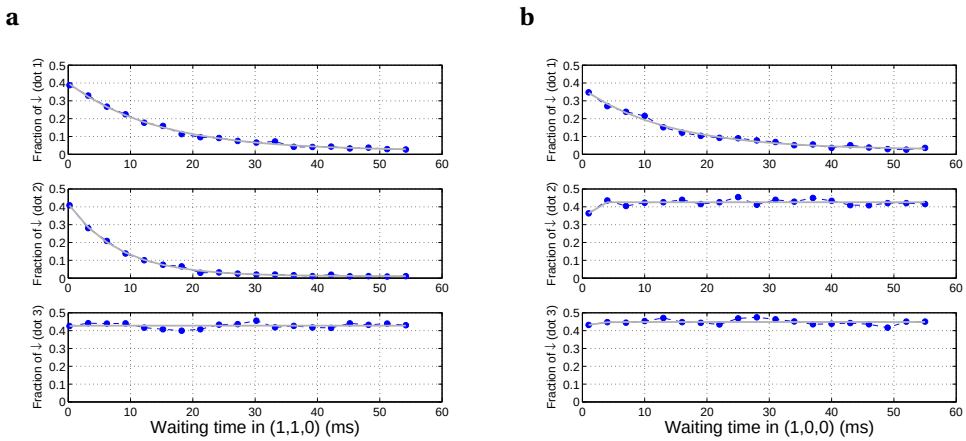

Figure 4.12: a T_1 decay in (1,0,1). Fits to the data give T_1^3 = 14.3 ms, T_1^2 = 8.2 ms. The center spin now spends most of its time in dot 3, and therefore also relaxes with the same rate as T_1^1 as measured in (1,1,1). **b** T_1 decay in (1,0,0). Fit to the data gives T_1^3 = 13.9 ms.

5

COHERENT SPIN-EXCHANGE VIA A QUANTUM MEDIATOR

T.A. Baart, T. Fujita, C. Reichl, W. Wegscheider and L.M.K. Vandersypen

Coherent interactions at a distance provide a powerful tool for quantum simulation and computation. The most common approach to realize an effective long-distance coupling 'on-chip' is to use a quantum mediator, as has been demonstrated for superconducting qubits [88, 89] and trapped ions [90]. For quantum dot arrays, which combine a high degree of tunability [26] with extremely long coherence times [91], the experimental demonstration of coherent spin-spin coupling via an intermediary system remains an important outstanding goal [92–108]. Here, we use a linear triple-quantum-dot array to demonstrate a first working example of a coherent interaction between two distant spins via a quantum mediator. The two outer dots are occupied with a single electron spin each and the spins experience a superexchange interaction through the empty middle dot which acts as mediator. Using single-shot spin read-out [47] we measure the coherent time evolution of the spin states on the outer dots and observe a characteristic dependence of the exchange frequency as a function of the detuning between the middle and outer dots. This approach may provide a new route for scaling up spin qubit circuits using quantum dots and aid in the simulation of materials and molecules with non-nearest neighbour couplings such as MnO [109, 110], high-temperature superconductors [111, 112] and DNA [113]. The same superexchange concept can also be applied in cold atom experiments [114].

manuscript submitted, arXiv:1603.03433

5.1. INTRODUCTION

Nanofabricated quantum dot circuits provide an excellent platform for performing both quantum computation and simulation using single spins [13, 26, 64, 72]. Many approaches to implementing coherent spin coupling between distant quantum dots have been proposed using a variety of coupling mechanisms. These include superconducting resonators [92–94], surface-acoustic wave resonators [95], floating metallic [96] or ferromagnetic couplers [97], collective modes of spin chains [98], superconductors [99, 100], Klein tunneling through the valence or conduction band [101] and superexchange or sequential operations via intermediate quantum dots [103–106]. A common theme among many of these proposals is to create a coupling between distant spins by virtual occupation of a mediator quantum system. So far, none of these schemes have been performed experimentally. More broadly, there are no experimental realizations so far of direct quantum gates between any type of solid-state spins at a distance.

In this Letter we focus on the superexchange interaction to induce spin-spin coupling at a distance. Superexchange is the (usually) antiferromagnetic coupling between two next-to-nearest neighbour spins through virtual occupation of a non-magnetic intermediate state [109, 110]. To date, only indirect observations of superexchange involving spins in quantum dots have been reported [115]. Given that superexchange involves a fourth order process in the hopping amplitude, it is challenging to use it for achieving coherent coupling. This is also the case for several related schemes relying on quantum mediators.

We use a linear triple-quantum-dot array with one electron on each of the outer dots, and induce a superexchange interaction through the empty middle dot, which acts as a quantum mediator. This induces spin exchange of the two distant electron spins. Using repeated single-shot spin measurements we record the coherent time evolution of the spin states on the outer dots. We control the superexchange amplitude via the detuning of the middle dot electrochemical potential relative to those of the outer dots, and study the cross-over between superexchange and conventional nearest-neighbour spin exchange.

5.2. DEVICE OPERATION

The dot array is formed electrostatically in a two-dimensional electron gas (2DEG) 85 nm below the surface of a GaAs/AlGaAs heterostructure, see Fig. 5.1a. Gate electrodes fabricated on the surface (see Methods) are biased with appropriate voltages to selectively deplete regions of the 2DEG and define the linear array of three quantum dots. The left and right dot are each occupied with one electron, and each of the two electrons constitutes a single spin-$\frac{1}{2}$ particle. The interdot tunnel couplings are set to ≈ 8.5 GHz (left-middle) and ≈ 11.8 GHz (middle-right). The sensing dot (SD) next to the quantum dot array is used for non-invasive charge sensing using radiofrequency (RF) reflectometry to monitor the number of electrons in each dot [75]. An in-plane magnetic field B_{ext} = 3.2 T is applied to split the spin-up ($\uparrow$) and spin-down ($\downarrow$) states of each electron by the Zeeman energy ($E_Z \approx 80$ μeV), defining a qubit. The electron temperature of the right reservoir is ≈ 75 mK.

In this system, superexchange can be seen as the result of the effective tunnel cou-

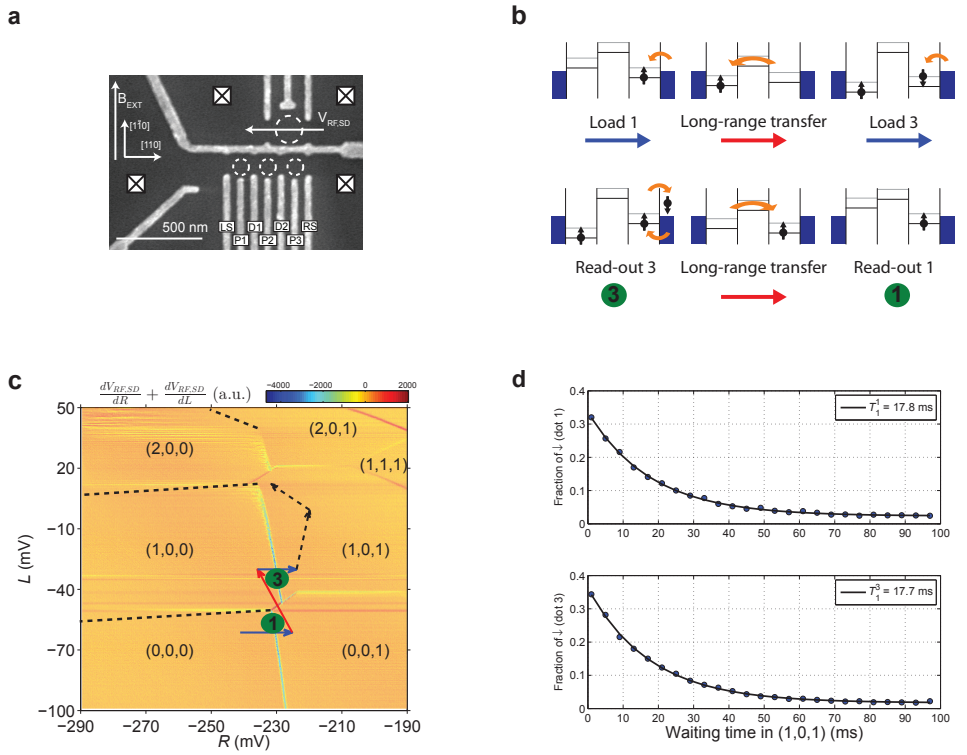

Figure 5.1: Figure 1 Linear array of three quantum dots and long-range spin transfer a Scanning electron microscopy image of a sample nominally identical to the one used for the measurements. Dotted circles indicate quantum dots and squares indicate Fermi reservoirs in the 2DEG, which are connected to ohmic contacts. The RF reflectance of the SD is monitored in order to determine the occupancies of the three dots labeled numbers 1 to 3 from left to right respectively. **b** Read from left to right and top to bottom. The array is initialized by loading two electrons from the right reservoir. The spin that is loaded first is transferred to the left dot via a second-order tunnel process across the middle dot. We load ↑-spins by tuning the loading position such that only the ↑-spin level is accessible (as in the top left diagram). Random spins are loaded by making both spin levels energetically available (top right). Spin read-out occurs using energy-selective tunneling combined with charge detection via the SD. **c** Charge stability diagram of the triple dot for M = -412 mV. Along the L and R axis, we linearly vary the voltages applied to gates P_1, P_2 and P_3 in such a way that we affect mostly the left and right dots, compensating for cross-capacitances. Similarly, M controls mostly the middle dot (see Supplementary Information 5.6.2). Labels (n,m,p) indicate the number of electrons in the left, middle and right dot respectively. The middle dot cannot be loaded directly from a reservoir [23] and the left dot is only weakly tunnel coupled to the left reservoir, leading to faintly visible charge transitions (black dotted lines indicate their positions). The pulse sequence for loading and read-out is indicated in the charge stability diagrams via blue and red arrows, see also panel b. The two black dashed arrows denote additional stages to probe superexchange (see Fig. 5.2). **d** Measured single-spin populations averaged over 8000 cycles per datapoint as a function of waiting time in (1,0,1) for dot 1 (top) and dot 3 (bottom).

pling t_{SE} between the outer dots. The amplitude of superexchange, J_{SE}, is approximated by $-\frac{t_{SE}^2}{\epsilon}$, with ϵ the detuning between the electrochemical potentials of the outer dots [13], and $\epsilon = 0$ when (1,0,1) and (2,0,0) are degenerate. Here t_{SE} can be described as $t_{SE} = (t_{m,l}\, t_{m,r})/\delta$, with $t_{m,l}$ ($t_{m,r}$) the tunnel coupling between the middle and the left

(right) site and δ the detuning between the electrochemical potential of (1,1,0) and the average of the electrochemical potentials of (1,0,1) and (2,0,0) [116]. The superexchange amplitude can thus be approximated as (see Supplementary Information 5.6.5 for the range of validity)

$$J_{SE} = -\frac{t_{m,l}^2 t_{m,r}^2}{\delta^2 \epsilon}, \tag{5.1}$$

which illustrates the characteristic fourth-order hopping process underlying superexchange.

To provide direct evidence of coherent superexchange, we will probe the resulting time evolution of the two spins via repeated single-shot measurements using spin-to-charge conversion [47]. It is beneficial to perform this conversion as close as possible to the charge sensor, SD, to achieve high read-out fidelities. In previous work, we therefore shuttled electrons consecutively from left to middle to right with no detectable sign of spin flips upon shutting [117]. Here, we explore a different approach, transferring the spin from left to right with only virtual occupation of the middle dot, using the same long-range tunnel coupling that underlies coherent superexchange [115]. We test the two-spin read-out and long-range spin transfer as described by the schematic diagrams of Fig. 5.1b and implemented by the pulse sequence depicted by the blue and red arrows in Fig. 5.1c. Starting from an empty array, we load a random electron from the reservoir into the right dot by pulsing into the charge state (0,0,1). Next we pulse into (1,0,0), whereby the electron is transferred from the rightmost dot to the leftmost dot via a second-order tunnel process across the middle dot. For this transfer we temporarily pulse δ closer to 0 to increase the long-range shuttling rate (see Supplementary Information 5.6.1). Finally, we once more load a random electron in the right dot by pulsing to (1,0,1). We vary the waiting time in (1,0,1) during which spins relax to the spin ground state $|\uparrow 0 \uparrow\rangle$. Then we reverse the pulse sequence and add two calibrated read-out stages denoted by the green circles where spin-to-charge conversion takes place. Fig. 5.1d shows the measured decays to the ground state spin-up for each of the two spins. We report read-out fidelities of on average 95.9% and 98.0% for spin-down and spin-up respectively, assuming no spin flips during the spin transfer [117] (see Supplementary Information 5.6.3).

5.3. KEY SIGNATURE OF SUPEREXCHANGE DRIVEN OSCILLATIONS

A key signature of superexchange driven spin oscillations is their dependence on the detuning of the intermediate level (δ), see Eq. (5.1). We have therefore created linear combinations of the gates P_1, P_2 and P_3 in such a way that we can independently vary δ and ϵ as can be seen in Fig. 5.2b. Superexchange occurs in the (1,0,1) charge configuration, and the superexchange amplitude, J_{SE}, increases for less negative ϵ, which translates to an operating point closer to the (2,0,0)-configuration, see Fig. 5.2a. Similarly, J_{SE} increases with less negative δ, up to the point where we cross the (1,0,1)-(1,1,0) transition indicated by the black dashed line in Fig. 5.2b and spin exchange between nearest-neighbour dots will dominate (see Fig. 5.2c). To capture the expected time evolution, we must take into account a difference in Zeeman energies between the two dots, $\Delta E_z = E_{z,3} - E_{z,1}$, arising from slight differences in the g-factor for each dot [117]. Spin exchange defines one rota-

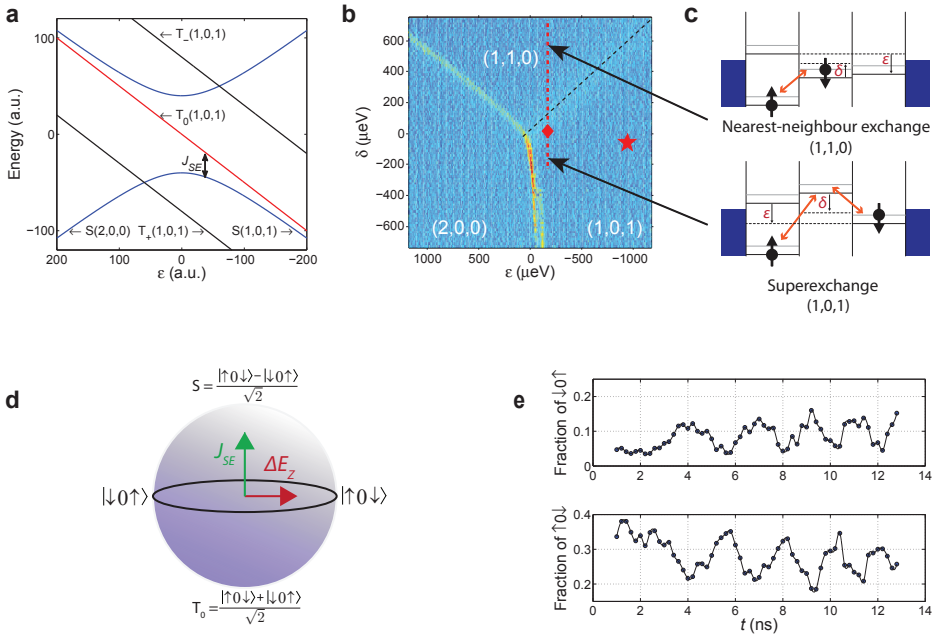

Figure 5.2: Superexchange-driven spin oscillations a Energy diagram as a function of ϵ for $\delta < 0$. The long-range tunnel coupling induces an anti-crossing between the (1,0,1) and (2,0,0) singlet states. The energy difference between T_0 and the hybridized S is denoted J_{SE}. The T_- and T_+ states are split off by B_{ext}. **b** Charge stability diagram in detuning space, allowing individual control of the detuning of the middle dot (δ) and between the outer dots (ϵ), see panel c. **c** Cartoon depicting the transition from superexchange to nearest-neighbour exchange as δ is made more positive. **d** Bloch sphere representation of $S - T_0$ subspace in the superexchange regime with control axes J_{SE} and ΔE_Z. **e** Observation of superexchange-driven spin oscillations. Starting with a mixture of $|\uparrow 0 \downarrow\rangle$ and $|\uparrow 0 \uparrow\rangle$ at the position of the red star in b, we pulse ϵ for a varying amount of time to the position indicated by the red diamond. Afterwards the four two-spin probabilities are measured by averaging over 999 single-shot cycles per datapoint, two of which are shown.

tion axis, the Zeeman energy difference an orthogonal axis, as shown in the Bloch sphere in Fig. 5.2d. In the experiment, ΔE_z is fixed, and J_{SE} can be controlled by gate voltage pulses, as we discussed. By adjusting J_{SE}, we can thus define the net rotation axis and rate [118]. A similar Bloch sphere can be made for the nearest-neighbour regime.

The protocol for probing the time evolution is as follows. Starting with an empty array, we create a mixture of $|\uparrow 0 \downarrow\rangle$ and $|\uparrow 0 \uparrow\rangle$ and move to the position of the red star in Fig. 5.2b, where J_{SE} is small compared to ΔE_Z. This is achieved by sequentially loading the two spins as in Fig. 5.1c, in this case loading a $\uparrow$ in the left dot and a random spin in the right dot. This procedure allows us to conveniently create an anti-parallel spin state without using more involved techniques such as electron spin resonance. Next, following the black dashed arrows in Fig. 5.1c, we pulse towards the (2,0,0) regime and wait for several ns. The exact location in detuning space is marked in Fig. 5.2b by a red diamond. At this point J_{SE} is sizable, $|\uparrow 0 \downarrow\rangle$ is not an eigenstate of the Hamiltonian and is thus expected to evolve in time, periodically developing a $|\downarrow 0 \uparrow\rangle$ component ($|\uparrow 0 \uparrow\rangle$ will only acquire an overall phase). The larger $J_{SE}/\Delta E_Z$, the larger the $|\downarrow 0 \uparrow\rangle$ component.

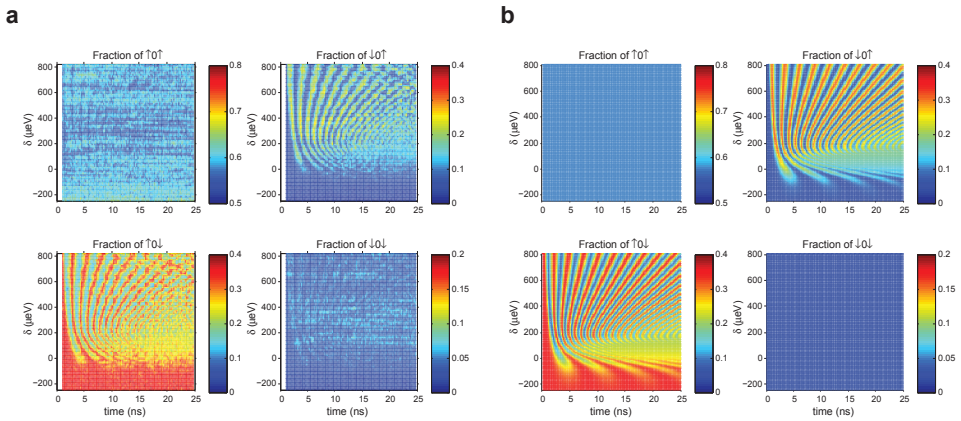

Figure 5.3: Transition from superexchange to nearest-neighbour exchange a Starting with a mixture of $|\uparrow 0 \downarrow\rangle$ and $|\uparrow 0 \uparrow\rangle$ at the position of the red star in Fig. 5.2b, we pulse ϵ and δ for a varying amount of time to the position indicated by the vertical dashed line in Fig. 5.2b. Afterwards the four two-spin probabilities are measured by averaging over 999 single-shot cycles per datapoint. We clearly note the transition of oscillations dominated by ΔE_z ($\delta < -50$ μeV) to increasingly faster superexchange dominated spin evolution and finally ($\delta > 200$ μeV) nearest-neighbour exchange dominated evolution, which slows down as δ is further increased. Acquiring this set of data took ~20 hours. **b** Simulation of the data shown in a. The independently determined input parameters are: $t_{m,l}$ = 8.5 GHz, $t_{m,r}$ =11.8 GHz, $E_{z,1}$ =19.380 GHz, $E_{z,2}$ =19.528 GHz, $E_{z,3}$ =19.510 GHz and the risetime of the detuning pulse is 0.8 ns (see Supplementary Information 5.6.4).

We pulse back to the position of the red star in (1,0,1) and follow the same spin readout procedure as was done for the T_1-measurement in Fig. 5.1d. Fig. 5.2e shows the $|\uparrow 0 \downarrow\rangle$ and $|\downarrow 0 \uparrow\rangle$ probability as a function of the length of the detuning pulse. We see a sinusoidal dependence, with the $|\uparrow 0 \downarrow\rangle$ and $|\downarrow 0 \uparrow\rangle$ populations evolving in anti-phase, as expected.

Returning to the key signature of superexchange, we fix the value of ϵ and vary δ along the vertical dashed line shown in Fig. 5.2b. For each choice of δ, we record the four two-spin probabilities as a function of the length of the detuning pulse (Fig. 5.3a). Starting from large negative δ, we first observe no oscillations at all: the superexchange mechanism is suppressed and the $|\uparrow 0 \downarrow\rangle$-state remains fixed along the x-axis of the Bloch sphere. As we bring the electrochemical potential of the intermediate level closer to that of the outer dots, J_{SE} increases in magnitude and slow oscillations ~ 150 MHz start appearing that are still dominated by $\Delta E_z \approx 130$ MHz between the outer dots, hence the low contrast of the oscillations. The oscillations become faster up to ~ 900 MHz as δ is increased at which point J_{SE} is stronger than ΔE_z and the contrast increases. When δ is further increased, the (1,1,0)-state becomes energetically favourable and the nearest-neighbour exchange between the left and middle dot dominates. Here $\epsilon = -170$ μeV and this transition occurs around $\delta = 120$ μeV, which is where the black-dashed line inFig. 5.2b is crossed. Increasing δ even more enlarges the detuning between the left and middle dot and thereby slows down the nearest-neighbour oscillations, as seen in the data.

5.4. DISCUSSION

For a quantitative comparison with the theoretical predictions, we show in Fig. 5.3b the expected time evolution of the system modeled using the measured nearest-neighbour tunnel couplings, detunings δ and ϵ, and the difference in Zeeman energy probed through electric-dipole spin resonance measurements [76]. We include the effect of dephasing by charge noise [118] via a single parameter to match the decay of the oscillations and account for the known read-out fidelities (see Supplementary Information 5.6.4). Fig. 5.2e shows that it takes more than 1 ns for the superexchange to be turned on. This is caused by the finite risetime of the pulses produced by the arbitrary waveform generator and finite bandwidth of the coax lines. The simulation includes this gradual turn on and off of J_{SE}. Comparing Fig. 5.3a and Fig. 5.3b we report good agreement between theory and experiment, which supports our interpretation of the data in terms of superexchange, including the transition to nearest-neighbour exchange.

In summary, we have demonstrated a first working example of a direct quantum gate between solid-state spins at a distance via virtual occupation of a quantum mediator. This result underlines the utility of arrays of quantum dots for the investigation and application of fundamental physical processes driven by small-amplitude terms and higher-order tunneling. It is possible to extend the distance between the coupled spins using elongated intermediate quantum dots or via different (quantum) mediators altogether. Another interesting direction is to create non-nearest neighbour spin-spin interactions with the centre dot occupied [105, 106], which opens up further new possibilities for quantum computation and modeling of complex materials.

5.5. METHODS

The experiment was performed on a GaAs/$Al_{0.25}Ga_{0.75}As$ heterostructure grown by molecular-beam epitaxy, with a 85-nm-deep 2DEG with an electron density of $2.0 \cdot 10^{11}$ cm^{-2} and mobility of $5.6 \cdot 10^{6}$ cm^{2}V^{-1}s^{-1} at 4 K. The metallic (Ti-Au) surface gates were fabricated using electron-beam lithography. The device was cooled inside an Oxford Kelvinox 400HA dilution refrigerator to a base temperature of 45 mK. To reduce charge noise, the sample was cooled while applying a positive voltage on all gates (ranging between 250 and 350 mV) [85]. The main function of gates LS and RS is to set the tunnel coupling with the left and right reservoir, respectively. D_1 and D_2 control the interdot tunnel coupling and P_1, P_2 and P_3 are used to set the electron number in each dot. The device was tuned to the single-electron regime. Gates P_1, P_2, P_3 and D_2 were connected to homebuilt bias-tees (RC= 470 ms), enabling application of d.c. voltage bias as well as high-frequency voltage excitation to these gates. The microwaves were generated using a HP83650A connected to P_2 via a homemade bias-tee at room temperature. Voltage pulses to the gates were applied using a Tektronix AWG5014. RF reflectometry of the SD was performed using an LC circuit matching a carrier wave of frequency 111.11 MHz. The inductor is formed from a microfabricated NbTiN superconducting spiral inductor with an inductance of 3.0 μH. The power of the carrier wave arriving at the sample was estimated to be -103 dBm. The carrier signal is only unblanked during read-out. The reflected signal was amplified using a cryogenic Weinreb CITLF2 amplifier and subsequently demodulated using homebuilt electronics. Real time data acquisition was per-

formed using a FPGA (field-programmable gate array DE0-Nano Terasic) programmed to detect tunnel events using a Schmitt trigger.

5.6. SUPPLEMENTARY MATERIAL

Parts of the supplementary material were already published in [117] (see Chapter 4) and are repeated here to make the text more self-contained.

5.6.1. DETAILED INFORMATION OF THE APPLIED PULSE SEQUENCE

In this section we give detailed information on the applied pulse sequences. Fig. 5.4 shows the same charge stability diagram as Fig. 5.1c from the main text with additional labeling. Table 5.1 gives an explanation including the details of the relevant stages. To correct for slow variations in the dot levels as a function of time (hours timescale), we always calibrate the two read-out stages before each longer measurement such as a complete T_1 decay (~20,000 datapoints taken after one calibration run, which takes about half an hour).

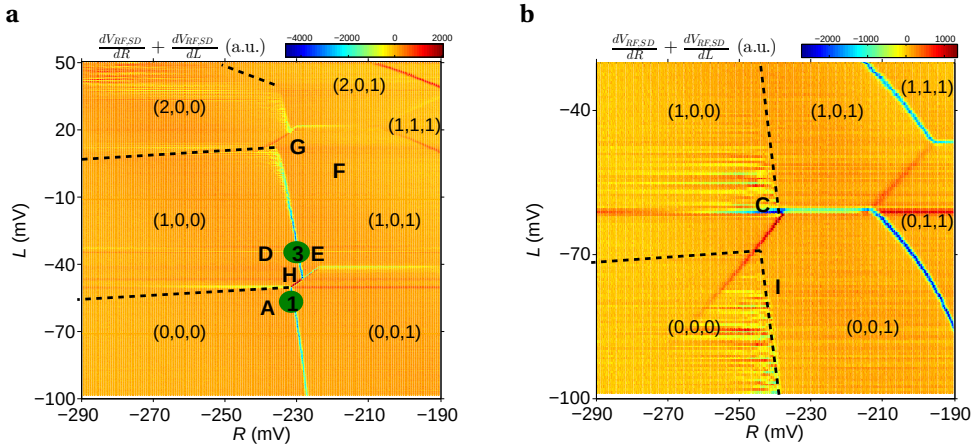

Figure 5.4: Charge stability diagram for **a** M= -412 mV and **b** M= -382 mV with added details for the pulse sequence as explained in Table 5.1.

Stage(s)	**Purpose and details**
A	Emptying stage (lasting 200 μs) during which all dots are emptied.
A → Stage 1	Loading an ↑-spin from the right reservoir into the right dot. The electrochemical potential of the dot is tuned such that only ↑-states will enter the dot. We wait 200 μs in stage 1.
Stage 1 → C	Shuttle electron from the right to the left dot via a second-order tunnel process across the middle dot. We temporarily pulse M 30 mV more positive (-382 mV) to increase the long-range shuttling rate. Waiting time at C is 5 μs. We did not observe any charge exchange with the reservoir at point C. This is also substantiated by the high spin-up fidelity: charge exchange results in the loading of random spins and would therefore increase the offset of the T_1-curves.
C → D	We pulse M back to the value M= -412. Waiting time at D is 10 μs.
D → E	Load a random electron from the right reservoir. Waiting time at E is 100 μs.
E → F	Prepare exchange gate. Waiting time at F is 1 μs.
F → G	Pulse into exchange position G for a varying time.
G → F	Start read-out sequence. Waiting time at F is 1 μs.
F → Read-out stage 3	Gate voltage pulses larger than ~2 mV produce a spike in the RF-read-out signal. To prevent false events, we therefore first pulse to a position close to the read-out stage (2 mV more positive in R) and wait for 2 μs. Only then, the RF-signal is unblanked and next we pulse into the read-out configuration for 150 μs.
Read-out stage 3 → H	Empty the right dot for 50 μs.
H → I	Shuttle electron from the left to the right dot. We temporarily pulse M 30 mV more positive to increase the long-range shuttling rate. Waiting time at I is 5 μs. Point I is positioned relatively far away from the interdot transition (1,0,0)-(0,0,1) to circumvent so-called hot-spots where spin relaxation occurs on the sub-μs timescale [81]. We did not observe any charge exchange with the reservoir at point I.
I → Read-out stage 1	Similar as Read-out stage 3.
Compensation stage	At the end of the pulse sequence we add a compensation stage of ~0.5 ms to ensure that the total DC-component of the pulse is zero. This prevents unwanted offsets of the dot levels due to the bias tees.

Table 5.1: Detailed explanation of the applied pulse sequence as described by Fig. 5.4. Unless noted otherwise, we always ramp from one point to the other (ramp time is 1 μs). The total duration of this sequence is around 900 μs, not including the compensation stage at the end.

5.6.2. VIRTUAL GATES L, M AND R

To control the electron number inside each dot we change the voltages on gates P_1, P_2 and P_3. In practice each gate couples capacitively to all three dots. Changing for example P_1 which couples mostly to dot 1, will therefore also influence dot 2 and 3. To make selective control of each dot easier it is convenient to correct for this capacitive cross-coupling. This can be done by measuring the cross-capacitance matrix for the three gates recording the influence of each gate on every dot. Inverting this matrix allows us to create charge stability diagrams with vertical and horizontal charge transitions in a so-called 'virtual gate'-space. In such a 'virtual gate'-space, the real gates P_1, P_2 and P_3 have been replaced by linear combinations of the three gates which allow the user to change the chemical potential in one dot, without changing the chemical potential in the neighboring dots.

For this experiment the exact relation between P_1, P_2 and P_3 and the 'virtual gates' L, M and R used is given by

$$\begin{pmatrix} L \\ M \\ R \end{pmatrix} = \begin{pmatrix} 1.56 & 0.0 & 0.40 \\ 0.0 & 1.56 & 0.0 \\ 0.20 & 0.51 & 1.05 \end{pmatrix} \begin{pmatrix} P_1 - P_{1,\text{offset}} \\ P_2 - P_{2,\text{offset}} \\ P_3 - P_{3,\text{offset}} \end{pmatrix}$$

with $P_{1,\text{offset}} = 23.99$ mV, $P_{2,\text{offset}} = 61.01$ mV, $P_{3,\text{offset}} = -111.6$ mV. This set of virtual gates did not perfectly correct for cross-capacitances, as the capacitances themselves turn out to slightly vary with the gate voltages. Working with virtual gates does however give one large freedom to take slices at any angle through the 3D honeycomb diagram that satisfy the requirements for the experiment.

5.6.3. DETAILS ON CALCULATION OF THE READ-OUT FIDELITIES

We obtained our read-out fidelities in a similar way as described in [117]. The numbers used to obtain these fidelities are summarized in Table 5.3. Parameters T_1^j and α^j were extracted from Fig. 5.1d of the main text by fitting it to $p^j \cdot e^{-t/T_1^j} + \alpha^j$. The tunnel rates with the reservoir, $\Gamma_{out}^{\downarrow,i}$ and $\Gamma_{in}^{\uparrow,i}$, were determined from the histograms depicted in Fig. 5.5. The measurement bandwidth, $B^j(\tau)$, is extracted from Fig. 5.6.

dot nr.	Spin-down fidelity (%) (worst,best)	Spin-up fidelity (%) (worst,best)
1	95.8 (95.4, 96.1)	97.7 (97.5, 97.9)
3	96.0 (95.5, 96.3)	98.3 (98.1, 98.5)

Table 5.2: Read-out fidelities per dot. Values in brackets show the 95% confidence intervals based on the fits.

dot nr.	T_1 (ms) (worst,best)	$\Gamma_{out}^{\downarrow,i}$ (kHz) (worst,best)	$\Gamma_{in}^{\uparrow,i}$ (kHz) (worst,best)	Read-out time (μs)	T_{wait}^{3} (μs)
1	17.8 (17.2, 18.4)	79.75 (78.89, 80.61)	123.61 (125.29, 121.92)	150	60.25
3	17.7 (17.2, 18.3)	77.71 (76.93, 78.48)	153.51 (154.51, 152.51)	150	-

Table 5.3: Overview of the required parameters to calculate the read-out fidelities as described in [117]. Values in brackets show the 95% confidence intervals based on the fits.

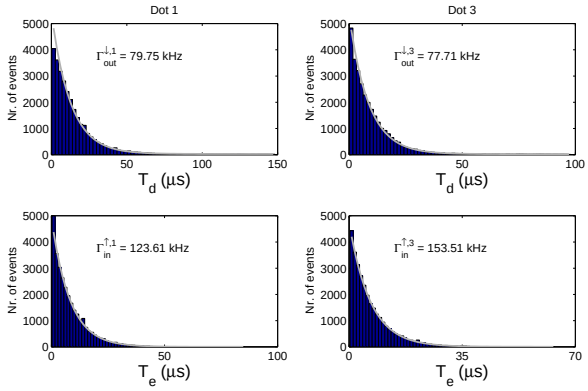

Figure 5.5: Top row: histograms showing the distribution of the time T_d it takes a spin-down electron to tunnel out at the read-out position of each respective dot for a measurement similar to the one shown in Fig. 5.1d of the main text. The line is an exponential fit from which we determine the decay rate given by $\Gamma_{out}^{\downarrow,j} + \frac{1}{T_1^j}$. Bottom row: histograms showing the distribution of the time T_e it takes a spin-up electron to tunnel back into the empty dot. The grey line is an exponential fit from which we can extract the tunnel rate given by $\Gamma_{in}^{\uparrow,j}$.

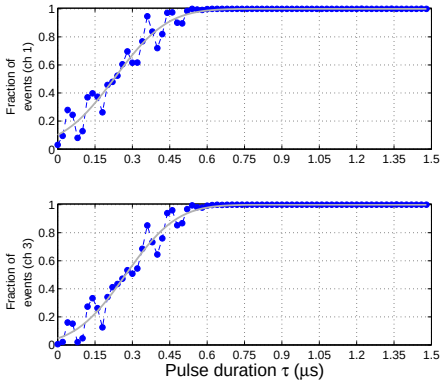

Figure 5.6: The probability of detecting a pulse with duration τ for each of the two read-out channels ($B^j(\tau)$). Every read-out stage is monitored by a separate input channel of the FPGA. The output of the demodulation box is low-pass filtered at 1 MHz. The sensitivity of the SD is slightly different for the two different read-out stages as they occur at different detunings of the plunger gates. Each datapoint is an average of 999 measurements.

5.6.4. SIMULATION OF THE EXPERIMENT

In this section we describe how we calculated the simulated data as shown in Fig. 5.3b of the main text.

THEORETICAL MODEL

We model our system using the following hamiltonian, defined in the $S(200)$, $S(110)$, $T_0(110)$, $S(101)$, $T_0(101)$ basis.

$$H = \begin{pmatrix} -\epsilon/2 & t_l & 0 & 0 & 0 \\ t_l & -\delta & \Delta E_{z,21}/2 & t_r & 0 \\ 0 & \Delta E_{z,21}/2 & -\delta & 0 & t_r \\ 0 & t_r & 0 & \epsilon/2 & \Delta E_{z,31}/2 \\ 0 & 0 & t_r & \Delta E_{z,31}/2 & \epsilon/2 \end{pmatrix}$$

The matrix elements are defined as follows:

- ϵ is the detuning between the outer dots
- δ is the detuning of the middle dot with respect to the average of the outer dots
- t_l is the tunnel coupling between the $S(200)$ and $S(110)$ state
- t_r is the tunnel coupling between the (110) and (101) state
- $\Delta E_{z,21}$ is the difference in Zeeman energy between dot 1 and 2, defined as $E_{z,2} - E_{z,1}$.
- $\Delta E_{z,31}$ is the difference in Zeeman energy between dot 1 and 3, defined as $E_{z,3} - E_{z,1}$.

We have to solve the time-dependent Schrödinger equation to incorporate the finite rise- and falltime of the AWG:

$$i\hbar \frac{\partial}{\partial t} \Psi(t) = H(\epsilon(t), \delta(t))\, \Psi(t) \tag{5.2}$$

We numerically approximate the time evolution of $\Psi(t)$ by discretizing time in steps Δt and calculating $\Psi(t + \Delta t) = e^{-iH(t)\Delta t/\hbar}\Psi(t)$. We model the time dependence of $\epsilon(t)$ and $\delta(t)$ as follows:

If $t < t_f$:

$$\epsilon(t) = \left[\epsilon(t_f) - \epsilon(0)\right] \cdot (1 - e^{-t/t_{rise}}) + \epsilon(0) \tag{5.3}$$

$$\delta(t) = \left[\delta(t_f) - \delta(0)\right] \cdot (1 - e^{-t/t_{rise}}) + \delta(0) \tag{5.4}$$

Else:

$$\epsilon(t) = \left[\epsilon(t_f) - \epsilon(0)\right] \cdot (1 - e^{-t_f/t_{rise}}) \cdot e^{-(t-t_f)/t_{rise}} + \epsilon(0) \tag{5.5}$$

$$\delta(t) = \left[\delta(t_f) - \delta(0)\right] \cdot (1 - e^{-t_f/t_{rise}}) \cdot e^{-(t-t_f)/t_{rise}} + \delta(0) \tag{5.6}$$

Where $(\epsilon(0), \delta(0))$ denotes the starting point (red star symbol in Fig. 5.2b), $(\epsilon(t_f), \delta(t_f))$ the detuning point programmed in the AWG, t_f the programmed time to spend in $(\epsilon(t_f), \delta(t_f))$, and t_{rise} the risetime of the pulse arriving at the sample.

We add pure electrical dephasing by multiplying with an amplitude decay of the form $e^{-\left(t_{\mathrm{SWAP}}/T_2^*\right)^2}$ [118]. The sensitivity of T_2^* to charge noise is approximated by $T_2^* = \frac{T_{2,\mathrm{factor}}}{\sqrt{\left(\left(\frac{\partial}{\partial\epsilon}J(\epsilon(t_f),\delta(t_f))\right)^2+\left(\frac{\partial}{\partial\delta}J(\epsilon(t_f),\delta(t_f))\right)^2\right)}}$. The simulations shown use $T_{2,\mathrm{factor}} = 0.25$ ns. This model does not incorporate the change in T_2^* during the risetime of the pulse, which could be incorporated in future work. Especially pulses traversing the transition from superexchange (1,0,1) to nearest neighbour exchange (1,1,0) suffer from a temporarily shorter T_2^* than the value calculated at $(\epsilon(t_f),\delta(t_f))$. For completeness Fig. 5.7 shows the simulation with no dephasing.

We correct for the read-out fidelities by introducing the fidelity matrix **F**:

$$\mathbf{F} = \begin{pmatrix} F_\uparrow^1 F_\uparrow^3 & F_\uparrow^1(1-F_\downarrow^3) & (1-F_\downarrow^1)F_\uparrow^3 & (1-F_\downarrow^1)(1-F_\downarrow^3) \\ F_\uparrow^1(1-F_\uparrow^3) & F_\uparrow^1 F_\downarrow^3 & (1-F_\downarrow^1)F_\uparrow^3 & (1-F_\downarrow^1)F_\downarrow^3 \\ (1-F_\uparrow^1)F_\uparrow^3 & (1-F_\uparrow^1)(1-F_\downarrow^3) & F_\downarrow^1 F_\uparrow^3 & F_\downarrow^1(1-F_\downarrow^3) \\ (1-F_\uparrow^1)(1-F_\uparrow^3) & (1-F_\uparrow^1)F_\downarrow^3 & F_\downarrow^1(1-F_\uparrow^3) & F_\downarrow^1 F_\downarrow^3 \end{pmatrix}$$

Where $F_\uparrow^i$ and $F_\downarrow^i$ are the read-out fidelities for dot i (see Table 4.1). We denote the measured four two-spin probabilities at time t by $\Pi_{\mathrm{measured}}(t) = (P_{\uparrow\uparrow}, P_{\uparrow\downarrow}, P_{\downarrow\uparrow}, P_{\downarrow\downarrow})$. The actual two-spin probabilities $\Pi(t)$, i.e. corrected for the read-out fidelities, can be found by solving the linear equations $\Pi_{\mathrm{measured}}(t) = \mathbf{F}\Pi(t)$. The linear equations are solved by numerically minimizing the squared length of the vector $\Pi_{\mathrm{measured}}(t) - \mathbf{F}\Pi(t)$ and restricting the solutions $\Pi(t)$ to physical solutions (all elements have to be positive and the sum of the elements has to be one, since the vector consists of four two-spin probabilities). Using this method we determine $\Pi(t=0)$, which is used as initial condition for the simulation. The outcome of the simulation, $\Pi(t)$, is multiplied by **F** to calculate the theoretically expected $\Pi_{\mathrm{measured}}(t)$ as shown in Fig. 5.3b of the main text.

INPUT PARAMETERS

Zeeman energy E_z: The Zeeman energy in each dot has been measured using electric-dipole spin resonance (EDSR) in a similar way as in Ref. [76]. At 3.2 T the Zeeman energy is 19.380 GHz, 19.528 GHz and 19.510 GHz for dot 1, 2 and 3 respectively.

Tunnel couplings t_l and t_r: The tunnel coupling at zero detuning between neighbouring dots was measured using photon-assisted tunneling [86], see Fig. 5.8. These measurements were also used to determine the lever arm α_i of each gate for ϵ and δ. t_r was measured at: $(\epsilon,\delta) = (-230, 180)$ μeV. This is close to the detuning where the data of Fig. 5.3a was acquired. The value of t_l had to be measured however for a different tuning: $(\epsilon,\delta) = (230, 180)$ μeV. Tunnel couplings depend strongly on the exact gate voltages. We measured for example that decreasing δ by 300 μeV whilst staying on the (2,0,0)-(1,1,0) transition decreases t_l by ~30%. At the detuning of the experiment most datapoints are taken away from the (2,0,0)-(1,1,0) transition in the direction of the (1,1,0)-regime where t_l will be even further reduced [119]. We find a good match between experiment and simulation by keeping t_r fixed at the measured 11.8 GHz and lowering the measured t_l by 45% to 8.5 GHz. We have verified that changing t_l is the most efficient way to get good agreement with experiment. t_l strongly influences the oscillations for positive δ, whilst

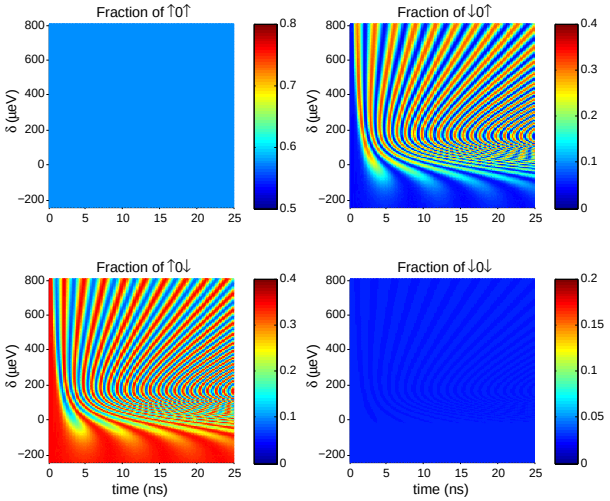

Figure 5.7: Same simulation as Fig. 5.3a of the main text without the dephasing term.

the product of t_l and t_r dominates for negative δ. This allowed us to determine that t_l had to be changed and not t_r. Future work could incorporate the precise dependence of tunnel coupling on detuning.

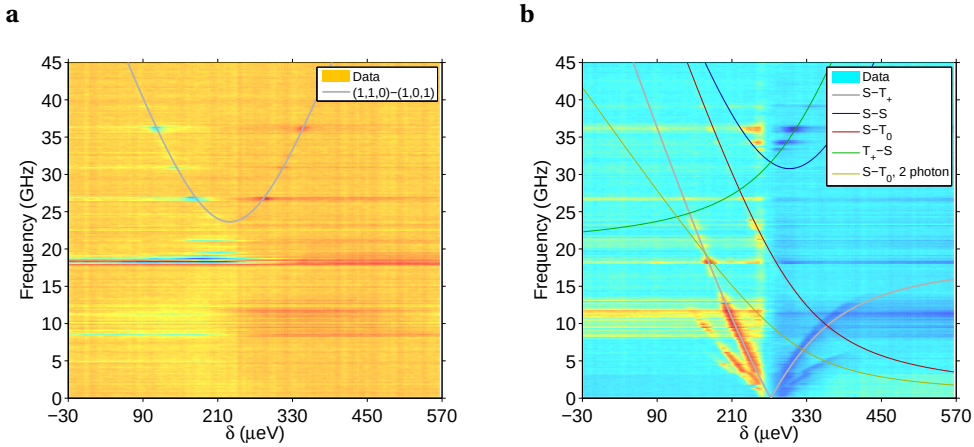

Figure 5.8: Charge sensor signal as a function of frequency versus δ between: **a** (1,1,0) and (1,0,1) at $\epsilon = -230$ μeV, **b** (2,0,0) and (1,1,0) at $\epsilon = 230$ μeV. The data in **a** is fitted to $\sqrt{((M-M_{\text{offset}})\cdot\alpha_M)^2+4t_r^2}$ giving $t_r = 11.8 \pm 0.6$ GHz. In **b** we fit the $S-T_+$-transition that is clearly visible to $\left|\left(\sqrt{((M-M_{\text{offset}})\cdot\alpha_M)^2+4t_l^2}-((M-M_{\text{offset}})\cdot\alpha_M)\right)/2-\left(E_{z,1}+E_{z,2}\right)/2\right|$ giving $t_l = 15.4 \pm 1.3$ GHz. Based on this fit we also plot the expected position of multiple other transitions.

$\epsilon(t_f)$, $\delta(t_f)$ and t_{rise} : The model described in Eq. (5.3)-(5.6) is an approximation to the true shape of the pulse. The measured output of the AWG including the low pass filter (MiniCircuits SBLP-300+) can be modeled well with $t_{rise} \approx 0.8$ ns. The coax cables inside the dilution refrigerator show a shorter t_{rise} (<600 ps), but in addition suffer from the skin effect. Due to this effect it takes several ns to reach the final voltage value on the sample. In practice this means that for short pulses (< few ns) Eqs. (5.3)-(5.6) work fine if $\epsilon(t_f)$ and $\delta(t_f)$ are reduced in magnitude to incorporate the skin effect. This is also seen in practice by measuring a pulsed version of charge stability diagram Fig. 5.2b of the main text. Fig. 5.2b depicts the charge stability diagram when changing the detunings relatively slowly (~ms timescale per horizontal trace). To verify that the fast (~ns) pulses arrive at slightly different points in detuning-space, we create a mixture of $\uparrow 0 \downarrow$ and $\uparrow 0 \uparrow$ in (1,0,1) and pulse for 5 ns to the same detunings as Fig. 5.2b and detect the spin-state. This pulse starts at $(\epsilon, \delta) \approx (-950, 0)$. Fig. 5.9 shows the expected three regimes: (1) as long as the pulse stays within the (1,0,1)-region no spin evolution occurs, (2) pulsing into the (2,0,0)-region leads to a mixture of the $\uparrow 0 \downarrow$, $\downarrow 0 \uparrow$ and $\uparrow 0 \uparrow$ states as a consequence of full dephasing during the superexchange and (3) pulsing into (1,1,0) induces coherent nearest-neighbour exchange. Comparing Fig. 5.9 and Fig. 5.2b shows that the transition from (1,0,1) to (2,0,0) takes place at a more positive ϵ as expected: ~300 μeV. This is attributed to the skin effect inside the coax cables. A similar measurement for a pulse time of 1 μs does not show this shift. The data in Fig. 5.3a is taken for $\epsilon(t_f) = 0$. To compensate for the skin effect we need to input a more negative value for ϵ in the simulation to get good agreement with the data: -170 μeV. To make a perfect model one could first measure the precise pulse shape arriving at the sample more carefully.

Despite some uncertainty in the exact value of some of the input parameters, within a reasonable range of inputs all give a similar qualitative picture. They all show the change from a regime driven by $\Delta E_{z,31}$ for negative δ, to superexchange oscillations that become faster as δ is increased to a regime of nearest-neighbour oscillations that slow down as δ becomes more positive. This underlines that our experimental data indeed shows the transition from superexchange to nearest-neighbour exchange.

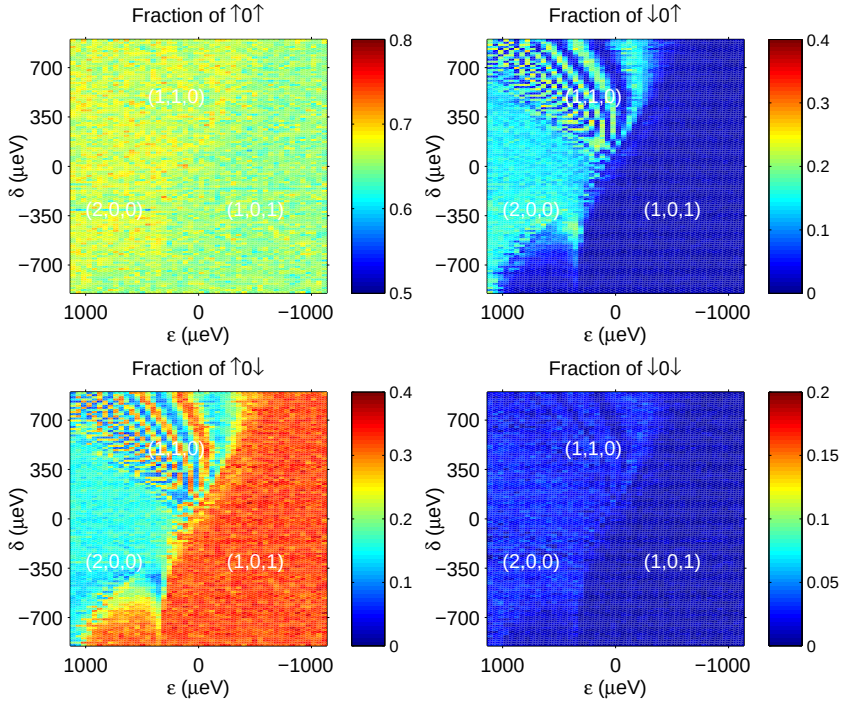

Figure 5.9: Pulsed version of charge stability diagram Fig. 5.2b of the main text. We create a mixture of $\uparrow 0 \downarrow$ and $\uparrow 0 \uparrow$ in (1,0,1) and pulse for 5 ns to the same detunings as Fig. 5.2b and detect the spin-state.

5.6.5. COMPARISON OF THE QUALITY FACTOR OF SUPEREXCHANGE VERSUS NEAREST-NEIGHBOUR EXCHANGE

In this section we make a comparison of the charge-noise sensitivity of superexchange versus nearest-neighbour exchange. This allows us to compare the quality factor, Q, in the regime where charge noise is the dominant source of dephasing (i.e. $J > \Delta E_Z$). Q is proportional to the number of visible exchange oscillations within the dephasing time: $Q \propto J \cdot T_2^*$.

We start with an approximation of the nearest-neighbour exchange interaction J_N by [13]

$$J_N \approx -\frac{t_N^2}{\epsilon}, \tag{5.7}$$

with t_N the neareast-neighbour tunnel coupling and ϵ the detuning between the dots. This approximation is valid in the regime where $t_N \ll |\epsilon|$ and $\epsilon < 0$. We assume that fluctuations in ϵ are the dominant contribution to dephasing and neglect dephasing from other fluctuating parameters [118]. The sensitivity to charge noise is then given by

$$\frac{\partial}{\partial \epsilon} J_N = \frac{t_N^2}{\epsilon^2} \tag{5.8}$$

For a fixed J_N and t_N the sensitivity to charge noise is

$$\frac{\partial}{\partial \epsilon} J_N = \left(\frac{J_N}{t_N}\right)^2 \tag{5.9}$$

This results in a Q of

$$Q \propto \frac{J}{\frac{\partial}{\partial \epsilon} J} = \frac{t_N^2}{J_N} \tag{5.10}$$

Note that in this approximation, a larger Q for a fixed J is obtained by increasing the tunnel coupling.

A similar first order approximation can be made for the superexchange regime. It however only gives reliable results for a small portion of the detuning space. To give a fair comparison between nearest-neighbour and superexchange we therefore used the same model as in section 5.6.4 to numerically calculate J and the effect of charge noise for each value of δ and ϵ. Assuming uncorrelated, equal magnitude noise in δ and ϵ results in the following expression for the charge-noise sensitivity

$$\sqrt{\left(\frac{\partial}{\partial \epsilon} J\right)^2 + \left(\frac{\partial}{\partial \delta} J\right)^2} \tag{5.11}$$

and we approximate Q by

$$Q \propto \frac{J}{\sqrt{\left(\frac{\partial}{\partial \epsilon} J\right)^2 + \left(\frac{\partial}{\partial \delta} J\right)^2}} \tag{5.12}$$

For simplicity we set the g-factor differences to 0 and assume equal nearest-neighbour tunnel couplings t. The calculated $\log(Q)$ for $t = 40$ μeV is shown in Fig. 5.10a. White contour lines indicate constant J for several different values of J. From Fig. 5.10a we can conclude the following if we limit ourselves to the (1,1,0)- and (1,0,1)-regime: for a fixed J, the best Q is always obtained by operating in the short-range regime (1,1,0). (Please note that all white lines in (1,0,1) eventually enter the (1,1,0)-regime; for several contour lines this happens outside the plotted detuning range of the figure.)

It is possible to boost the performance of both superexchange and nearest-neighbour exchange by increasing the interdot tunnel coupling. In Fig. 5.10b and c we plot how much Q and J change respectively when t is doubled to $t = 80$ μeV. This shows that the Q and J of superexchange both improve inside the (1,0,1)-region by increasing t, allowing one to induce more oscillations at higher speed. Inside the nearest-neighbour region (1,1,0) there is also a large region where both Q and J increase.

We can also include the (2,0,0)-region in the discussion which can be reached using long-range tunneling. This requires the timing jitter of the tunneling from the (1,0,1)- to the (2,0,0)-region to be small compared to J. This condition can be satisfied by making the tunnel couplings sufficiently large. In that case, the contour lines in Fig. 5.10a indicate that for a fixed J, the Q's are similar for both the nearest-neighbour and superexchange region. This can be understood from the fact that in the far detuned regime, the energy splitting between the T_0 and S state (J) is linearly proportional to the detuning and the tunnel coupling has a negligible influence. We expect the nearest-neighbour and superexchange to show even better Q's when operating in the very far detuned regime inside (2,0,0), where the exchange is set by the orbital splitting and the sensitivity to charge noise is low [118]. In that regime we expect the nearest-neighbour and superexchange to have the same quality factor.

As a final observation we note that nearest-neighbour exchange can never fully be turned off and can at most be reduced to t^2/U with U the charging energy of the dot [13]. Superexchange can be set closer to zero however as δ can easily be made larger than U: this is beneficial to fully decouple qubits.

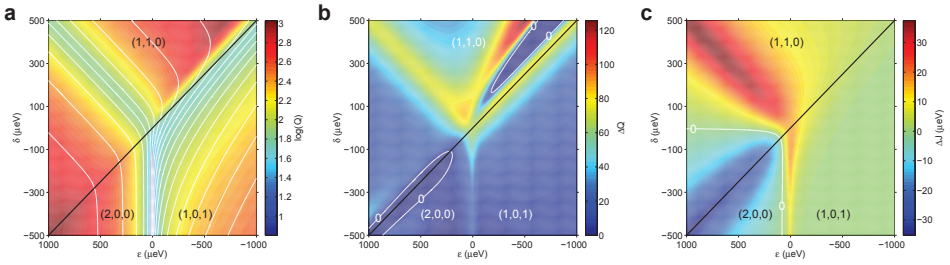

Figure 5.10: a Numerically approximated $\log(Q)$ of the exchange oscillations as a function of δ and ϵ for $t = 40$ μeV. White lines represent contour plots of fixed J for several different values of J. Black line denotes the transition between nearest-neighbour and superexchange. **b** Change in Q when t is doubled to $t = 80$ μeV: $\Delta Q = Q(t = 80) - Q(t = 40)$. White line represents contour plot of $\Delta Q = 0$. **c** Change in J when t is doubled to $t = 80$ μeV: $\Delta J = J(t = 80) - J(t = 40)$. White line represents contour plot of $\Delta J = 0$. The decrease in J in the (2,0,0)-region is caused by the increased anti-crossing between the $T_0(1,1,0)$- and $T_0(1,0,1)$-state.

6

COMPUTER-AUTOMATED TUNING OF SEMICONDUCTOR DOUBLE QUANTUM DOTS INTO THE SINGLE-ELECTRON REGIME

T.A. Baart, P.T. Eendebak, C. Reichl, W. Wegscheider and L.M.K. Vandersypen

We report the computer-automated tuning of gate-defined semiconductor double quantum dots in GaAs heterostructures. We benchmark the algorithm by creating three double quantum dots inside a linear array of four quantum dots. The algorithm sets the correct gate voltages for all the gates to tune the double quantum dots into the single-electron regime. The algorithm only requires (1) prior knowledge of the gate design and (2) the pinch-off value of the single gate T that is shared by all the quantum dots. This work significantly alleviates the user effort required to tune multiple quantum dot devices.

manuscript submitted, arXiv:1603.02274

6.1. INTRODUCTION

Electrostatically defined semiconductor quantum dots have been the focus of intense research for the application of solid-state quantum computing [26, 120, 121]. In this architecture, quantum bits (qubits) can be defined by the spin state of an electron. Recently, several experiments have shown coherent manipulation of such spins for the purpose of spin-based quantum computation [29, 42, 43, 119, 122–124]. Enabled by advances in device technology, the number of quantum dots that can be accessed is quickly increasing from very few to many [125, 126]. Up to date, all these quantum dots have been tuned by 'hand'. This is a slow process whereby gate voltages are tweaked carefully, first to reach a regime with one electron in each of the dots, and then to adjust the strength of all the tunnel barriers. Defects and variations in the local composition of the heterostructure lead to a disordered background potential landscape, which must be compensated for by the gate voltages. On top, cross-capacitances of each gate to neighboring dots increases the tuning complexity as the number of dots increases. The ability to tune these dots automated by computer algorithms, including tuning of many dots in parallel, is an important ingredient towards the scalability of this approach to create a large-scale quantum computer.

In this Letter, we demonstrate the computer automated tuning of double quantum dot (DQD) devices. We have created an algorithm that only requires as input: (1) prior knowledge of the gate design, which is reasonable for future large-scale quantum dot circuits and (2) the measured pinch-off value of the single gate T shared by all the quantum dots. We describe the algorithm used and verify its robustness by creating three independent DQDs inside a quadruple dot array. The algorithm finds the correct gate voltages to tune all DQDs into the single-electron regime and the computer recognizes that this goal has been achieved within an overnight measurement.

A scanning electron microscopy (SEM) image of a device nominally identical to the one used is shown in Fig. 6.1(a). Gate electrodes fabricated on the surface of a GaAs/AlGaAs heterostructure are biased with appropriate voltages to selectively deplete regions of the two-dimensional electron gas (2DEG) 90 nm below the surface and define the quantum dots. The main function of each gate is as follows: gates L and R set the tunnel coupling with the left and right reservoir, respectively. $D1-D3$ control the three inter-dot tunnel couplings and $P1-P4$ are used to set the electron number in each dot. However, each gate influences the other parameters as well. Changing L for example, will also change the electron number in dot 1 and influence the inter-dot tunnel barrier between dot 1 and 2. This needs to be taken into account by the algorithm. Two other nearby quantum dots on top of the qubit array, sensing dot 1 and 2 (SD1 and SD2), are created in a similar way and function as a capacitively coupled charge sensor of the dot array. When positioned on the flank of a Coulomb peak, the conductance through the sensing dot is very sensitive to the number of charges in each of the dots in the array. Changes in conductance are measured using radiofrequency (RF) reflectometry [75]. High-frequency lines are connected via bias-tees to gates $P1$, $P3$ and $P4$. The device was cooled inside a dilution refrigerator to a base temperature of ~15 mK. All measurements were taken at zero magnetic field.

Before running the algorithm the user is required to input a range of T-values for which the algorithm should try to find DQDs. This range is currently determined by

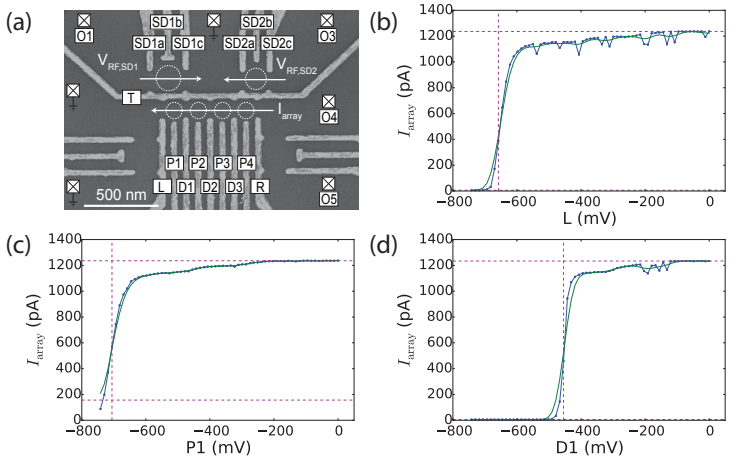

Figure 6.1: (a) SEM image of a sample nominally identical to the one used for the measurements. Dotted circles indicate quantum dots, squares indicate Fermi reservoirs in the 2DEG, which are connected to ohmic contacts. O5 is always open during the measurements. The gates that are not labeled are grounded. The current through the quadruple dot array, I_{array}, is measured to create single dots. The reflectance of the SDs, $V_{RF,SD1}$ and $V_{RF,SD2}$, is monitored to tune DQDs into the single-electron regime. (b-d) Pinch-off curves showing I_{array} versus the gate voltages L, $P1$ and $D1$ ($T = -400$ mV). The calculated transition value $V^{\text{tr}}_{\text{gate},i}$ is shown as a dotted vertical line. The horizontal lines denote the high and low value of the current as detected by the algorithm.

measuring the pinch-off value of T manually, and then choosing a set of gate voltages more negative than this pinch-off value. The pinch-off value can for example be determined by setting all other gates to 0 mV and next measuring the current from O1 to O4 (other ohmics open) whilst sweeping T. This step could be automated in future work.

6.2. THE ALGORITHM

The algorithm consists of 3 steps: (1) to determine the starting values for the gate voltages, we first measure the pinch-off characteristic between each individual gate and the shared T-gate. Based on those results we (2) create single quantum dots. The required tunnel barriers acquired in (2) can be used as a starting point to (3) create double dots into the single-electron regime. Subsequently, steps (1) and (2) are used to create the SDs.

To measure the pinch-off characteristic we apply a small voltage-bias (~ 500 μV) to O4 and measure the current I_{array} through the quadruple dot array. Variations in the local composition of the heterostructure underneath each gate will be reflected in the required voltage to create quantum point contacts (QPCs). We term this voltage the transition value, $V^{\text{tr}}_{\text{gate},i}$, which is defined as the gate voltage for which I_{array} is at $\sim 30\%$ of its maximum value (see Supplementary Information 6.6.2). This procedure is repeated for a range of T-values. Figs. 6.1(b-d) show an example for $T = -400$ mV and the gates controlling the leftmost dot (L, $P1$ and $D1$). In practice, it is best to continue with the most

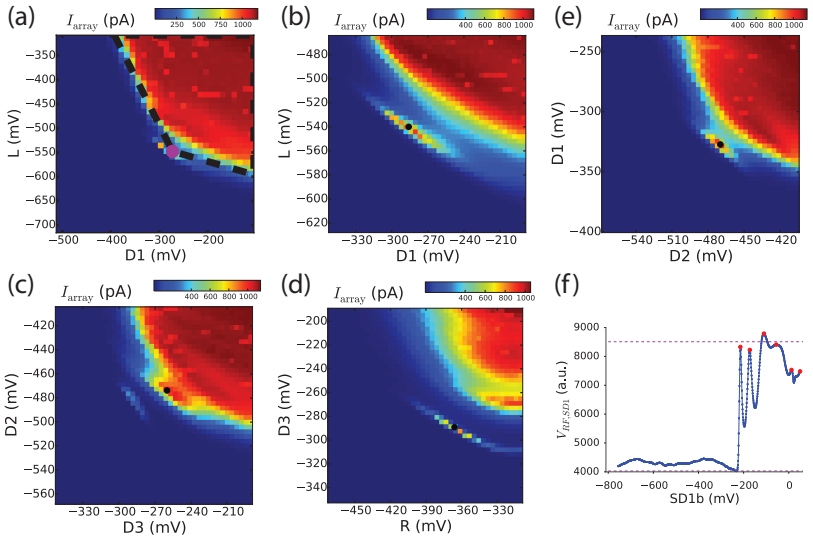

Figure 6.2: (a-e) Four single dots are created by sweeping the tunnel barrier gate voltages for each dot whilst keeping the plunger gate fixed and monitoring I_{array}. After a coarse scan (example shown for the leftmost dot in (a)) we zoom in to the region showing Coulomb blockade (b-e). The center location where Coulomb peaks are formed is determined using a Gabor filter and depicted by black dots. (f) The SD is fine-tuned by sweeping its plunger gate voltage. The charge sensing measurements shown in Fig. 6.3 are performed by tuning to the left flank of a Coulomb peak.

positive T-value that still allows pinch-off for all gates. In our experience this tends to create better quantum dots for this gate design.

6.3. CREATION OF SINGLE QUANTUM DOTS

We start by creating single quantum dots, as they already include much of the cross-talk between gates, dots and barriers, that is present in double dots. To create single quantum dots we apply a fixed voltage for the plunger gate (usually -80 mV) which we know is appropriate for this device design, and use the transition values of the barrier gates as input for a 2D coarse scan. A suitable scan range is [$V^{\mathrm{tr}}_{\mathrm{gate},i}$-10 mV, $V^{\mathrm{tr}}_{\mathrm{gate},i}$+400 mV]. We again monitor I_{array}. The structure of these scans is always similar: for negative gate voltages the channel is closed, so there is no current. For more positive voltages the channel is open, so there is a large current. We fit a tetragon to the area corresponding to large current, see Fig. 6.2(a) for an example of the leftmost dot (details can be found in Supplementary Information 6.6.2). We next take a finer scan of the area closest to the tetragon corner with the most negative gate voltages, see Figs. 6.2(b-e). In the experiments we have performed, this point is always showing the start of quantum dot formation through the appearance of a Coulomb peak. We use this point as the starting point in gate-space for creating DQDs. The exact location of the Coulomb peak is determined using a Gabor filter and is shown as black dots in Figs. 6.2(b-e) (see Supplementary Information 6.6.2).

6.4. CREATION OF DOUBLE QUANTUM DOTS

When going to double dots, transport measurements are not suitable as current levels through few-electron double dots are impractically low for this device design. Therefore, once the single dots have been formed, we tune the SDs in a similar way. They can then be used for non-invasive charge sensing which does allow one to distinguish single-electron transitions in the dot array through RF-reflectometry. To achieve a high sensitivity it is important that the SD is tuned to the flank of one of its Coulomb peaks. After finding a Coulomb peak for the SD in a similar way as described for the qubit dots, we make a 1D scan of the plunger gates, see Fig. 6.2(f). Each detected Coulomb peak is given a score based on its height and slope that allows the algorithm to continue with the most sensitive operating point for the corresponding plunger gate (see Supplementary Information 6.6.2).

With the SD tuned we create a double dot in the following way: first we set the voltages of the gates for the double dot to the values found for the individual single dots (black dots in Figs. 6.2(b-e)). For the single gate shared by the two individual dots (e.g. gate $D1$ for the leftmost double dot) the average of the two values is used. Next, we record a charge stability diagram of the double dot structure by varying the two plunger gate voltages involved. We use a heuristic formula to determine the correct scan range that takes into account the capacitive coupling of the gates to the dots (see Supplementary Information 6.6.2). Typical results for such scans are shown in Fig. 6.3(a-c). Scans involving two plungers are measured by applying a triangular voltage ramp to the plungers on the horizontal axis using an arbitrary waveform generator, and by stepping the other plunger gate using DACs [117]. Whilst stepping the latter gate we also adjust the sensing dot plunger gate to compensate for cross-capacitive coupling and thereby improve the operating range of the SD.

To verify that the double dot has reached the single-electron regime, the algorithm first detects how well specific parts of the charge stability diagrams match the shape of a reference cross (see inset of Fig. 6.3). Each match should ideally correspond to the crossing of a charging line from each dot. The shape of the reference cross is derived from the various capacitive couplings, which follow from the gate design and are known approximately from the start. Instead of detecting crosses, one could also try to detect the individual charge-transition lines. This turned out to be more sensitive to errors for two reasons: (1) Extra features in the charge stability diagrams that do not correspond to charging lines are wrongfully interpreted as dot features. (2) Not all charging lines are straight across the entire dataset; this makes it harder to interpret which line belongs to which dot. The cross-matching algorithm is robust against such anomalies because of the local, instead of global, search across the dataset. In future work it could actually be useful to still detect these extra and/or curved lines. They could give information about e.g. unwanted additional dots and aid in determining the electron numbers in regions with higher tunnel couplings. For the current goal of finding the single-electron regime this extra information is not required.

Next, the algorithm checks whether within a region slightly larger than 70×70 mV^2, it finds other charge transitions for more negative gate voltages with respect to the most bottom-left detected cross. If this region is too small to draw a conclusion, the algorithm will adjust the scan range to more negative voltages (see Supplementary Informa-

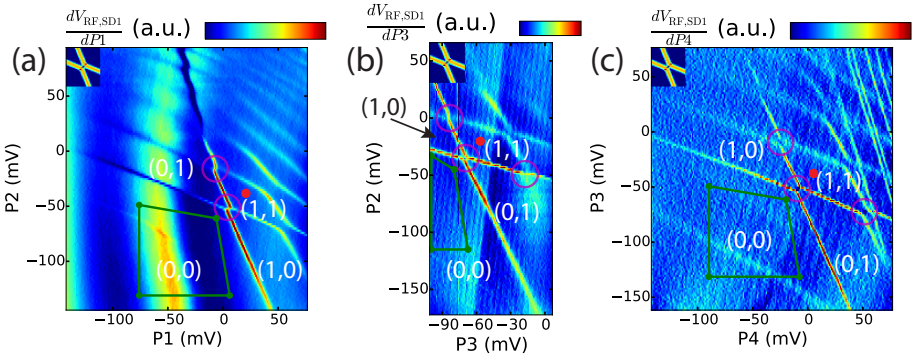

Figure 6.3: (a-c) Double dot charge stability diagram for the left, middle and right double dot respectively. Using the result of Figs. 6.2(b-e) the tunnel barriers are set, and the plunger gates are swept as indicated. The occupancy of each dot is denoted by (n, m) corresponding to the number of electrons in the left and right dot respectively of that specific double dot. The algorithm determines how well regions of the charge stability diagram match to a reference cross (see inset). Good matches are encircled. These are interpreted as crossings of charging lines from two dots. The single-electron regime is found by verifying that no other prominent charging lines are observed for more negative gate voltages with respect to the most bottom-left detected cross (green regions). The extra features present in (a) and (c) were below the detection threshold and are attributed to additional dots due to a lack of coupling with the double dot under investigation (a) or a different slope (c). These unwanted dots do not necessarily pose a problem for follow-up double dot experiments. The horizontal scan range of panel (b) is less than for (a) and (c) due to hardware limitations.

tion 6.6.2). The regions are depicted by the green tetragons in Fig. 6.3. If no extra transitions are detected: the single-electron regime has been found and the result is given a score of 1 for that specific measurement outcome. If extra transitions are found, the algorithm outputs the score 0. For a score of 1, the algorithm can set both plunger voltages to +15 mV with respect to the most bottom-left detected cross to enter the single-electron regime (depicted by red dots in Fig. 6.3). This is where the algorithm stops. At the end of the run the user can see the measurement results for the various initial choices of T and select the best one.

6.5. DISCUSSION

All combined, the running of this complete algorithm (for a single value of the T-gate) takes ~200 minutes (see Supplementary Information 6.6.2). Per device typically 5 T-values are tested. In practice we have observed that for some cooldowns of the sample the algorithm could not attain the single-electron regime. A thermal cycle combined with different bias cooling [85] can significantly influence the tuning and solve this issue; just as for tuning done by hand. The key difference is that with the computer-aided tuning hardly any user effort is required to explore tuning of double dots to the few-electron regime. In future work the time required for automated tuning (as well as for tuning by hand) can be further reduced by also connecting the tunnel barrier gates of each single dot to a high-frequency line which would allow much faster scans for Figs. 6.1-6.2 [127]. These scans currently form the bottleneck in the overall tuning process. Future experiments will also address the automated tuning of more than two dots and the tuning of

the tunnel couplings in between dots and their reservoirs, which are key parameters for operating dots as qubit devices.

In summary, we have demonstrated computer-automated tuning of double quantum dot devices into the single-electron regime. This work will simplify tuning dots in the future and forms the first step towards automated tuning of large arrays of quantum dots.

6.6. SUPPLEMENTARY INFORMATION

6.6.1. METHODS AND MATERIALS

The experiment was performed on a GaAs/$Al_{0.307}Ga_{0.693}As$ heterostructure grown by molecular-beam epitaxy, with a 90-nm-deep 2DEG with an electron density of $2.2 \cdot 10^{11}$ cm^{-2} and mobility of $3.4 \cdot 10^{6}$ cm^{2}V^{-1}s^{-1} (measured at 1.3 K). The metallic (Ti-Au) surface gates were fabricated using electron-beam lithography. The device was cooled inside an Oxford Triton 400 dilution refrigerator to a base temperature of 15 mK. To reduce charge noise the sample was cooled while applying a positive voltage on all gates (ranging between 100 and 400 mV) [85]. Gates $P1$, $P3$ and $P4$ were connected to home-built bias-tees (RC = 470 ms), enabling application of d.c. voltage bias as well as high-frequency voltage excitation to these gates. Frequency multiplexing combined with RF reflectometry of the SDs was performed using two LC circuits matching a carrier wave of frequency 107.1 MHz for SD1 and 86.4 MHz for SD2. The inductors are formed by micro-fabricated NbTiN superconducting spiral inductors with an inductance of 3.2 μH (SD1) and 4.6 μH (SD2). The power of the carrier wave arriving at the sample was estimated to be -93 dBm. The reflected signal was amplified using a cryogenic Weinreb CITLF2 amplifier and subsequently demodulated using homebuilt electronics. Data acquisition was performed using a FPGA (DE0-Nano Terasic) and digital multimeters (Keithley). Voltage pulses to the gates were applied using a Tektronix AWG5014.

6.6.2. SOFTWARE AND ALGORITHMS

The software was developed using Python [128] with SciPy [129].

The image processing is performed in pixel coordinates. We specify the parameters of algorithms in physical units such as mV. The corresponding parameter in pixel units is then determined by translating the value using the scan parameters. By specifying the parameters in physical units the algorithms remain valid if we make scans with a different resolution. Of course making scans with a different resolution can lead to differences in rounding of numbers leading to slightly different results.

DETERMINATION OF THE TRANSITION VALUES $V^{tr}_{gate,i}$

To determine the transition-voltage values $V^{tr}_{gate,i}$ we perform the following steps:

- Determine the lowvalue (L) and highvalue (H) of current of the scan by taking a robust minimum and maximum. For L this is done by taking the 1^{th} percentile of the values. H is determined by first taking the 90^{th} percentile of the scan data H_0 and then the 90^{th} percentile of all the values larger then $(L + H_0)/2$. This two-stage process to determine H also works well when for example the pinch-off occurs for

very positive gate voltages. Simply taking for example the 99$^{\text{th}}$ percentile of the scan data could then result in a too low estimate.

- Smoothen the signal and find the first element in the scan whose current value is larger than $.7L + .3H$. The corresponding gate voltage for that current value is selected as the transition value $V^{tr}_{gate,i}$.

- Perform several additional checks. The above two steps will always results in a transition value, even though the channel could be completely open or closed. The checks include amongst others:

  – If the transition value is near the left border of the scan we conclude the transition has not been reached. We then set the transition value to the lowest value of the gate that has been scanned. In principle the algorithm could continue to search for a transition value for more negative gate voltages. However, making gate voltages too negative may induce charge noise in the sample so we do not want to apply very negative voltages. Choosing the most negative voltage of the scan range then turns out to be a good choice. In the next steps of the algorithm, this transition voltage is just a starting value and the gate voltage will still be varied. Due to cross-talk, the neighboring gates in follow-up steps will together with the gate that did not yet close, typically still ensure the formation of single dots.

  – The difference of the mean of the measured current values left of the transition value and the mean of the current values right of the transition value should be large enough. Large enough means more than 0.3 times the standard deviation of all the current values in the scan. If it is not large enough, we set the transition value to the lowest value of the gate that has been scanned following a similar reasoning as for the previous check. In this scenario we assume that the scan range started at a voltage around 0 mV, and thus that no significant change in the measured current corresponds to a channel that was always open.

ANALYSIS OF SINGLE DOTS

As described in the main text the initial analysis of a 2D scan is performed by fitting a tetragon to the image. The tetragon is fitted by maximizing a cost function that measures how well the tetragon fits to the region with high current. First an adaptive threshold is calculated to determine the values of high and low current. The cost function is then defined by the number of pixels within the tetragon with high current, minus the number of pixels outside the tetragon with low current. The optimization is performed with the Nelder-Mead algorithm under the constraint that the tetragon is contained within the image. The bottom-left corner point of the tetragon gives a good indication of the position of the area where Coulomb peaks are visible. See the magenta points in Figs. 6.4(a-d).

The next step is to make a more detailed scan of the area. In this scan we search for the Coulomb peaks using a Gabor filter [130, 131]. A Gabor filter is a sinusoidal wave

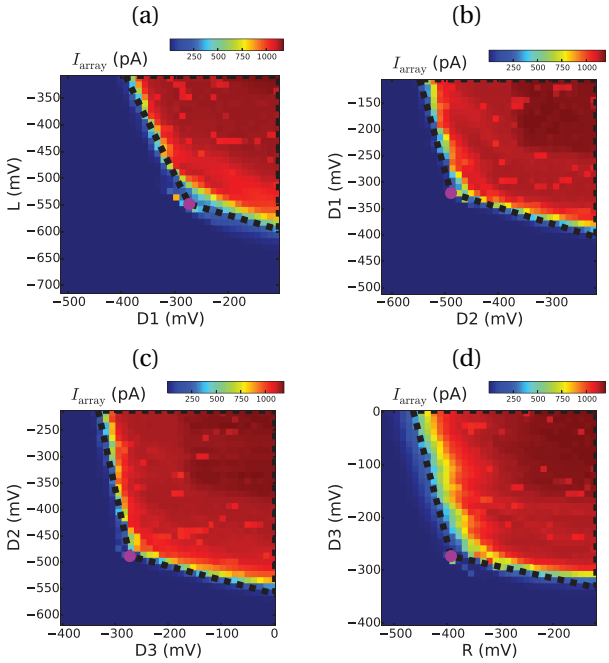

Figure 6.4: (a-d) Four single dots are created by sweeping the tunnel barriers for each dot whilst keeping the plunger fixed. The outcome is fitted to a tetragon (dashed black lines) to find the best gate values to search for Coulomb peak formation.

multiplied by a Gaussian function. The sinusoidal wave seeks out features that show contrast with their environment. We define

$$G(x,y,\lambda,\theta,\psi,\sigma,\gamma) = \exp\left(-\frac{x'^2+\gamma^2 y'^2}{2\sigma^2}\right)\cos(2\pi x'/\lambda+\psi) \tag{6.1}$$

with $x' = \cos(\theta)x + \sin(\theta)y$, $y' = -\sin(\theta)x + \cos(\theta)y$. We create a Gabor filter with the following parameters: The orientation is set to $\theta = \pi/4$, standard deviation of Gaussian $\sigma = 12.5$ mV, $\gamma = 1$, $\lambda = 10$ mV, $\psi = 0$. A rectangular image patch of size 40×40 mV^2 is created using this Gabor function (see inset Fig. 6.5).

The response of the Gabor filter to the 2D scan of Fig. 6.5 is shown in Fig. 6.6.[1] From the response figure it is clear that there is a peak (red color) at the location of the Coulomb peak. To extract the precise location of the peaks we threshold the image with a value automatically determined from the response image and determine the connected components, i.e. the pixels that together constitute a relevant feature. The center of the component furthest into the direction of the closed region is selected as the best Coulomb peak (green point). The concept of connected components for a binary image is standard in the computer vision community. We find these using OpenCv, see `http://docs.`

[1] We use the OpenCV function `matchTemplate` with method `TM_CCORR_NORMED`.

opencv.org/3.0.0/d0/d7a/classcv_1_1SimpleBlobDetector.html, but any implementation will return the same results. If there are more than two Coulomb peaks there are two possibilities:

1. Both peaks are converted into two separate connected components. Then, the blob furthest into the direction of the closed region of the scan is selected.

2. One of the two peaks might be much stronger than the other. In that case the other peak is below the threshold selected by the algorithm and the other peak will be not be visible.

In our experiments we observed that for the single dots at most a couple of Coulomb peaks are visible. Scans of the region of Fig. 6.5 with a charge sensor instead of the current through the array confirm that the last Coulomb peak visible in the image is indeed the Coulomb peak corresponding to the zero-to-one electron transition. This behavior is typical for this specific gate design and influences the choice for the plunger gate values for the DQD scans such as shown in Fig. 6.3 of the main text to find the single-electron regime, see also section 6.6.2.

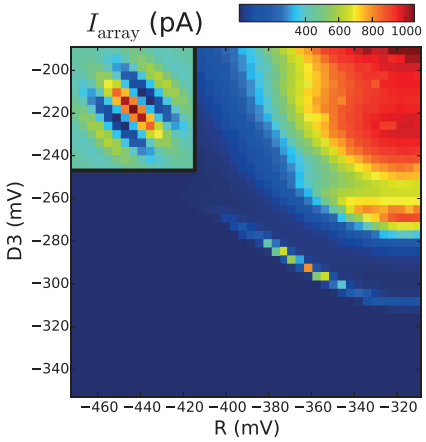

Figure 6.5: Scan of the rightmost single dot where the tunnel barriers are varied. The inset depicts the Gabor filter used to determine the location where Coulomb peaks are formed, see Fig. 6.6 for the filter response.

SELECTION OF COULOMB PEAKS

In this section we describe how the selection of Coulomb peaks for the SD is performed. We start with a scan of the plunger gate $SDxb$ (x is 1 or 2) in a configuration for which Coulomb peaks can be expected. In the scan we determine the lowest and highest values (meaning the channel is completely closed or completely open) using a robust minimum and maximum function (see section 6.6.2 for details). These values are indicated as dotted horizontal lines in Fig. 6.7.

The peaks in the data are detected by selecting the local maxima in the plot. All peaks below a minimum threshold are discarded.[2] For each of the peaks the position of the

[2] We use `scipy.ndimage.filters.maximum_filter1d` with a size parameter of 12 mV.

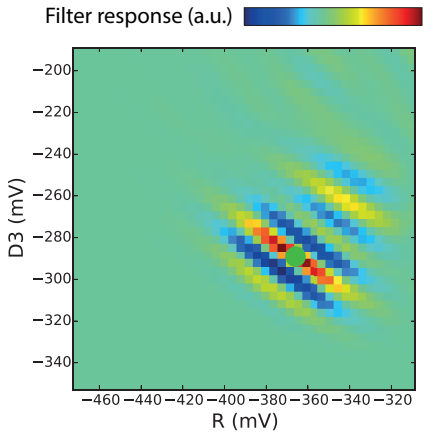

Figure 6.6: Response of the Gabor filter for the data shown in Fig. 6.5. Green point is selected as the best Coulomb peak.

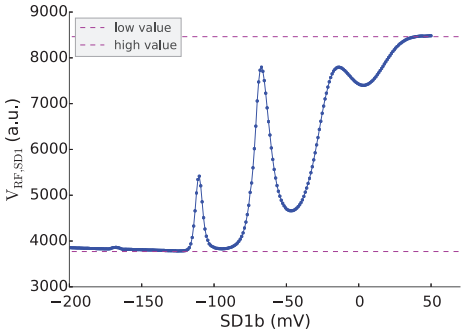

Figure 6.7: Scan of the reflectance $V_{\mathrm{RF,SD1}}$ for varying plunger gate $SD1b$.

peak half-height on the left and right side is determined. Also the bottom of the peak is determined (see details at the end of this section). From these values we can determine the peak properties such as the height and the half-width of the peak. Finally the peaks are filtered based on the peak height and overlapping peaks are removed (see details at the end of this section) leading to the detected peaks shown in Fig. 6.8.

After this filtering step the peaks are ordered according to a score. For various applications we can define different scores. In this work the SD-peaks are primarily selected for proper charge sensing. For a good charge sensitivity we need a large peak with a steep slope. We then tune the SD to the position at half-height on the left of the highest-scoring peak. The scoring function we used is

$$\text{score} = \text{height}\frac{2}{1+\text{hw}/\text{hw}_0} \tag{6.2}$$

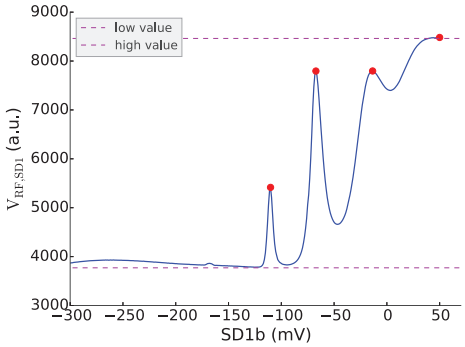

Figure 6.8: Detected peaks in the data of Fig. 6.7.

The value of hw_0 is a scaling parameter determining the typical half width of a Coulomb peak. In our experiments we used $hw_0 = 10$ mV. In our experience, this scoring represents a reasonable trade-off between the height and the slope of a peak. The result is shown in Fig. 6.9.

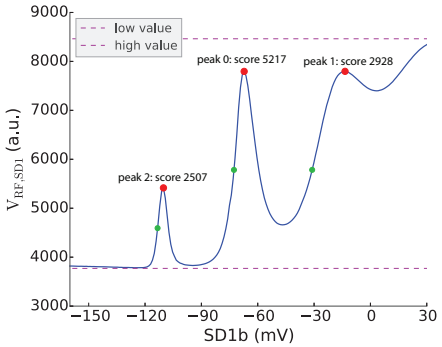

Figure 6.9: Final result of indexing the data from Fig. 6.7. The peaks are plotted in red, the point at the peak half-height on the left is plotted as a green dot.

Details to detect the bottom left of a peak: the x-coordinate of a peak, x_{peak}, has already been determined by selecting the local maxima in the data. To find the x-coordinate of the bottom on the left side of the peak, l, the following steps are performed after smoothing the data:

1. Search for the x-coordinate, $x_{\text{bottom low}}$, of the minimum value (bottom low) in the range $[x_{\text{peak}} - 3 \times thw, x_{\text{peak}}]$. The variable thw is a measure for the typical half width of a peak and is set to ~ 10 mV.

2. Starting from $x_{\text{bottom low}}$, scan from left to right and select the first datapoint that

Gate	Left dot	Right dot	Double-dot
L	-539.9		-539.9
$P1$	-80.0		-33.0
$D1$	-285.9	-327.3	-306.6
$P2$		-80.0	-26.0
$D2$		-469.7	-469.7

Table 6.1: Example for double dot settings. All values are in mV.

fulfills the following two conditions: (1) the slope is positive, and (2) the y-value is larger than 'bottom low + 10% of the peak height'.

This method does not require a specific fitting model, and also works well for asymmetric Coulomb peaks.

Details of the filter to remove overlapping peaks: for each peak we have the position of the bottom on the left (l) and the top of the peak (p). For two peaks the overlap is defined using the intersection of the intervals $[l_1, p_1]$ and $[l_2, p_2]$: $\pi([l_1, p_1], [l_2, p_2])$. The length of an interval L is denoted as $||L||$. The overlap ratio is then equal to $||\pi([l_1, p_1], [l_2, p_2])|| / \sqrt{||[l_1, p_1]|| ||[l_2, p_2]||}$. To make the overlap a bit more robust we use a smoothed version of this formula using Laplace smoothing:

$$s = \frac{1 \text{ mV} + ||\pi([l_1, p_1], [l_2, p_2])||}{1 \text{ mV} + \sqrt{||[l_1, p_1]|| ||[l_2, p_2]||}}. \tag{6.3}$$

When the overlap s between two peaks is larger than a threshold (0.6), then the peak with the lowest score is removed.

TUNING AND ANALYSIS OF A DOUBLE DOT

The main text describes how we set the gate values for the tunnel barriers of each double dot using the information of the single dot scans. For the plunger gates of the double dot an extra compensation factor is added. When each single dot is formed, the dot-barrier gate of its neighbor is kept at zero Volt. When next making a double dot, these dot-barrier gates are activated and shift the electrochemical potential of their neighbor, for which we compensate with the corresponding plunger voltage. This compensation factor is determined heuristically. For a double dot with gates $L - P1 - M - P2 - R$ the compensation values for $P1, P2$ are

$$\left(-\phi R, -\phi L\right), \tag{6.4}$$

with $\phi = 0.1$. See Table 6.1 for an example. In future experiments we plan to use the capacitive-coupling information from the single dot scans in order to create more precise compensation values for the tunnel barrier gates. The exact values of the plunger gates are not very important, since we will make a scan of the double dot using the plunger gates. A good initial guess does reduce the measurement time.

The important structures in the scan of a double dot are the charging lines and the crossings of two charging lines. To determine the locations of the crossings in the image

we create a template for such a crossing. We then search for crossings using template matching. The response to the template is thresholded and local maxima are calculated. The template of the crossing consists of 4 lines at angles $\pi/8$, $3\pi/8$, $9\pi/8$ and $11\pi/8$ (radians) that are separated by a distance of 1.5 mV at 45 degrees that represents the interdot capacitive coupling (see inset of Fig. 6.3 of the main text). The width of these lines ensures that experimentally measured crossings still overlap with the template despite unavoidable small variations in the interdot capacitive coupling and the lever arms between gate voltage and electrochemical potential, which affect the slope of the transitions.

The final step consists of checking whether extra charging lines are visible in a region of ~70×70 mV^2 to the side of more negative gate voltages. The size of this region should be larger than the charging energy of each dot in mV. The topright corner of the 70×70 mV^2 area is located -10 mV southwest of the most bottom-left cross. We slightly extend this region on top and on the right to reduce the probability that a charging line is missed. If the total region falls outside the scan range of the data, the algorithm reduces the size of this region accordingly. The algorithm could then draw the wrong conclusion. When the region that results from clipping at the border of the scan range is smaller than 40×40 mV^2, the algorithm will adjust the scan range to more negative voltages. The location of the most-bottom-left detected cross will be moved to the coordinates (2/3, 2/3) of the total scan range. An example is shown in Fig. 6.10. The algorithm will then repeat itself starting with template matching of crossings.

In the case that the region is large enough, we first smoothen the data within this region. We subtract the smoothed data from the original data and check whether the resulting pixel values fall above a certain threshold that is proportional to the standard deviation of the smoothed dataset. The algorithm classifies the dataset as 'single-electron regime' if at most a few pixel values are larger than the threshold. The precise number of allowed pixel values above the threshold is proportional to the scan resolution.

TIME REQUIRED TO RUN THE ALGORITHM

As mentioned in the main text the data acquisition time for Figs. 6.1-6.2 forms the bottle neck in the overall tuning process. Table 6.2 gives an overview of the data acquisition time per step of the algorithm. The overall data analysis takes less than 10 minutes and does not form the limiting step. The algorithm always goes through each of the three steps.

Step nr. of algorithm	Data acquisition time [min]
(1)	15.7
(2)	179.6
(3)	13.6

Table 6.2: Data acquisition time per step of the algorithm.

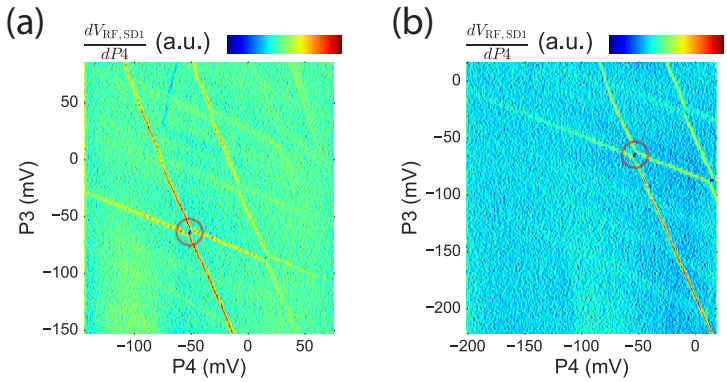

Figure 6.10: Example where the scan range for rightmost double dot is adjusted such that the originally most bottom-left detected cross (a) is moved to (2/3, 2/3) of the total scan range (b). For this example we forced the algorithm to rescan, even though the region to the bottom-left of the cross was already sufficiently large. So far we did not yet observe results where this rescan was strictly required. We did already incorporate this feature in the algorithm in case the first guess for the scan range is not sufficient to determine if the single-electron regime has been reached. The data in this scan is different compared to the results shown in Fig. 6.3 of the main text due to a thermal cycle of the sample.

7

NANOSECOND-TIMESCALE SPIN TRANSFER USING INDIVIDUAL ELECTRONS IN A QUADRUPLE-QUANTUM-DOT DEVICE

T.A. Baart, N. Jovanovic, C. Reichl, W. Wegscheider and L.M.K. Vandersypen

The ability to coherently transport electron-spin states between different sites of gate-defined semiconductor quantum dots is an essential ingredient for a quantum-dot-based quantum computer. Previous shuttles using electrostatic gating were too slow to move an electron within the spin dephasing time across an array. Here we report a nanosecond-timescale spin transfer of individual electrons across a quadruple-quantum-dot device. Limited by the relaxation time of a 'hot spot' we conclude that the shuttle takes at most 150 ns but could well have been faster. 150 ns is fast enough to preserve the phase for spin quantum bits in e.g. Si or Si/SiGe. This work therefore forms an important step towards demonstrating coherent spin transfer.

manuscript in preparation

7.1. INTRODUCTION

Electrostatically defined semiconductor quantum dots have been the focus of intense research for the application of solid-state quantum computing [26, 120, 121]. In this architecture, quantum bits (qubits) can be defined by the spin state of an electron. Recently, several experiments have shown coherent manipulation of such spins for the purpose of spin-based quantum computation [29, 42, 43, 119, 122]. Enabled by advances in device technology, the number of quantum dots that can be accessed is quickly increasing from very few to many [125, 126]. Large-scale quantum computing architectures require that qubits can be moved around in the course of a quantum computation [64, 84]. Several approaches have been demonstrated to transfer electrons between different sites, e.g.: using surface acoustic waves [132] or electrostatic gates [117] (see Chapter 4). First evidence has been shown that the spin projection is preserved during such a shuttle. It still remains to be demonstrated however that a coherent superposition is also preserved during shuttling, an essential requirement for a quantum computer.

In this work we will focus on the approach using electrostatic gates as it has proven to provide high-fidelity spin transfer [117]. We use a linear array of 4 quantum dots which is currently the state-of-the-art in system size for GaAs/AlGaAs heterostructures. So far, it has been challenging to create high tunnel couplings between neighbouring dots, whilst keeping sufficient coupling with nearby reservoirs to load spin states and perform the spin read-out using spin-to-charge conversion [47]. In the most recent example of a shuttle [117], the inter-dot tunnel couplings were below 1 GHz making it impossible to shuttle on the nanosecond-timescale. Given the rapid dephasing time, T_2^*, of ~20 ns (in GaAs), such high-speed shuttles are essential to perform a coherent spin transfer. In general, short shuttle times will be beneficial.

In this Letter, we demonstrate the fast transfer of an electron-spin state inside a quadruple-quantum-dot device with high inter-dot-tunnel couplings (>2.5 GHz). Measurements indicate that programming a pulse sequence to shuttle the electron within 3 ns from the leftmost to the rightmost dot works with high spin-transfer fidelity. We cannot give definitive evidence that the electron actually shuttled within 3 ns, but can measure an *upper* bound of 150 ns. Although 150 ns is too slow for GaAs devices, this approach can be mapped onto Si and/or Si/SiGe structures where the dephasing time has been measured to be much longer >120 μs [42]. It still has to be shown that such structures can reach high tunnel couplings, although first steps have recently been made in a triple-quantum-dot device [133]. The work presented here therefore forms an important step towards demonstrating a coherent spin transfer.

A scanning electron microscopy (SEM) image of a device nominally identical to the one used is shown in the inset of Fig. 7.1(a). Gate electrodes fabricated on the surface of a GaAs/AlGaAs heterostructure are biased with appropriate voltages to selectively deplete regions of the two-dimensional electron gas (2DEG) 90 nm below the surface and define the quantum dots. The main function of each gate is as follows: gates L and R set the tunnel coupling with the left and right reservoir, respectively. $D1-D3$ control the three inter-dot tunnel couplings and $P1-P4$ are used to set the electron number in each dot. The inter-dot tunnel couplings have each been tuned to above 2.5 GHz (see Supplementary Information 7.5.3). We label the dots nrs. $1-4$ starting from left (nr. 1) to right (nr. 4). A nearby quantum dot on top of the qubit array, sensing dot (SD2), is created in a

similar way and functions as a capacitively coupled charge sensor of the dot array. When positioned on the flank of a Coulomb peak, the conductance through the sensing dot is very sensitive to the number of charges in each of the dots in the array. Changes in conductance are measured using radiofrequency (RF) reflectometry [75]. High-frequency lines are connected via bias-tees to gates $P1$, $P3$ and $P4$. The device was cooled inside a dilution refrigerator to a base temperature of ~22 mK. An in-plane magnetic field B_{ext} = 3.5 T was applied to split the spin-up (↑) and spin-down (↓) of the electron by the Zeeman energy ($E_z \approx 87\ \mu$eV), defining a qubit.

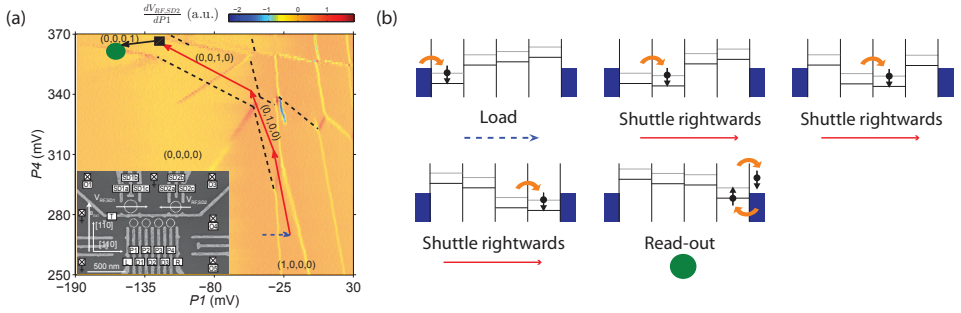

Figure 7.1: (a) Charge stability diagram of the quadruple dot. The occupancy of each dot is denoted by (l, m, n, p) corresponding to the number of electrons in dot 1 (leftmost), 2, 3 and 4 (rightmost) respectively. The fading of charge transition lines from dot 2 and 3 can be explained in a similar way as in Ref. 23 (black dotted lines indicate their positions) and becomes less prominent for a slow scan (see Supplementary Information 7.5.2). The pulse sequence for loading and read-out is indicated in the charge stability diagram via arrows, see also panel b. The black rectangle corresponds to the hot spot in dot 4 where spins relax on a sub-microsecond timescale; this hot spot is only used for the measurements of Fig. 7.3. Inset: SEM image of a sample nominally identical to the one used for the measurements. Dotted circles indicate quantum dots, squares indicate Fermi reservoirs in the 2DEG, which are connected to ohmic contacts. The gates that are not labeled are grounded. The reflectance of SD2, $V_{RF,SD2}$, is monitored. (b) Read from left to right and top to bottom. The system is initialized by loading one electron from the left reservoir. Next, we shuttle the electron to dot 2, 3 and 4 sequentially and finally read out the spin state using spin-selective tunneling.

7.2. OPERATING THE HIGH-SPEED SHUTTLE

The spin shuttle was initialized by loading a random electron-spin from the left reservoir into dot 1, as described by the schematic diagrams of Fig. 7.1(b) and implemented by the pulse sequence depicted by the arrows in Fig. 7.1(a). The loading of a random electron typically results in a spin mixture of ~35% spin-↓ and 65% spin-↑ [134]. Next, we quickly change the electrochemical potential of dot 1 and 2 in such a way that the electron will shuttle to dot 2. This is repeated for dot 2 to 3, and finally for dot 3 to 4 following the red arrows of Fig. 7.1(a). Once the electron spin has reached dot 4, the electrochemical potential of dot 4 is tuned to the position of the green circle in Fig. 7.1(a). At this position an excited spin-↓ was allowed to tunnel to the reservoir, while a ground-state spin-↑ would remain in the dot. The nearby sensing dot (SD2) was then used to record whether or not the electron had tunneled out, thereby revealing its spin state [47].

The operation of the spin shuttle was tested by performing a variety of measurements. The first two consist of introducing an extra variable waiting time inside either

dot 1 or dot 4 which induces spin relaxation to the ground state spin-↑. We will test if this is reflected in the measurement statistics. For the data represented by the blue curve in Fig. 7.2, we first load a random electron-spin in dot 1 for 10 μs, next shuttle to dot 2 in 1 ns, then to dot 3 in 1 ns, afterwards to dot 4 in 97 ns resulting in a total shuttle time of 99 ns and add an extra waiting stage in dot 4. Finally the read-out occurs which takes 320 μs. The data shows an expected exponential decay in the measured fraction of spin-↓ of the form $P(\downarrow) = p \cdot e^{\frac{-t}{T_1^j}} + \alpha^j$, where p is proportional to the initial loading probability of a spin-↓, T_1^j the relaxation time in dot j and α^j an offset. We observe $T_1^4 = 3.7$ (3.1, 4.4) ms and $\alpha^4 = 0.012$ (0.00, 0.025) (values in between brackets indicate 95% confidence interval).

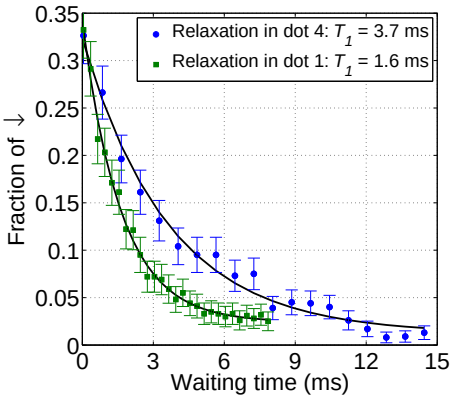

Figure 7.2: A random electron-spin is loaded inside dot 1. Afterwards the spin is either allowed to relax inside dot 1 (green trace) and next shuttled to dot 4 within 3 ns where the spin is read out. Or, the electron is directly shuttled from dot 1 to 4 within 99 ns, and relaxation is induced inside dot 4 after which it is read out (blue trace). Each datapoint is an average of 999 measurements (error bars two s.d.). Solid lines indicate an exponential fit to the data of the form $P(\downarrow) = p \cdot e^{\frac{-t}{T_1}} + \alpha$.

For the data represented by the green curve in Fig. 7.2 we perform a similar pulse sequence as before, only this time we add the extra waiting stage in dot 1 instead of dot 4. Also, the shuttling time from dot 3 to dot 4 is shortened to 1 ns giving a total shuttling time of 3 ns which is close to the fastest pulse that can be applied by the used pulse generator. We observe $T_1^1 = 1.6$ (1.5, 1.8) ms and $\alpha^1 = 0.024$ (0.019, 0.030).

For the T_1 measurement in dot 4, α^4 corresponds to '1 minus the spin-↑ read-out fidelity', assuming perfect spin-↑ initialization [117]. α^1 describes the probability to measure a spin-↓ in dot 4, after having created a spin-↑ in dot 1 by waiting infinitely long. The read-out fidelity does not depend on in which dot the T_1 process is induced, or on the shuttling time from dot 1 to 4. As a consequence, the value of α^1 can be used to determine if spin flips have occurred as a spin-↑ from dot 1 is shuttled to dot 4. Such spin flips could originate from (1) charge exchange with the reservoirs, (2) spin-orbit (SO) interaction and (3) hyperfine interaction with the nuclear spins of the quantum-dot host material. A detailed discussion is given in Ref. 117. If α^1 is larger than α^4, this would indicate spin flips. We observe here that $\alpha^1 = 0.024$ (0.019, 0.030) and $\alpha^4 = 0.012$ (0.00, 0.025).

This allows us to conclude that within the measurement uncertainty, shuttling a spin-↑ from dot 1 to dot 4 for this pulse sequence does not significantly affect the spin state.

The measurements so far strongly indicate that we have good control over where the electron spin resides (different T_1's), and that no spin-flips are induced even when shuttling at high speed throughout the array (similar α's). However, due to the relatively long read-out time of 320 μs it was still possible that even though we *programmed* a pulse sequence that should correspond to a shuttle time of 3 ns from dot 1 to 4, the electron actually remained for a longer time in one the dot(s) $1-3$ and only eventually shuttled to dot 4 somewhere during the read-out stage. During such an event, the electron lagging behind would temporarily be in a dot whose electrochemical potential is *above* the Fermi-level of the reservoirs and has sufficient energy to potentially leave the dot array. If it leaves, a new random electron will enter the array which would be detrimental for the shuttle-functionality. Alternatively, the electron stays within the array and continues the shuttle to end up in dot 4.

7.3. MEASURING AN UPPER-BOUND FOR THE SHUTTLING TIME

To gain more insight in when the electron actually arrives in dot 4, we added an extra stage to the pulse sequence that corresponds to a so-called 'hot spot' in dot 4. At the location of this hot spot, spin-orbit and hyperfine interactions rapidly mix the spin and orbital excited states '↓ $(0,0,0,1)$' and '↑ $(0,0,1,0)$'. Spin-conserving orbital relaxation rapidly transfers the state '↑ $(0,0,1,0)$' to '↑ $(0,0,0,1)$'. As a result, the '↓ $(0,0,0,1)$' state will relax on a sub-microsecond timescale to the state '↑ $(0,0,0,1)$' [81]. We will now use a similar pulse sequence as before, only with the inclusion of the hot spot inside dot 4. If the electron spin indeed follows the prescribed pulse sequence, it will hit the hot spot and relax. If the electron however resides for some more time in dot $1-3$, it will afterwards miss the hot spot and will still show a significant spin-↓ fraction. To identify the location of the hot spots we again load a random electron-spin in dot 1, pulse to dot 2 in 1 ns, then to dot 3 in 1 ns and next to a varying location along the inter-dot transition of dot 3 and 4 for 500 ns; the result is shown in Fig. 7.3(a). This clearly shows two prominent locations where the spin has completely relaxed. The dip at $P_1 \approx -121$ mV corresponds to the hot spot in dot 4, and is depicted by a black rectangle in Fig. 7.1(a). The other dip ($P_1 \approx -115$ mV) corresponds to the hot spot in dot 3 and is not used in this experiment.

To get an upper bound for the shuttling speed we apply a sequence where we again hop from dot 1 to 2, and dot 2 to 3 in 1 ns each, and then pulse to the hot spot in dot 4 for a varying amount of time; the result is shown in Fig. 7.3(b). This shows that after waiting 150 ns, the whole spin state has relaxed resulting in an upper bound of shuttling of ~150 ns. For quantifying this upper bound we are now limited by the relaxation time of the hot spot in dot 4. We have verified that by using just dot 4 (i.e. load in dot 4, move to hot spot, and read-out from dot 4) that ~150 ns is the fastest relaxation time of this hot spot.

7.4. DISCUSSION

The upper bound of 150 ns is not yet enough to guarantee that a coherent spin transfer can be performed inside a GaAs device with a $T_2^* \approx 20$ ns. It is however promising that

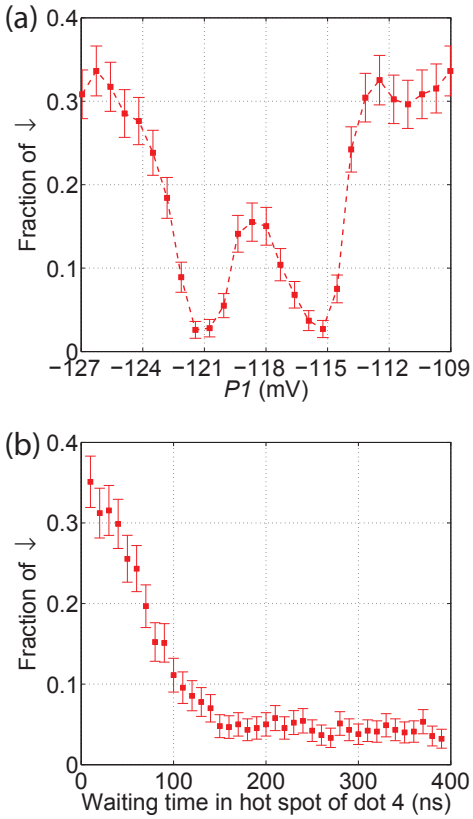

Figure 7.3: (a) A random electron-spin is loaded inside dot 1. It is then shuttled to dot 2 for 1 ns, and next to dot 3 for 1 ns. Afterwards we vary P_1 across the inter-dot transition of dot 3 and 4 and wait there for 500 ns to identify the location of the hot spots. Each datapoint is an average of 999 measurements (error bars two s.d.). Dashed line is a guide to the eye. (b) Same pulse sequence as (a), only this time we pulse to the hot spot in dot 4 determined from (a) ($P_1 \approx -121$ mV), and vary the waiting time inside the hot spot. Each datapoint is an average of 900 measurements (error bars two s.d.).

the spin shuttle seems to function without loss of spin-information for a shuttling time as short as 3 ns such as shown in Fig. 7.2, indicating that a coherent transfer could already be feasible in this system. In each case, 150 ns is fast enough in different host materials such as Si or Si/SiGe where this shuttling technique could in principle also be applied.

In summary, we have demonstrated a spin shuttle inside a quadruple-quantum-dot device where an electron-spin is shuttled within at most 150 ns across the four dots. This work forms the next step in performing a spin shuttle using electrostatic gates that demonstrates preservation of a quantum superposition, an essential ingredient for powerful quantum computing architectures.

7.5. SUPPLEMENTARY MATERIAL

7.5.1. METHODS AND MATERIALS

The experiment was performed on a GaAs/$Al_{0.307}Ga_{0.693}As$ heterostructure grown by molecular-beam epitaxy, with a 90-nm-deep 2DEG with an electron density of $2.2 \cdot 10^{11}$ cm^{-2} and mobility of $3.4 \cdot 10^6$ cm^{2}V^{-1}s^{-1} (measured at 1.3 K). The metallic (Ti-Au) surface gates were fabricated using electron-beam lithography. The device was cooled inside an Oxford Triton 400 dilution refrigerator to a base temperature of ~22 mK. To reduce charge noise the sample was cooled while applying a positive voltage on all gates (ranging between 100 and 400 mV) [85]. Gates $P1$, $P3$ and $P4$ were connected to home-built bias-tees (RC=470 ms), enabling application of d.c. voltage bias as well as high-frequency voltage excitation to these gates. Frequency multiplexing combined with RF reflectometry of the SDs was performed using LC circuits matching a carrier wave of frequency 81.0 MHz for SD2. The inductors are formed by microfabricated NbTiN superconducting spiral inductors with an inductance of 4.6 μH for SD2. The power of the carrier wave arriving at the sample was estimated to be -103 dBm. The carrier signal was only unblanked during readout. The reflected signal was amplified using a cryogenic Weinreb CITLF2 amplifier and subsequently demodulated using homebuilt electronics. Real-time data acquisition was performed using a field-programmable gate array (FPGA DE0-Nano Terasic) programmed to detect tunnel events using a Schmitt trigger. Voltage pulses to the gates were applied using a Tektronix AWG5014. Microwaves were generated using a Rohde & Schwarz SMR40 generator connected to P_3 via a homemade bias-tee at room temperature.

7.5.2. CHARGE STABILITY DIAGRAM MEASURED ON A SLOW TIMESCALE

The charge stability diagram shown in Fig. 7.1(a) of the main text has been taken in a so-called 'fast-honeycomb' mode [117]. Using the bias-tees connected to P_1, P_3 and P_4 it is possible to step one of them 'slowly' using a DAC and apply a triangular ramp on the other using the AWG. This significantly speeds up the measurements compared to stepping both gates using DACs. In Fig. 7.1(a) of the main text we plot the reverse sweep, i.e. the voltage on the x-axis is swept from positive to negative (with a rate of 220 mV/4.4 ms). The fading of the charging lines of dot 2 and 3 can then be explained from the indirect coupling with a reservoir [23]. To verify that this is correct, we have also measured Fig. 7.1(a) in a slow mode where we step both gates using a DAC, the result is shown in Fig. 7.4.

7.5.3. MEASUREMENTS OF THE INTER-DOT TUNNEL COUPLINGS

The tunnel coupling at zero detuning between neighbouring dots was measured using photon-assisted tunneling (PAT) [86], see Fig. 7.5. The data is fitted to $\sqrt{((P_1 - P_{1,\text{offset}}) \cdot \alpha_{P_1})^2 + 4t^2}$ where α_{P_1} is the lever arm that is different for each inter-dot transition (not used in this experiment).

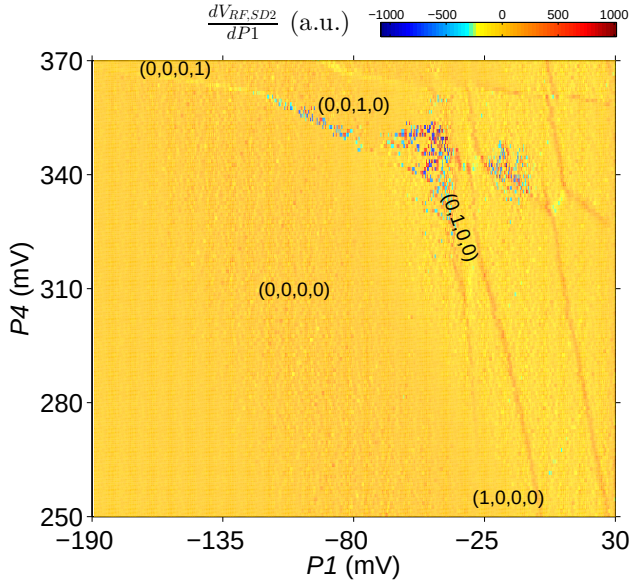

Figure 7.4: Charge stability diagram as in Fig. 7.1(a) of the main text, only measured in a 'slow' mode where both gates are stepped using a DAC. All the additional lines inside (0,0,0,0) of Fig. 7.1(a) of the main text are not visible anymore. This measurement took ~8 hours.

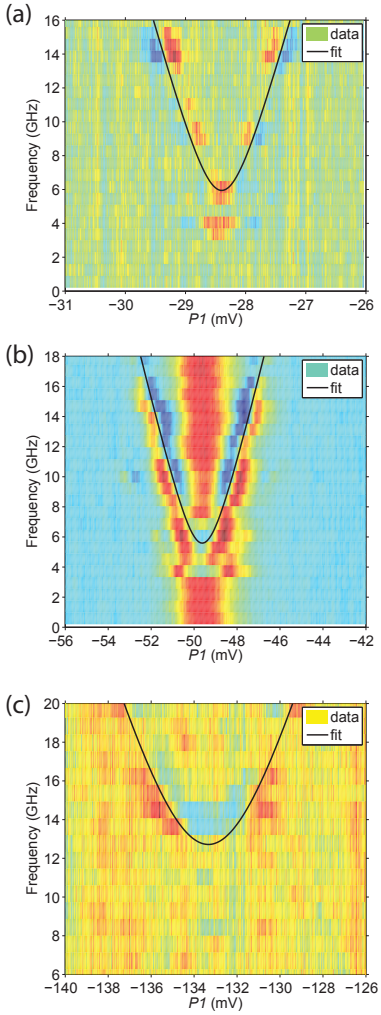

Figure 7.5: (a-c) Measurements of the tunnel coupling at zero detuning between neighbouring dots. (a) PAT between (1,0,0,0)-(0,1,0,0) resulting in $t_{1,2} \approx 3.0$ Ghz. (b) PAT between (0,1,0,0)-(0,0,1,0) resulting in $t_{2,3} \approx 2.8$ Ghz. (c) PAT between (0,0,1,0)-(0,0,0,1) resulting in $t_{3,4} \approx 6.4$ Ghz.

8

CONCLUSIONS AND OUTLOOK

This thesis is focused on the CCD operation and long-range coupling of single-electron spins in quantum dot arrays. This chapter summarizes the work presented in this thesis, puts it in the broader context of the field of laterally defined quantum quantum dots and gives suggestions for how to proceed from here.

8.1. CONCLUSIONS

A single-electron spin is a canonical two-level system. A single electron can be used as the information carrier in the form of a quantum bit. Also, the collective behaviour of many electrons together can give rise to a variety of interesting phenomena ranging from electricity & magnetism to the nature of the chemical bond. In this thesis progress has been presented on several fronts with the aim of better controlling multiple electron spins.

Single-spin CCD

In Chapter 4 three electrons are captured in a linear triple-dot array and operated in a CCD-like way. This chapter is the first experimental result where multiple spins are read-out, and where it is shown that the spin state of an electron is not significantly changed when shuttled across large distances. To understand why it is special that this result has been demonstrated, it is important to understand which challenges had to be overcome.

For the read-out it is experimentally hard to measure the spin state of an electron directly due to its small magnetic moment. As a solution, the spin information is converted into charge information using a technique called spin-to-charge conversion. Several approaches exist, and the one chosen in this work is the so-called 'Elzerman' read-out method [47]. In that approach, the energy level of a quantum dot is tuned in such a way that an excited spin-↓ has enough energy to leave the quantum dot, whilst the ground state spin-↑ will remain in the dot. Whether an electron leaves the dot or not, can be monitored using a nearby charge sensor such as a sensing dot. Several requirements need to be fulfilled for this to work:

1. The signal bandwidth of the charge-sensor setup should be large enough such that the spin-state can be determined before the spin has relaxed to the ground state (T_1-process).

2. There should be a reservoir for the electron to tunnel into.

3. The electron temperature of the reservoir should be low enough such that we can distinguish the two spin states split by the Zeeman energy.

4. The energy levels in the dot should be sufficiently stable over time. No large jumps in the charge stability diagram should occur during an experiment due to for example a switchy nearby two-level system. And slow drifts in the charge states should be corrected for.

In the case of more than one quantum dot, several extra requirements are added:

5. For multiple dots it is in general not true that each dot is connected to a reservoir. As a consequence, the electrons in dots without a reservoir eventually need to be shuttled to a dot with a reservoir. This shuttling should not randomly influence the spin-state.

6. The signal bandwidth should in this case be large enough to determine the spin-state of *all* spins that need to be read-out before they relaxed. If this read-out is

done sequentially, it implies that the *total* read-out time should be less than the T_1-time.

7. In order to have interaction between the two quantum dots (e.g. to perform a two-qubit gate) an interdot tunnel coupling of a few GHz is required. In practice this can quite easily be attained by 'pushing' the two quantum dots closer together using the gate voltages. However, the high interdot tunnel coupling needs to be combined with a sufficiently high tunnel coupling with the reservoir in order to read-out the spin state well within the T_1-time. And this requires pushing the quantum dot closer to the reservoir, instead of to its neighbour. This conflicting requirement can be hard to satisfy in practice.

In Chapter 4 we meet requirements 1-6 and partially satisfy requirement 7[1]. This has been achieved by combining several solutions:

1. Achieving high signal bandwidth by implementing RF-readout as described in section 3.2.2.

2. Designing the system to reach a sufficiently low electron temperature of 75 mK. This allowed us to work at relatively low magnetic fields with corresponding higher T_1-times.

3. Finding stable charge states in a range of possible gate voltages by testing several options for their stability and changing the bias cooling [85] if no stable regime was found.

4. Adding calibration routines to periodically correct for small drifts in the read-out positions.

5. Aligning the quantum dot axis and the direction of the applied external magnetic field in such a way that spin-orbit interaction during shuttling is minimized.

6. Applying carefully tuned pulse sequences such that an electron stays inside the quantum dot array whilst being shuttled (instead of for example being exchanged with electrons from the reservoir).

These solutions combined led to the result that it was possible to read out the three electron spins sequentially in a way that resembles the working of a charge-coupled device. The charge sensor was closest to the right reservoir, so first the rightmost spin was read out. Next, the right dot was emptied and the middle spin was shuttled to the rightmost dot and read-out. Finally, the leftmost spin was shuttled all the way to the right and its spin state determined. This was all done well within the T_1-time leading to read-out fidelities of on average 97%. Suggestions have been made to improve the read-out fidelities.

Besides reading out randomly loaded spins, it was also possible to initialize the CCD array into the ground state $\uparrow\uparrow\uparrow$ by only picking up spin-$\uparrow$ from the reservoir. Due to slight differences in g-factor in each of the three dots, we could next selectively flip either of

[1] Requirement 7 has later on been satisfied in Chapters 5 and 7.

the three pixels using adiabatic inversion by EDSR [76]. This corresponds to writing the pixels of the CCD.

The fact that multiple spins were read out is one of the highlights of that chapter. The most significant result is however that it was also demonstrated that shuttling a single spin across a cumulative distance of 80 μm had no measurable influence on the z-projection of the spin state. By carefully designing pulse sequences the spin was programmed to hop more than 500 times without leaving the dot array. The high fidelity with which the spin projection can be preserved upon shuttling between dots thus allows scaling the Single-spin CCD concept to linear arrays of hundreds of dots.

Coherent spin-exchange via a quantum mediator

The Single-spin CCD work shows that it is possible to read out and move around many spins in a controlled way. This was combined with rudimentary single-spin manipulations. In order to use the full potential of this system, interactions between the electrons are required. Previous work had demonstrated a two-qubit gate between neighbouring dots, see for example Refs. 53, 122. It would have been possible to apply the same approach in the triple-dot array and apply two-qubit interactions between qubit 1 and 2, and qubit 2 and 3. This would partially resemble the results demonstrated for the exchange-only qubit [119], except that in that case effectively only one qubit was made inside a triple-dot array. It was more interesting at this time to show that it is also possible to couple spins that are not residing in neighbouring dots, and instead show that over a longer distance quantum coherence would still be preserved. Long-range interactions are an interesting research topic as they lie at the heart of quantum simulations and computations. In the context of quantum computation, it leads the way to viable quantum computer architectures. Long-range coherence is also a necessary ingredient for performing quantum simulations of materials and molecules with non-nearest neighbour couplings such as MnO [109, 110], high-temperature superconductors [111, 112] and DNA [113].

Earlier work in Refs. 116, 135 gave experimental evidence that *charge* could oscillate between the outer dots of a triple-dot array whilst virtually occupying the middle dot, giving rise to an effective tunnel coupling between the outer dots. Motivated by this result, we explored whether this effective coupling could also be used to couple two distant *spins*. In Chapter 5 we demonstrate that this coupling is indeed possible. The two outer dots are each occupied with a single-electron spin and experience a superexchange interaction through an intermediate level of the empty middle dot. We measure the coherent time evolution of the spin states on the outer dots and observe a non-monotonous dependence of the exchange frequency as function of the detuning of the intermediate energy level.

We simulate the measured data using the measured nearest-neighbour tunnel couplings (~10 GHz), detunings and the difference in Zeeman energy probed through electric-dipole spin resonance measurements. We include the effect of dephasing by charge noise which limits the total number of oscillations to ~ 10, account for the known readout fidelities and include the gradual turn on and off of the superexchange due to the finite risetime of the applied pulses. The good agreement between theory and experiment allows us to conclude we are indeed driving the time evolution of the outer spins

by superexchange. It thereby constitutes the first working example of using a quantum coupler, the middle dot, to induce a coherent interaction between two distant spins in a solid-state environment.

Computer-automated tuning of semiconductor double quantum dots into the single-electron regime

Whatever the type of experiment one intends to perform with single-electron spins in gate-defined quantum dots, all of them will require the tuning of gate voltages to arrive at the desired conditions such as number of electrons in each dot and the coupling between them. This tuning can be time consuming as each dot is unique due to sample inhomogeneity, and changing the settings of one dot tends to influence the settings of the neighbouring dots due to cross-capacitive coupling. The ability to tune these dots automated by computer algorithms, including tuning of many dots in parallel, is an important ingredient towards the scalability of this approach to create a large-scale quantum computer. It will be practically impossible for a human to tune a million-quantum-dot device.

In Chapter 6 we perform the first non-trivial step in automating this tuning by implementing an algorithm that manages to create double quantum dots into the single-electron regime and recognizes that this goal has been achieved. The algorithm is specifically written for the device design used in this thesis and operates as follows:

- The user inputs a range of gate voltages for the shared T-gate for which the algorithm should try to find double quantum dots[2].
- To determine the starting values for the other gate voltages, we first measure the pinch-off characteristic between each individual gate and the shared T-gate.
- Based on the results of the previous step we create single quantum dots.
- The required tunnel barriers acquired for the single dots can be used as a starting point to create double dots into the single-electron regime.

In this chapter the algorithm is benchmarked by creating three double-quantum dots inside a quadruple-quantum-dot array. Although still far away from a future large scale device, it already forms a very helpful tool in the lab to determine if a sample is useful or not. Especially since the algorithm can be run overnight and gives the user a conclusion the next morning after loading a sample.

Nanosecond-timescale spin transfer using individual electrons in a quadruple-quantum-dot device

The Single-spin CCD result demonstrated that it is feasible to shuttle electron spins through an array. The tuning for this triple-dot sample however involved relatively low tunnel couplings making it impossible to shuttle the spin state within the spin dephasing time across the device (T_2^*). The ability to move a coherent superposition around during the coarse of a quantum computation is an important ingredient for a large-scale quantum computer [64].

[2] This step can also be automated in the future.

For the experiment in Chapter 7 more effort was spent to tune all the interdot tunnel couplings to >2.5 GHz, and an extra dot was added giving four dots in total. This chapter first of all demonstrates that it is possible to tune a quadruple-quantum-dot device into the single-electron regime with sufficient coupling with the reservoirs *combined with* high interdot tunnel couplings. This will in principle allow one to use this device to operate four qubits with sufficient interaction between them to also drive two-qubit gates. This work also demonstrates that it is possible to shuttle an electron spin state within ≤150 ns throughout the array. This upper limit stems from the relaxation time of a 'hot spot'. *Programming* a pulse to shuttle an electron within 3 ns seems to function without loss of spin-information but it cannot be guaranteed that the spin made it in 3 ns. The upper bound of 150 ns is however already enough to shuttle an electron spin within the dephasing time of a Si-based quantum dot.

8.2. OUTLOOK

The results in this thesis are steps in bringing the field of gate-defined quantum dots forward. Irrespective of which material is used, e.g. GaAs, SiGe or Si-MOS, many elements of each individual chapter can be used to take next steps. The principle of the Single-spin CCD shows great promise that it will also work for hundreds of quantum dots. It would be great if these could all be tuned automatically using a similar algorithm as has been demonstrated in Chapter 6. And strong evidence can be found in Chapter 7 that such a CCD can be operated at high speed. Future work would certainly benefit from non-nearest neighbour couplings. Chapter 5 gives a first working example that that is possible, and it is likely that future experiments will explore how a similar principle can be used using different mediators.

In this Outlook several future approaches are discussed and challenges that need to be overcome are listed.

8.2.1. DIFFERENT HOST MATERIALS

All work in this thesis has been performed using GaAs as host material for the electron spins. This substrate has been used for over 20 years to create quantum dots [136] and has been used intensively due to the relative ease of device fabrication. A significant drawback of GaAs is the hyperfine interaction between the electron and the nuclear spins of the host material (see section 2.2.2) that causes rapid dephasing on the ~10 ns timescale [26]. Multiple approaches exist to extent the qubit lifetime by using for example dynamical decoupling [40], measuring faster than the coherence time of the nuclear bath [137] or by influencing the nuclear spin environment itself [44]. These examples show that it is in principle possible to use GaAs as host material for qubit experiments. However, by moving to a different host material that have less to no nuclear spins, such as Si [42], Si/SiGe [43] or carbon nanotubes [18], all the additional effort required in the previous examples is no longer necessary to achieve longer qubit lifetimes. It is therefore likely that a large-scale quantum computer will be created in a nuclear-spin-free host material.

Of all the options for a host material, Si is a very promising one due to its similarity

with the current semiconductor industry. There are however still some open questions that need be addressed before it is clear that this is indeed a viable option. Challenges include:

1. Fabrication of Si-quantum dot devices is not yet very reliable. Ohmic contacts do not always function properly, and in some cases the gates are leaky. Nowadays several labs around the world have been successful but it is not yet routine work.

2. Si-substrates are not always good enough to host quantum dot devices. It is for example not yet routinely possible to create structures with sufficient mobility.

3. The effective mass of electrons in Si is much higher compared to GaAs: $m^* = 0.19m_0$ versus $m^* = 0.067m_0$, where m_0 is the mass of a free electron. This introduces two extra challenges for Si-based materials:

   (a) The electron tunneling rate across a barrier of height E_B and width d is proportional to $e^{-2\sqrt{2m^*E_B}d}$. Given the larger effective mass in Si, dots need to be brought closer together to achieve the same tunnel coupling, and the tunnel coupling is more sensitive to small variations in E_B (i.e. gate voltages). This makes it hard to achieve large interdot tunnel couplings such as has been shown in e.g. Chapter 7 for GaAs.

   (b) The orbital-energy spacing inside a quantum dot scales with $\frac{1}{m^*a^2}$, with a the radius of the dot. As a result, it is more difficult to reach the single-electron regime, and it is more likely that disorder in the potential landscape will give rise to additional unwanted dots.

4. The symmetry of the Si-crystal structure gives the electrons an additional degree of freedom known as the valley. The valley energy splitting can be on the order of, or even smaller than the thermal energy [43, 138]. This can result in leakage of quantum information into excited valley states which deteriorates the fidelity of qubit operations. Experiments have demonstrated that in some cases it is possible to tune the valley splitting, see for example Ref. 82. Future device optimization may also ensure that the valley splitting will be sufficiently large.

Multiple labs around the world are now working intensively on getting Si-based qubits to work. A promising recent result is the first demonstration of a two-qubit gate in a Si-device [91] (combined with single-spin rotations and read-out).

8.2.2. SCALING

The state-of-the-art devices contain at most 4 to 5 quantum dots [125, 126]. Past decades have been spent on getting good control of 1 or 2 dots such as proper initialization, read-out and showing single- and two-qubit gates [26]. Coherence times have in the meantime improved by orders of magnitude from the ns timescale to the ms timescale. A clear next goal should be to show that we can control many qubits. One could think of extending the linear arrays to increase the number of dots, but that may not be the best approach. A viable quantum computer requires quantum error correction (QEC) and one of the best known approaches at this time is to apply the so-called surface code [139].

This scheme requires a 2D square lattice of nearest-neighbour coupled qubits with initialization, read-out, memory and quantum gates all operating with errors of less then ~1%.

Even when we have reached this threshold in a few-dot system, it is still a hard problem to scale this up. The following points need further investigation:

Qubit uniformity
Due to sample inhomogeneity each quantum dot requires its own tuning. If you find the right set of gate voltages to control one dot, it is very unlikely that you can use the same settings for a different dot, or even the same settings for the same dot after a thermal cycle. These variations stem from local variations in the host material and possible variations in the gate pattern stemming from fabrication (the metallic gates will not be identical). If these two issues have been improved, it is likely that this field will make a tremendous jump forward.

Tuning of many dots
Better qubit uniformity will make it easier to tune up a large number of quantum dots. Especially if this is done by an automated routine such as demonstrated in Chapter 6. It is still an open question what the best approach is to automatically tune more than 2 dots. One option is to first characterize all the single dots and then 'stitch' them together one by one. Another option is to create for example many double (or more) dots and stitch those together. This needs to be investigated in practice. A clear challenge comes from the cross-capacitance between the dots: changing the tuning of one dot, also influences the properties of the neighbouring dots. We observe that this cross-coupling extends for at least three neighbours making it a highly coupled system.

In practice it would be great if the data acquisition rate would be improved and that we end up with video-rate scans of charge stability diagrams, see for example Ref. 127. This will speed up the automated tuning, and give the human user a lot of flexibility to quickly change dot parameters to optimize the settings. Another improvement that I expect is likely to happen is that we eventually abandon charge-stability diagrams as the main tool to operate the quantum dots. Already in Chapter 7 we notice that it becomes increasingly complex to navigate inside such a diagram. As an alternative, it would be great if we could eventually start looking at the system in terms of electrochemical potential ladders such as drawn schematically in for example Fig. 4.1b. Ideally, such an interface also allows 'dialing in' the the desired tunnel and capacitive couplings.

Wiring
The amount of wiring needed will go up as the number of qubits increases. Coaxial cables and DC-wires are currently all brought in from room temperature all the way to the coldest plate of ~10 mK. This wiring requires space and cooling power. It is not yet obvious what a million-qubit setup would look like to accommodate all required control lines. Part of the solution will involve multiplexing where one line is used to transmit a signal to several qubits. This could involve a multiplexer at low temperatures with flash-memory cells that bias e.g. the gates. Investigations are underway to understand how

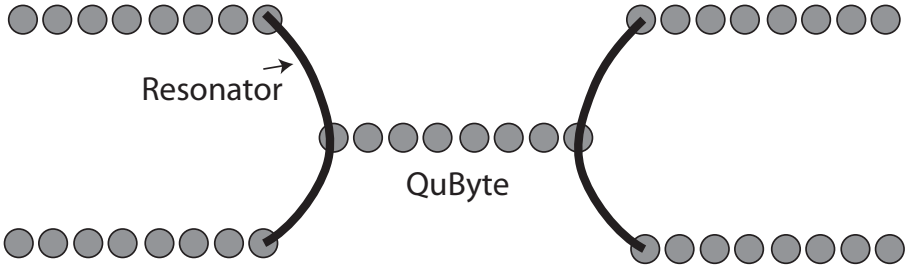

Figure 8.1: Sketch of coupling linear arrays of 8 dots, 'QuBytes', using a superconducting resonator. This approach allows for more space for the control wiring.

this can best be done at low temperatures.

Another open question is what the design of the quantum dots should look like to make it scalable. We need to come up with a design that can be *copy-pasted* across a surface without losing functionality. This is clearly not the case for the gate designs used in this thesis as the sides of the device were used to spread out all the wiring. Solutions will likely include a so-called interconnect where the third dimension is used to connect qubit gates to a control unit on top. To reduce the number of charge sensors we may need to adopt dispersive gate read-out as demonstrated in Ref. 79. In parallel, 'breathing room' for wires can be created by using large mediators to couple distant qubits: e.g. a superconducting resonator (see section 8.2.3 and Chapter 5 for more examples). These mediators themselves ideally do not require a lot of wiring such that the space around them is available to spread out the control wires for the quantum dots. See Fig. 8.1 for a sketch where so-called 'QuBytes' are coupled to one another using a resonator. The space around the resonator can be used for wiring. We are currently very experienced in operating linear arrays so this may be a very reasonable experiment for a near-future experiment to demonstrate a scalable design.

The field may even move fully to qubits operated at higher temperatures (1-4 K). Working at these temperatures does not require a dilution unit with He-3, and allows much higher heat dissipation of the electronics. If the singlet-triplet splitting can be made large enough it may be possible to operate a ST-qubit at these temperatures.

The second dimension

Most of the experiments so far have been performed in linear arrays. A notable exception is demonstrated in a 2x2 system in Ref. 125. It is expected that the fabrication techniques for laterally defined quantum dots are compatible with the highly-developed semiconductor industry, which should eventually allow the fabrication of large two-dimensional arrays thereby drastically increasing the number of qubits. It is infeasible to right away operate 1000x1000 qubits and Fig. 8.2 gives a sketch of what a more realistic near-future experiment could look like. Also here, it is likely that some breathing room is required that can be given by large mediators. It will be very interesting to investigate how to operate such a 3x3 array where there is also a center dot that is fully decoupled from any reservoir. How large can NxN become before the system becomes practically too hard to

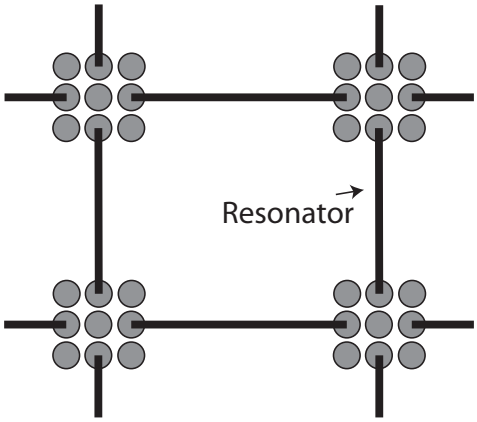

Figure 8.2: Sketch of coupling 3x3 arrays using superconducting resonators. 3x3 arrays would be a non-trivial example of using the second dimension in the design of laterally defined quantum dots.

operate? It is very likely that the second dimension will give rise to additional effects. For example, in Chapter 4 we on purpose minimized the effect of spin-orbit coupling along the axis of shuttling. For a 2D system, it will not be possible to minimize this effect along both directions and (predictable) spin-orbit effects need to be taken into account for at least one direction. This is also the case for Si-systems that induce an artificial spin-orbit interaction through the presence of a micro-magnet. The spin-orbit interaction could then also be used as a tool to change the spin-direction in a desired way.

8.2.3. LONG-RANGE COUPLING

The surface code does not require qubit interactions beyond nearest-neighbour. Still, it is very interesting and relevant to study what happens if next-nearest neighbour interactions are included. They may not be a stringent requirement for a quantum computer, but in the field of quantum simulations they would be a useful asset to model complex materials [109–113]. The work in Chapter 5 demonstrates a first working example of such long-range spin-spin coupling through the superexchange mechanism. It is fair to say that in this example there was no qubit in the middle so in a way one could argue the two outer spins were effectively nearest-neighbours again. A theoretical proposal exists to also make this work with the center dot occupied [105], but this requires very high photon frequencies that are not (yet) feasible in the lab. It is also not obvious that the superexchange mechanism is the best approach to achieve long-range coupling. It requires a rather complicated structure as mediator (a fully tuned quantum dot). Other approaches, such as a superconducting resonator [107, 108], floating metallic gates [96, 140] or a ferromagnetic coupler [97], are likely to give more 'breathing room' on the sample space, and in principle do not require tuning. It is likely that in the near-future experimental results will be shared that use a different mediator than an empty quantum dot. Up till that time, the result in Chapter 5 has been an interesting first demonstration of coherent spin-exchange between distant spins in the solid-state.

Last but not least, several labs are now actively pursuing the possibility of physically

moving the qubit containing the quantum information from one node of the quantum processor to the other. Using either surface-acoustic waves (SAW) [69, 70, 132] or a shuttle operated by gates [117] electrons can be moved from one location to the other. Each of these approaches has shown that it is likely that the electron spin can be shuttled within the dephasing time. No evidence has yet been published that a quantum superposition was actually preserved. For such an experiment it is for example also important that the jitter on the tunnel events is small compared to the difference in qubit frequencies in each dot (due to e.g. a micromagnet or different g-factors). At the moment of writing this thesis a follow-up experiment on Chapter 7 shows promising data that the quantum phase is preserved during the shuttle. In this experiment a singlet is created in the leftmost dot, and next one of the two electrons is shuttled to one of the three other dots for a varying amount of time. The data shows coherent singlet-triplet oscillations with a frequency that depends on in which dots the electrons reside (resemblant of the different g-factors in Chapter 4 and 5). This is a strong signature that we can indeed move a quantum superposition around. Another interesting experiment would be to verify if the theoretical concept of 'motional narrowing' can be demonstrated in practice [141]. During the shuttling the electron spin will probe different nuclear spin environments, each with a random orientation. It is expected that the spread in the effective Overhauser field will therefore decrease with the square root of the number of dots that are traversed during the shuttle. This should result in a longer dephasing time.

8.2.4. HOW TO OPERATE THE QUANTUM DOTS?

At the moment many labs are pursuing a qubit architecture that is compatible with the surface code. Most of the expected near-future experiments in quantum dots will probably not yet be at the stage where surface code is directly applicable. See for e.g. the proposed experiment in Fig. 8.1. It is important to better understand what types of algorithms can already be run on such an architecture. On a similar topic, it is at the moment also not yet obvious which type of qubit is the best: Loss-DiVincenzo [13], Singlet-triplet [122], Exchange-only [119], the Hybrid qubit [142] or possibly a different one? They each have their advantages and disadvantages. Differences include (1) sensitivity to charge and nuclear noise, (2) required external magnetic field, (3) different control axes, (4) required number of quantum dots per qubit and (5) how two-qubit gates can be applied. It is still an open question which qubit is most suitable for a large-scale system.

The outstanding challenges described in this chapter may seem daunting at first. And indeed they are very complex problems that need to be solved. Most of the steps that we take are still new and raise interesting scientific questions that need to be solved. It is not clear at this point in time if we will manage to do so, and likely more obstacles may come along the way. What is clear, is that there is room for optimism. There is a significant interest from large companies to invest in this type of research (e.g. Google, Intel, Microsoft, IBM). It is almost guaranteed that something useful will come out, although we may currently not yet be aware what that may be (e.g. the world wide web as spin-off from CERN). And last but not least, progress may go faster than expected. Two years ago

it was hard to believe we would have a quadruple-quantum-dot device running at this point in time: I'm glad to say that today I can wish my successors all the best with this currently operational device.

Tim Baart

ACKNOWLEDGEMENTS

Working on a challenging topic is something best done together. Some of our technical components may for example look fairly simple from a distance, but I soon realized that they were typically developed over the course of many years or even decades. Figuring out how to best use it, can then not be done alone within a reasonable timespan. And this is just an example of something that is already up and running. When facing obstacles during an experiment that had never been encountered before, it is a big relief to be able to discuss with others what to do.

I would like to start by thanking Lieven for his supervision during my PhD. During my studies I had the opportunity to work for a variety of supervisors and Lieven was one of them. It was clear to me that we would become a good match. Your in-depth knowledge of physics is enormous, and in some way you always manage to ask the right questions to help improve other people's work. The freedom you give to your students is great. If there are several pathways we can take during an experiment, you gave us advice on what could happen on every one of them, but you never forced us to pick a specific one. This always ensured that we choose the topic we most liked and felt very responsible for it. I want to wish you all the best with the Intel collaboration and I hope that in the near future your children can actually admire what you have been teaching them to say as one of their first words: 'pappa bouwt een kwantumcomputer'!

For most of my PhD I worked together with Mohammad and I learned a lot from him. Varying from how to cool down a fridge, how to write proper computer code, how to become very stressed ;P, and any details regarding all the electronics used. We faced many challenges and we had to try many different things before we managed to get something new to work. At the start we were planning to demonstrate fast Rabi oscillations in a double dot, but after roughly 1.5 years realized we would not be successful. In the meantime I was making quadruple-dot devices but none of the batches turned out to be stable. Luckily, we could use a sample from Floris and got it to work. It is a pity you had to leave Delft on the evening (!) that three-dot read-out started working. You left behind a very nice piece of software that has allowed us to do many follow-up experiments, many thanks for that!

Soon after Mohammad left I had the pleasure to work with Takafumi. You must have felt somehow this was the right moment in time to join because we managed to measure a lot of cool stuff together! It is impressive to see how fast you catched up with the running experiments, started eating Dutch sandwiches with cheese and how you managed to write impressive Mathematica codes to simulate our experiments. I am sure many more successful experiments will be done by you!

I had the opportunity to supervise two master students during my PhD. The first was Jules van Oven with whom we developed most of the RF-readout system. I really appreciated you working attitude that allowed you to get things done, and you asked many good questions. The RF-readout system made it possible that I can now present

these nice results in this thesis. Without it, the read-out fidelities would have been much worse, and I am sure we would have had a lot more problems with the noise sources in our system. I am grateful that we managed to circumvent that!

The second student was Natasja Jovanovic who helped me to get the quadruple-dot device tuned. This was the first quadruple-dot device in the single-electron regime in Delft! We had a fun time and I enjoyed working together with you. Even when the fridge warmed up for the so-manyth time (...), you were always ready to start all over again. Eating brownies in those dark times helped both of us :). We managed to shuttle a spin at high speed, and we can now use your good starting point to aim for the next big step of coherent transport.

I have gotten a lot of useful input from the other members of the spin qubit team. Pasquale was always around to help with whatever you asked, and you were like a walking encyclopedia regarding spin qubits. I hope you will have a great time in ETH and can eventually start your own group in Italy. Erika, you are always so kind and polite. I am impressed by your motivation to understand everything and the insane working hours you can make. I really enjoyed our visit to Japan and think we should go there once more to visit a karaoke bar! Floris, I was glad to be able to talk with a more down-to-earth Dutch guy once in while :), and you really made a big change to my PhD by giving us your triple-dot sample. Toivo, Udi, you are a fun team together and I hope your project of 'many dots' will show awesome results in the near future. Jelmer, Tom, good luck with creating the perfect qubit in Si/SiGe.

As one of the first students I also had to opportunity to work with someone from TNO, Pieter Eendebak, through the QuTech collaboration. Pieter, even though you had no background in quantum dots whatsoever, very soon you started making your own dots, and in some spare time even made a movie of a triple dot forming out of nothing. I think we were a very good and efficient team, and I enjoyed seeing how a more experienced person solves problems. I liked your down-to-earth approach.

A critical team of people was formed by the technicians. The general technicians, Bram, Remco, Jelle, Mark and Siebe, were always around to fill a helium vessel, help fix a broken pump and find solutions to general problems. I had a lot of fun during the coffee breaks with you guys. Whether it was grumpy Bram complaining about the TU, Remco predicting the downfall of the world based on the Maya calendar or Mark trying to convince us to look at the bright side :). The team of electronics-related technicians was formed by a.o., Raymond Schouten, Marijn, Raymond Vermeulen, Berend, Jack, Ruud and Rogier. Crappy electronics implies crappy experiments, and I was very glad I could rely on you to build impressive electronics for us, figure out why there is this strange noisy signal in the lab, or just explain how things work. The amount of time invested by you in my projects was huge, and I would like to sincerely thank you for that. The cleanroom technicians, Marco van der Krogt, Ewan, Marc, Arnold, Anja, Frank, Charles, Roel, Hozanna, Marco Bakker, were a very welcome guidance during the black magic taking place in the cleanroom.

In the background Yuki and Marja made sure that I could mostly focus on my research. I almost never had to do any paperwork, and I know you two were responsible for that :). I think it is great to see that you two supported QT for so long in an extremely efficient and helpful way. Just two people for such a large group! And Yuki, I will keep on

watching LuckyTV so that we stay synchronized ;P.

Julia, Pauline and Arjan, thank you for being around not only as colleagues but especially also as friends within the TU. For a long time the spider you gave me for my birthday was the only 'spin' I could actually flip hahahahaa. I had a great time with you guys at the TU and hope to still see you around afterwards.

The fact that I started a PhD is caused for a large part by my previous daily supervisors. Marius Trouwborst, you really sparked my interest in experimental physics by introducing me to cryogenic systems and by measuring currents through single-atom thick golden wires. Stijn Goossens, oh oh oh, what did we think trying to capture single electrons in a material with no bandgap, hahaha. I still remember the day that I managed to break our first device, but that you stayed calm and we quickly managed to make new ones. We both appreciated Fred & Ria and going to classical concerts, I will never forget that. Shimon Kolkowitz and Quirin Unterreithmeier, you formed a crazy team together! The day that Quirin decided not to shave his beard till the experiment worked, taught me that you better be very patient in science, hahaha, you ended up like Santa Claus.

Outside of work I am very grateful to all my friends and family that make many jokes about my work, but are also very proud of what I have been doing. Peter, you flew all the way over to Boston to take me along to some fresh air in New York. At the same time you gave some valid advice on the strange shape of our probes: 'Ah joh, dat lijkt wel oxidatie!'. Eva, already during high school you started teaching me how to look at the bright side of life. That turned out to be a very useful asset during a PhD! Together, you and Peter, made sure that there was always something to laugh about and not to take everything to seriously :). Gertjan, yes, this is the first time I can properly acknowledge you for being a roommate for more than 6 years and for all the wonderful events involving crappy music, excellent whisky & cigars, discussions on where to go with this society and also very useful input for my PhD itself!

Aan de echte basis van dit alles liggen natuurlijk mijn ouders. Jullie hebben een zeer eigenwijs kind weten op te voeden, en op mysterieuze manier hier zo'n draai aan weten te geven dat ik redelijk op mijn pootjes terecht ben gekomen en heel blij ben met wat ik tot nu toe heb mogen doen. Jullie hebben mij altijd de vrijheid gegeven om zelf beslissingen te nemen, en dat vertrouwen waardeer ik enorm.

Tot slot een van de leukste dingen die mij is overkomen tijdens mijn promotie: Anna. Wat ben ik blij dat wij elkaar uiteindelijk hebben gevonden en nu al meerdere jaren gelukkig samen zijn. Als iets tegen zit weet je het altijd fijn in perspectief te zetten, en als iets goed gaat zorg je ervoor dat we het vieren. Elke dag dat we samen zijn zorgen we altijd wel weer voor iets geks dat ik niet snel zal vergeten. Op naar nog vele jaren samen!

Tim

A

FABRICATION RECIPE OF QUANTUM DOT DEVICES

In this Appendix we summarize the fabrication recipe used to fabricate the quadruple-dot devices. The fabrication recipe for the triple-dot sample can be found in [19]. This appendix is a continuation of the earlier work described in [143].

First some general remarks:

- The evaporation rates given in the recipe are mainly determined by the evaporator. For the big structures like the alignment markers and the large gates a higher rate is desirable, to shorten the time the evaporation takes. However a higher rate in the used evaporator could not be reached due to a maximum possible current through the filament.
- For all steps apart from the fine gates the given values for the dose, beam current and spot size only have to be met approximately. The given value for the dose is the lowest value which worked during the recent fabrication. A $100-200\ \mu C/cm^2$ higher dose can be applied without noticeably changing the structure, the only disadvantage being a longer writing time. A lower dose might result in too much resist residues after development. For the fine gates a dose test is done on a small spare corner of the chip.
- The lift-off is faster if the acetone is warmed up in a au-bain marie. Note that acetone boils at about 56°C. Also note that warm acetone evaporates extremely fast, such that care needs to be taken when taking the sample out of the beaker. Using a syringe filled with acetone (taken from the same beaker glass to prevent overflowing) you can spray on the sample to facilitate lift-off. In our experience you can spray as hard as you want with no risk of damaging (even the fine) gates.
- The details of the first resist layer (17.5%wt Copolymer) used for the alignment markers and the ohmics are : 8%wt MMA(methamethyl acrylate) in

MAA(methylacrylic acid) in ethyl-actate. In the Delft cleanroom the bottle is marked as 8%PMMA/MAA (17.5%) Ethyl Lactate.

- The used spinner is programmed to always spin at 500 rpm in the first 5 s of the spinning recipe.

(a) **Substrate preparation**

Cleaning front side:

- acetone clean (5 min)
- IPA rinse (30 s)
- N_2 (g) dry
- oven 120°C (10 min)

Clean Ga on the backside (necessary in case of wafers from Wegscheider group) :

- 1-2 μm photoresist, e.g. S1813 on front side
- bake on hot plate: 80 °C (15 min)
- Another layer of 1-2 μm photoresist on front side
- bake on hot plate: 80 °C (15 min)
- 2 min in hot HCl (50 °C)
- H_2O rinse (30 s)
- N_2 (g) dry
- Check if the Ga is sufficiently removed: if not, put the wafer again in HCl. Note: as long as gas formation occurs there is still Ga on the backside.
- acetone (30 min)

Remarks:

- Baking the photoresist too hot (even 120°C) resulted in resist residues which could not be removed, also not with an oxygen plasma strip.
- One layer of photoresist is not always enough to prevent the HCl from reaching the surface of the wafer. It is recommended to put two layers.
- If 2 min in HCl is not enough, you can wipe the backside with a small wiper (cleanroom 'Q-Tip') to facilitate the removal of Ga.

(b) **Alignment markers**

Preparation:

- acetone rinse (2 min)
- IPA rinse (30 s)
- N_2 (g) dry

Resist:

- first layer: 17.5%wt Copolymer (11%wt MMA(methamethyl acrylate) in MAA(methylacrylic acid)) in ethyl-lactate: ≈ 350 nm, 2250 rpm (55s)
- bake on hot plate 175 °C (10 min)

- second layer: 2% wt PMMA 950K in anisole: 100 nm, 1500 rpm (55s)
- bake on hot plate 175 °C (10 min)

Exposure:

- e-beam dose: 650 μC/cm^2 at 100kV
- spot size 100 nm, beam current 200 nA

Developing:

- 1:3 MIBK / IPA (1min)
- IPA stop (1 min)
- N_2 (g) dry

Evaporation:

- 50 nm Ti, rate 0.1 nm/s
- 150 nm Au, rate 0.1-0.2 nm/s

Lift-off:

- cold acetone 6h or warm acetone (53 °C) 3h / acetone spray
- IPA rinse (30 s)
- N_2 (g) dry

Remarks:

- The e-beam does not require such high markers (200 nm). However, after the annealing step for the ohmic contacts they tend to penetrate into the GaAs substrate which significantly reduces their height.

(c) **Mesa etching**

Preparation:

- acetone rinse (2 min)
- IPA rinse (30 s)
- N_2 (g) dry

Resist:

- 2% wt PMMA 950K in anisole: 90 nm, 2000 rpm (55s)
- bake on hot plate 175 °C (10 min)

Exposure:

- e-beam dose: 550 μC/cm^2 at 100 kV
- spot size 90 nm / beam current 160 nA

Developing:

- 1:3 MIBK / IPA (1 min)
- IPA stop (1 min)
- N_2 (g) dry

Etching:

- measure height of the resist *before* etching to have a proper reference height
- surface oxide removal: 1:5 H_2SO_4/H_2O (30 s)
- H_2O rinse (30 s)
- wet etch in 1:5:25 $H_2O_2/H_2SO_4/H_2O$, etchant cooled to 10 °C, rate ~3 nm/s
- H_2O rinse (30 s)
- IPA rinse (30 s)
- N_2 (g) dry

Remarks:

- The etch rate can vary for different wafers and is also quite sensitive to how precise the etchant is mixed. Also if the H_2O_2 is already old, its concentration might have changed. Etch a pure GaAs chip first to make sure that the etchant is mixed properly. The etch is then typically done in several steps, while checking with a profilometer in between the steps. The aim is to etch as far as the 2DEG lies, which in the wafers used here is typically around 100 nm.
- It has been observed several times that even the etch rate across a wafer is non-uniform. One side of a quarter wafer had been etched to a depth of 37 nm while the other side reached 89 nm. Care was taken to keep the sample horizontal during these runs.
- The etchant is cooled to 10°C to reduce the etch rate. Changing the ratio of the mixture can also reduce the rate.
- Care needs to be taken when the sample is taken out of the beaker filled with water or acid. The surface adhesion is much higher than of e.g. IPA, so the sample 'sticks' to the liquid surface. Also when rinsing the sample in water or moving it in the acid gentle movements are recommended, since parts of the resist can move otherwise.

(d) **Ohmic contacts**

Preparation:

- acetone rinse (2 min)
- IPA rinse (30 s)
- N_2 (g) dry

Resist:

- first layer: 17.5%wt Copolymer (8%wt MMA in MAA) in ethyl-lactate: 350 nm, 2500 rpm (55 s)
- bake on hot plate 175 °C (10 min)
- second layer: 2% wt PMMA 950K in anisole: 100 nm, 1500 rpm (55 s)
- bake on hot plate 175 °C (10 min)

Exposure:

- e-beam dose 650 μC/cm^2 at 100 kV
- spot size 100 nm, beam current 200 nA

Developing:

- 1:3 MIBK / IPA (1 min)
- IPA stop (1 min)
- N_2 (g) dry

Evaporation:

- 5 nm Ni, rate 0.1 nm/s
- 150 nm AuGe, rate 0.1 nm/s
- 25 nm Ni, rate 0.2 nm/s
- 50 nm Au, 0.1 nm/s

Lift-off:

- cold acetone 6h or warm acetone (53 °C) 3h / acetone spray
- IPA rinse (30 s)
- N_2 (g) dry

Rapid thermal annealing:

- ramp from room temperature to 440 °C in 40 s, forming gas atmosphere (90% N_2, 10% H_2)
- stay at 440 °C for 60 s, forming gas atmosphere
- cool down from 440 °C to 80 °C in ≈ 30 s, N_2 purge

Remarks:

- The final 50 nm layer of Au is not required. It does help in measuring a more reliable ohmic-contact resistance at room temperature. Typical values for the current mesa-designs are 30-60 kΩ measured in a range of ±50 μV. Note: higher resistances do not have to be a problem for measurements. Especially if RF-read-out is applied (see section 3.2.2). The resistance of the ohmic contacts of the quadruple-dot device were > 500 kΩ at cold; the RF-read-out still worked fine however. This could possibly be explained by a small shunt capacitance.
- The rapid thermal annealer uses a pyroelement, which measures the temperature by detecting the thermal radiation from the carbon holder on which the sample is loaded. The pyroelement is only reliably calibrated above ≈ 300°C.
- Some annealing runs were performed at Philips Eindhoven due to a broken RTA in Delft.

(e) **Fine gates**

Preparation:

- oxygen plasma strip (10 s)
- acetone rinse (2 min)
- IPA rinse (30 s)
- N_2 (g) dry

Resist:

- 2% wt PMMA 950K in anisole: 90 nm, 2000 rpm (55 s)
- bake on hot plate 175 °C (10 min)

Exposure:

- e-beam dose: ~750 μC/cm^2, 1.7 times higher dose for plunger and thin part of topgate. Exact dose value is determined from a dose test.
- spot size: smallest available (around 20 nm with an estimated spot size 2-3 nm) / beam current 400 pA, resolution in the pattern file: 2 nm, beamstepsize: 2 nm

Developing:

- 1:3 MIBK / IPA (1 min)
- IPA stop (1 min)
- N_2 (g) dry

Evaporation:

- 10 nm Ti, rate 0.1 nm/s
- 20 nm Au, rate 0.1-0.2 nm/s

Lift-off:

- cold acetone 6h or warm acetone (53 °C) 3h / acetone spray
- IPA rinse (30 s)
- N_2 (g) dry

Remarks:

- In the e-beam, the edge of a premade alignment marker is used to focus the beam. The marker is on the holder on which the sample is mounted. If this alignment marker is already degraded by focusing the beam from previous writing jobs, with much higher beam currents, the beam is focused only very poorly resulting in a large spot size. Using an uncontaminated alignment marker (also on the holder, or one on the sample) improved the yield for writing the fine gates and also makes the writing result much less sensitive to the exact chosen dose.
- In previous recipes, such as [19, 143], there was an extra 'Surface oxide removal' step after the development step. In my experience this actually damaged the PMMA-layer so I stopped using this step.

(f) **Large gates**

Preparation:

- acetone rinse (2 min)
- IPA rinse (30 s)
- N_2 (g) dry

Resist:

- first layer: 500 nm OEBR-1000 (200 cp), 3500 rpm (55 s). Note: you cannot put a filter on the syringe: the resist is too thick.
- bake on hot plate 175 °C (30 min)
- second layer: 2% wt PMMA 950K in anisole: 90 nm, 2000 rpm (55 s)
- bake on hot plate 175 °C (10 min)

Exposure:

- e-beam dose: 750 μC/cm^2
- spot size: 100 nm/ beam current: 200 nA

Developing:

- 1:3 MIBK / IPA (1 min)
- IPA stop (1 min)
- N_2 (g) dry

Evaporation:

- 50 nm Ti, rate: 0.1 nm/s
- 400 nm Au, rate: 0.1-0.2 nm/s

Lift-off:

- cold acetone 6h or warm acetone (53 °C) 3h / acetone spray
- IPA rinse (30 s)
- N_2 (g) dry

Remark:

- The used OEBR-1000 (200 cp) is already 13 years old so the required spinning speed is typically higher than specified.

B

FABRICATION RECIPE OF SPIRAL INDUCTORS

In this Appendix we summarize the fabrication recipe used to fabricate the NbTiN spiral inductors. This recipe has been developed together with J.C. van Oven.

(a) **Deposition with superAJA**[1]

- Temperature: 100 °C
- Ar flow: 50, N flow: 6
- Pressure: 2 mTorr
- Power: 300 W
- Pre-sputter: 60 s, sputter: 90 s, for ~100 nm thickness

(b) **Patterning with EBPG**

- Spin: SAL-601 at 1500 rpm
- Bake: 2 min at 90 °C
- Expose in EBPG with dose: 22 μC/cm^2
- Bake: 3 minutes at 110 °C
- Develop in MF322 for 7 min
- Rinse in water

(c) **Etching with Leybold F1**

- SF_6 flow: 54 (= 13.5 sccm)
- Pressure: 5.5 μbar

[1] With support from the Leo Kouwenhoven team.

- RF power: 60 W (~350 V)
- Etch for 5 min

(d) **Removing etch mask**

- Soak in PRS-3000 for 30 minutes at 70 °C
- Sonicate for 10 minutes at full power
- Transfer chip to acetone at 50 °C
- Sonicate for 3 minutes at full power
- Rinse in IPA
- Blow dry with N_2 gas

BIBLIOGRAPHY

[1] J. J. Thomson, *Cathode Rays,* Philosophical Magazine Series 5 **44**, 293 (1897).

[2] N. W. Ashcroft and N. D. Mermin, *Solid State Physics* (Saunders, New York, 1974).

[3] R. Feynman, *Simulating physics with computers,* International Journal of Theoretical Physics **21**, 467 (1982).

[4] P. W. Shor, *Algorithms for quantum computation: discrete logarithms and factoring,* in *Proc. 35nd Annual Symposium on Foundations of Computer Science* (1994) pp. 124–134.

[5] L. K. Grover, *A Fast Quantum Mechanical Algorithm for Database Search,* in *Proceedings of the Twenty-eighth Annual ACM Symposium on Theory of Computing*, STOC (ACM, New York, 1996) pp. 212–219.

[6] D. P. DiVincenzo, *The Physical Implementation of Quantum Computation,* Fortschritte der Physik **48**, 771 (2000).

[7] F. Jelezko, T. Gaebel, I. Popa, M. Domhan, A. Gruber, and J. Wrachtrup, *Observation of Coherent Oscillation of a Single Nuclear Spin and Realization of a Two-Qubit Conditional Quantum Gate,* Physical Review Letters **93**, 130501 (2004).

[8] L. DiCarlo, J. M. Chow, J. M. Gambetta, L. S. Bishop, B. R. Johnson, D. I. Schuster, J. Majer, A. Blais, L. Frunzio, S. M. Girvin, and R. J. Schoelkopf, *Demonstration of two-qubit algorithms with a superconducting quantum processor,* Nature **460**, 240 (2009).

[9] G. Brennen, C. Caves, P. Jessen, and I. Deutsch, *Quantum Logic Gates in Optical Lattices,* Physical Review Letters **82**, 1060 (1999).

[10] S. Gulde, M. Riebe, G. P. T. Lancaster, C. Becher, J. Eschner, H. Häffner, F. Schmidt-Kaler, I. L. Chuang, and R. Blatt, *Implementation of the Deutsch-Jozsa algorithm on an ion-trap quantum computer.* Nature **421**, 48 (2003).

[11] V. Mourik, K. Zuo, S. M. Frolov, S. R. Plissard, E. P. A. M. Bakkers, and L. P. Kouwenhoven, *Signatures of Majorana Fermions in Hybrid Superconductor-Semiconductor Nanowire Devices,* Science **336**, 1003 (2012).

[12] J. R. Petta, A. C. Johnson, C. M. Marcus, M. P. Hanson, and A. C. Gossard, *Manipulation of a single charge in a double quantum dot,* Physical Review Letters **93**, 186802 (2004).

[13] D. Loss and D. P. DiVincenzo, *Quantum computation with quantum dots,* Physical Review A **57**, 120 (1998).

[14] R. J. Warburton, *Single spins in self-assembled quantum dots,* Nature Materials **12**, 483 (2013).

[15] S. Nadj-Perge, S. M. Frolov, E. P. A. M. Bakkers, and L. P. Kouwenhoven, *Spin–orbit qubit in a semiconductor nanowire,* Nature **468**, 1084 (2010).

[16] Y. Hu, H. O. H. Churchill, D. J. Reilly, J. Xiang, C. M. Lieber, and C. M. Marcus, *A Ge/Si heterostructure nanowire-based double quantum dot with integrated charge sensor,* Nature Nanotechnology **2**, 622 (2007).

[17] G. A. Steele, G. Gotz, and L. P. Kouwenhoven, *Tunable few-electron double quantum dots and Klein tunnelling in ultraclean carbon nanotubes,* Nature Nanotechnology **4**, 363 (2009).

[18] F. Pei, E. A. Laird, G. A. Steele, and L. P. Kouwenhoven, *Valley–spin blockade and spin resonance in carbon nanotubes,* Nature Nanotechnology **7**, 630 (2012).

[19] F. Braakman, *Coherent Coupling of Qubits in Small Quantum Dot Arrays*, Ph.D. thesis, Delft University of Technology (2013).

[20] A. Staring, *Coulomb-Blockade Oscillations in Quantum Dots and Wires*, Ph.D. thesis, Technische Universiteit Eindhoven (1992).

[21] H. Grabert and M. H. Devoret, eds., *Single Charge Tunneling*, NATO ASI Series, Vol. 294 (Springer US, Boston, MA, 1992).

[22] W. G. van der Wiel, S. De Franceschi, J. M. Elzerman, T. Fujisawa, S. Tarucha, and L. P. Kouwenhoven, *Electron transport through double quantum dots,* Reviews of Modern Physics **75**, 1 (2002).

[23] C. H. Yang, A. Rossi, N. S. Lai, R. Leon, W. H. Lim, and A. S. Dzurak, *Charge state hysteresis in semiconductor quantum dots,* Applied Physics Letters **105**, 183505 (2014).

[24] L. P. Kouwenhoven, D. G. Austing, and S. Tarucha, *Few-electron quantum dots,* Reports on Progress in Physics **64**, 701 (2001).

[25] J. Kyriakidis, M. Pioro-Ladriere, M. Ciorga, A. S. Sachrajda, and P. Hawrylak, *Voltage-tunable singlet-triplet transition in lateral quantum dots,* Physical Review B **66**, 1 (2002).

[26] R. Hanson, L. P. Kouwenhoven, J. R. Petta, S. Tarucha, and L. M. K. Vandersypen, *Spins in few-electron quantum dots,* Reviews of Modern Physics **79**, 1217 (2007).

[27] G. Dresselhaus, *Spin-Orbit Coupling Effects in Zinc Blende Structures,* Physical Review **100**, 580 (1955).

[28] Y. A. Bychkov and E. Rashba, *Properties of a 2D electron gas with lifted spectral degeneracy,* JETP Lett. **39**, 78 (1984).

[29] K. C. Nowack, F. H. Koppens, Y. V. Nazarov, and L. M. K. Vandersypen, *Coherent control of a single electron spin with electric fields,* Science **318**, 1430 (2007).

[30] P. Scarlino, E. Kawakami, P. Stano, M. Shafiei, C. Reichl, W. Wegscheider, and L. Vandersypen, *Spin-Relaxation Anisotropy in a GaAs Quantum Dot,* Physical Review Letters **113**, 256802 (2014).

[31] A. V. Khaetskii and Y. V. Nazarov, *Spin relaxation in semiconductor quantum dots,* Physical Review B **61**, 12639 (2000).

[32] A. V. Khaetskii and Y. V. Nazarov, *Spin-flip transitions between Zeeman sublevels in semiconductor quantum dots,* Physical Review B **64**, 7 (2001).

[33] V. N. Golovach, A. Khaetskii, and D. Loss, *Phonon-induced decay of the electron spin in quantum dots,* Physical Review Letters **93**, 016601 (2004).

[34] A. Abragam, *The Principles of Nuclear Magnetism* (Oxford University Press, Oxford, 1961).

[35] D. Paget, G. Lampel, B. Sapoval, and V. I. Safarov, *Low field electron-nuclear spin coupling in gallium arsenide under optical pumping conditions,* Physical Review B **15**, 5780 (1977).

[36] A. V. Khaetskii, D. Loss, and L. Glazman, *Electron Spin Decoherence in Quantum Dots due to Interaction with Nuclei,* Physical Review Letters **88**, 186802 (2002).

[37] F. H. L. Koppens, K. C. Nowack, and L. M. K. Vandersypen, *Spin Echo of a Single Electron Spin in a Quantum Dot,* Physical Review Letters **100**, 236802 (2008).

[38] J. M. Taylor, J. R. Petta, A. C. Johnson, A. Yacoby, C. M. Marcus, and M. D. Lukin, *Relaxation, dephasing, and quantum control of electron spins in double quantum dots,* Physical Review B **76**, 35315 (2007).

[39] I. T. Vink, K. C. Nowack, F. H. L. Koppens, J. Danon, Y. V. Nazarov, and L. M. K. Vandersypen, *Locking electron spins into magnetic resonance by electron-nuclear feedback,* Nature Physics **5**, 764 (2009).

[40] H. Bluhm, S. Foletti, I. Neder, M. Rudner, D. Mahalu, V. Umansky, and A. Yacoby, *Dephasing time of GaAs electron-spin qubits coupled to a nuclear bath exceeding 200 μs,* Nature Physics **7**, 109 (2010).

[41] M. S. Rudner, L. M. K. Vandersypen, V. Vuletić, and L. S. Levitov, *Generating Entanglement and Squeezed States of Nuclear Spins in Quantum Dots,* Physical Review Letters **107**, 206806 (2011).

[42] M. Veldhorst, J. C. C. Hwang, C. H. Yang, A. W. Leenstra, B. de Ronde, J. P. Dehollain, J. T. Muhonen, F. E. Hudson, K. M. Itoh, A. Morello, and A. S. Dzurak, *An addressable quantum dot qubit with fault-tolerant control fidelity,* Nature Nanotechnology **9**, 981 (2014).

[43] E. Kawakami, P. Scarlino, D. R. Ward, F. R. Braakman, D. E. Savage, M. G. Lagally, M. Friesen, S. N. Coppersmith, M. A. Eriksson, and L. M. K. Vandersypen, *Electrical control of a long-lived spin qubit in a Si/SiGe quantum dot.* Nature Nanotechnology **9**, 666 (2014).

[44] H. Bluhm, S. Foletti, D. Mahalu, V. Umansky, and A. Yacoby, *Enhancing the Coherence of a Spin Qubit by Operating it as a Feedback Loop That Controls its Nuclear Spin Bath,* Physical Review Letters **105**, 216803 (2010).

[45] X. Wang, L. S. Bishop, J. Kestner, E. Barnes, K. Sun, and S. Das Sarma, *Composite pulses for robust universal control of singlet–triplet qubits,* Nature Communications **3**, 997 (2012).

[46] A. Barenco, C. H. Bennett, R. Cleve, D. P. DiVincenzo, N. Margolus, P. Shor, T. Sleator, J. A. Smolin, and H. Weinfurter, *Elementary gates for quantum computation,* Physical Review A **52**, 3457 (1995).

[47] J. M. Elzerman, R. Hanson, L. H. Willems Van Beveren, B. Witkamp, L. M. K. Vandersypen, and L. P. Kouwenhoven, *Single-shot read-out of an individual electron spin in a quantum dot,* Nature **430**, 431 (2004).

[48] K. Ono, D. G. Austing, Y. Tokura, and S. Tarucha, *Current rectification by Pauli exclusion in a weakly coupled double quantum dot system.* Science **297**, 1313 (2002).

[49] A. C. Johnson, J. R. Petta, J. M. Taylor, A. Yacoby, M. D. Lukin, C. M. Marcus, M. P. Hanson, and A. C. Gossard, *Triplet-singlet spin relaxation via nuclei in a double quantum dot.* Nature **435**, 925 (2005).

[50] F. H. L. Koppens, C. Buizert, I. T. Vink, K. C. Nowack, T. Meunier, L. P. Kouwenhoven, and L. M. K. Vandersypen, *Detection of single electron spin resonance in a double quantum dot,* Journal of Applied Physics **101**, 081706 (2007).

[51] C. Barthel, J. Medford, H. Bluhm, A. Yacoby, C. M. Marcus, M. P. Hanson, and A. C. Gossard, *Relaxation and readout visibility of a singlet-triplet qubit in an Overhauser field gradient,* Physical Review B **85**, 035306 (2012).

[52] M. Shafiei, *Electrical Control, Read-out and Initialization of Single Electron Spins*, Ph.D. thesis, Delft University of Technology (2013).

[53] K. C. Nowack, M. Shafiei, M. Laforest, G. E. D. K. Prawiroatmodjo, L. R. Schreiber, C. Reichl, W. Wegscheider, and L. M. K. Vandersypen, *Single-shot correlations and two-qubit gate of solid-state spins.* Science **333**, 1269 (2011).

[54] D. J. Reilly, C. M. Marcus, M. P. Hanson, and A. C. Gossard, *Fast single-charge sensing with a rf quantum point contact,* Applied Physics Letters **91**, 162101 (2007).

[55] R. J. Schoelkopf, P. Wahlgren, A. A. Kozhevnikov, P. Delsing, and D. E. Prober, *The Radio-Frequency Single-Electron Transistor (RF-SET): A Fast and Ultrasensitive Electrometer,* Science **280**, 1238 (1998).

[56] T. Müller, T. Choi, S. Hellmüller, K. Ensslin, T. Ihn, and S. Schön, *A circuit analysis of an in situ tunable radio-frequency quantum point contact,* Review of Scientific Instruments **84**, 083902 (2013).

[57] M. Steer, *Microwave and RF design* (Scitech publishing, 2009).

[58] S. Hellmueller, M. Pikulski, T. Mueller, B. Kueng, G. Puebla-Hellmann, A. Wallraff, M. Beck, K. Ensslin, and T. Ihn, *Optimization of sample-chip design for stub-matched radio-frequency reflectometry measurements,* Applied Physics Letters **101**, 042112 (2012).

[59] G. A. Prinz, *Spin-Polarized Transport,* Physics Today **48**, 58 (1995).

[60] S. A. Wolf, D. D. Awschalom, R. A. Buhrman, J. M. Daughton, S. von Molnár, M. L. Roukes, A. Y. Chtchelkanova, and D. M. Treger, *Spintronics: a spin-based electronics vision for the future.* Science **294**, 1488 (2001).

[61] I. Žutić, J. Fabian, and S. D. Sarma, *Spintronics: Fundamentals and applications,* Reviews of Modern Physics **76**, 323 (2004).

[62] *Spintronics insight,* Nature Materials **11**, 367 (2012).

[63] R. Hanson and D. D. Awschalom, *Coherent manipulation of single spins in semiconductors.* Nature **453**, 1043 (2008).

[64] J. M. Taylor, H. A. Engel, W. Dur, A. Yacoby, C. M. Marcus, P. Zoller, and M. D. Lukin, *Fault-tolerant architecture for quantum computation using electrically controlled semiconductor spins,* Nature Physics **1**, 177 (2005).

[65] W. S. Boyle and G. E. Smith, *Charge Coupled Semiconductor Devices,* Bell System Technical Journal **49**, 587 (1970).

[66] J. Kikkawa and D. Awschalom, *Lateral drag of spin coherence in gallium arsenide,* Nature **397**, 139 (1999).

[67] S. A. Crooker, M. Furis, X. Lou, C. Adelmann, D. L. Smith, C. J. Palmstrøm, and P. A. Crowell, *Imaging spin transport in lateral ferromagnet/semiconductor structures.* Science **309**, 2191 (2005).

[68] Y. Ono, A. Fujiwara, K. Nishiguchi, H. Inokawa, and Y. Takahashi, *Manipulation and detection of single electrons for future information processing,* Journal of Applied Physics **97**, 031101 (2005).

[69] R. P. G. McNeil, M. Kataoka, C. J. B. Ford, C. H. W. Barnes, D. Anderson, G. A. C. Jones, I. Farrer, and D. A. Ritchie, *On-demand single-electron transfer between distant quantum dots,* Nature **477**, 439 (2011).

[70] S. Hermelin, S. Takada, M. Yamamoto, S. Tarucha, A. D. Wieck, L. Saminadayar, C. Bauerle, and T. Meunier, *Electrons surfing on a sound wave as a platform for quantum optics with flying electrons,* Nature **477**, 435 (2011).

[71] S. B. Howell, *Handbook of CCD Astronomy* (Cambridge University Press, 2006).

[72] P. Barthelemy and L. M. K. Vandersypen, *Quantum Dot Systems: A versatile platform for quantum simulations,* Annalen der Physik **525**, 808 (2013).

[73] R. Vrijen and E. Yablonovitch, *A spin-coherent semiconductor photo-detector for quantum communication,* Physica E: Low-Dimensional Systems and Nanostructures **10**, 569 (2001).

[74] T. Fujita, H. Kiyama, K. Morimoto, S. Teraoka, G. Allison, A. Ludwig, A. D. Wieck, A. Oiwa, and S. Tarucha, *Nondestructive real-time measurement of charge and spin dynamics of photoelectrons in a double quantum dot,* Physical Review Letters **110**, 266803 (2013).

[75] C. Barthel, M. Kjærgaard, J. Medford, M. Stopa, C. M. Marcus, M. P. Hanson, and A. C. Gossard, *Fast sensing of double-dot charge arrangement and spin state with a radio-frequency sensor quantum dot,* Physical Review B **81**, 161308 (2010).

[76] M. Shafiei, K. Nowack, C. Reichl, W. Wegscheider, and L. Vandersypen, *Resolving Spin-Orbit- and Hyperfine-Mediated Electric Dipole Spin Resonance in a Quantum Dot,* Physical Review Letters **110**, 107601 (2013).

[77] J. Danon and Y. V. Nazarov, *Pauli spin blockade in the presence of strong spin-orbit coupling,* Physical Review B **80**, 041301 (2009).

[78] L. Schreiber, F. Braakman, T. Meunier, V. Calado, J. Danon, J. Taylor, W. Wegscheider, and L. Vandersypen, *Coupling artificial molecular spin states by photon-assisted tunnelling,* Nature Communications **2**, 556 (2011).

[79] J. I. Colless, A. C. Mahoney, J. M. Hornibrook, A. C. Doherty, H. Lu, A. C. Gossard, and D. J. Reilly, *Dispersive Readout of a Few-Electron Double Quantum Dot with Fast rf Gate Sensors,* Physical Review Letters **110**, 046805 (2013).

[80] M. D. Shulman, O. E. Dial, S. P. Harvey, H. Bluhm, V. Umansky, and A. Yacoby, *Demonstration of Entanglement of Electrostatically Coupled Singlet-Triplet Qubits,* Science **336**, 202 (2012).

[81] V. Srinivasa, K. C. Nowack, M. Shafiei, L. M. K. Vandersypen, and J. M. Taylor, *Simultaneous spin-charge relaxation in double quantum dots,* Physical Review Letters **110**, 196803 (2013).

[82] C. H. Yang, A. Rossi, R. Ruskov, N. S. Lai, F. A. Mohiyaddin, S. Lee, C. Tahan, G. Klimeck, A. Morello, and A. S. Dzurak, *Spin-valley lifetimes in a silicon quantum dot with tunable valley splitting,* Nature Communications **4**, 2069 (2013).

[83] C. B. Simmons, J. R. Prance, B. J. Van Bael, T. S. Koh, Z. Shi, D. E. Savage, M. G. Lagally, R. Joynt, M. Friesen, S. N. Coppersmith, and M. A. Eriksson, *Tunable spin loading and T1 of a silicon spin qubit measured by single-shot readout,* Physical Review Letters **106**, 156804 (2011).

[84] D. Kielpinski, C. Monroe, and D. J. Wineland, *Architecture for a large-scale ion-trap quantum computer.* Nature **417**, 709 (2002).

[85] A. R. Long, M. Pioro-Ladrière, J. H. Davies, A. S. Sachrajda, L. Gaudreau, P. Zawadzki, J. Lapointe, J. Gupta, Z. Wasilewski, and S. A. Studenikin, *The origin of switching noise in GaAs/AlGaAs lateral gated devices,* Physica E: Low-Dimensional Systems and Nanostructures **34**, 553 (2006).

[86] T. H. Oosterkamp, T. Fujisawa, W. G. van der Wiel, K. Ishibashi, R. V. Hijman, S. Tarucha, and L. P. Kouwenhoven, *Microwave spectroscopy of a quantum-dot molecule,* Nature **395**, 873 (1998).

[87] J. M. Elzerman, R. Hanson, L. H. Willems Van Beveren, L. M. K. Vandersypen, and L. P. Kouwenhoven, *Excited-state spectroscopy on a nearly closed quantum dot via charge detection,* Applied Physics Letters **84**, 4617 (2004).

[88] J. Majer, J. M. Chow, J. M. Gambetta, J. Koch, B. R. Johnson, J. A. Schreier, L. Frunzio, D. I. Schuster, A. A. Houck, A. Wallraff, A. Blais, M. H. Devoret, S. M. Girvin, and R. J. Schoelkopf, *Coupling superconducting qubits via a cavity bus.* Nature **449**, 443 (2007).

[89] M. A. Sillanpää, J. I. Park, and R. W. Simmonds, *Coherent quantum state storage and transfer between two phase qubits via a resonant cavity.* Nature **449**, 438 (2007).

[90] F. Schmidt-Kaler, H. Häffner, M. Riebe, S. Gulde, G. P. T. Lancaster, T. Deuschle, C. Becher, C. F. Roos, J. Eschner, and R. Blatt, *Realization of the Cirac-Zoller controlled-NOT quantum gate.* Nature **422**, 408 (2003).

[91] M. Veldhorst, C. H. Yang, J. C. C. Hwang, W. Huang, J. P. Dehollain, J. T. Muhonen, S. Simmons, A. Laucht, F. E. Hudson, K. M. Itoh, A. Morello, and A. S. Dzurak, *A two-qubit logic gate in silicon,* Nature **526**, 410 (2015).

[92] J. M. Taylor and M. D. Lukin, *Cavity quantum electrodynamics with semiconductor double-dot molecules on a chip,* (2006), arXiv:0605144 [cond-mat] .

[93] G. Burkard and A. Imamoglu, *Ultra-long-distance interaction between spin qubits,* Physical Review B **74**, 041307 (2006).

[94] X. Hu, Y. X. Liu, and F. Nori, *Strong coupling of a spin qubit to a superconducting stripline cavity,* Physical Review B **86**, 035314 (2012).

[95] M. J. A. Schuetz, E. M. Kessler, G. Giedke, L. M. K. Vandersypen, M. D. Lukin, and J. I. Cirac, *Universal quantum transducers based on surface acoustic waves,* Physical Review X **5**, 031031 (2015).

[96] L. Trifunovic, O. Dial, M. Trif, J. R. Wootton, R. Abebe, A. Yacoby, and D. Loss, *Long-Distance Spin-Spin Coupling via Floating Gates,* Physical Review X **2**, 011006 (2012).

[97] L. Trifunovic, F. L. Pedrocchi, and D. Loss, *Long-Distance Entanglement of Spin Qubits via Ferromagnet,* Physical Review X **3**, 041023 (2013).

[98] M. Friesen, A. Biswas, X. Hu, and D. Lidar, *Efficient Multiqubit Entanglement via a Spin Bus,* Physical Review Letters **98**, 230503 (2007).

[99] M. Leijnse and K. Flensberg, *Coupling Spin Qubits via Superconductors,* Physical Review Letters **111**, 060501 (2013).

[100] F. Hassler, G. Catelani, and H. Bluhm, *Exchange-interaction of two spin qubits mediated by a superconductor,* Physical Review B **92**, 235401 (2015).

[101] B. Trauzettel, D. V. Bulaev, D. Loss, and G. Burkard, *Spin qubits in graphene quantum dots,* Nature Physics **3**, 192 (2007).

[102] T. Frey, P. J. Leek, M. Beck, A. Blais, T. Ihn, K. Ensslin, and A. Wallraff, *Dipole coupling of a double quantum dot to a microwave resonator,* Physical Review Letters **108**, 046807 (2012).

[103] S. Mehl, H. Bluhm, and D. P. DiVincenzo, *Two-qubit couplings of singlet-triplet qubits mediated by one quantum state,* Physical Review B **90**, 045404 (2014).

[104] J. Lehmann, A. Gaita-Arino, E. Coronado, and D. Loss, *Spin qubits with electrically gated polyoxometalate molecules.* Nature Nanotechnology **2**, 312 (2007).

[105] P. Stano, J. Klinovaja, F. R. Braakman, L. M. K. Vandersypen, and D. Loss, *Fast long-distance control of spin qubits by photon-assisted cotunneling,* Physical Review B **92**, 075302 (2015).

[106] V. Srinivasa, H. Xu, and J. M. Taylor, *Tunable Spin-Qubit Coupling Mediated by a Multielectron Quantum Dot,* Physical Review Letters **114**, 226803 (2015).

[107] J. J. Viennot, M. C. Dartiailh, A. Cottet, and T. Kontos, *Coherent coupling of a single spin to microwave cavity photons,* Science **349**, 408 (2015).

[108] K. D. Petersson, L. W. McFaul, M. D. Schroer, M. Jung, J. M. Taylor, A. A. Houck, and J. R. Petta, *Circuit quantum electrodynamics with a spin qubit.* Nature **490**, 380 (2012).

[109] H. Kramers, *L'interaction Entre les Atomes Magnétogènes dans un Cristal Paramagnétique,* Physica **1**, 182 (1934).

[110] P. W. Anderson, *Antiferromagnetism. Theory of Superexchange Interaction,* Physical Review **79**, 350 (1950).

[111] C. Kim, P. J. White, Z.-X. Shen, T. Tohyama, Y. Shibata, S. Maekawa, B. O. Wells, Y. J. Kim, R. J. Birgeneau, and M. A. Kastner, *Systematics of the Photoemission Spectral Function of Cuprates: Insulators and Hole- and Electron-Doped Superconductors,* Physical Review Letters **80**, 4245 (1998).

[112] M. Kohno, *Spectral properties near the Mott transition in the two-dimensional Hubbard model with next-nearest-neighbor hopping,* Physical Review B **90**, 035111 (2014).

[113] B. Giese, J. Amaudrut, A. K. Köhler, M. Spormann, and S. Wessely, *Direct observation of hole transfer through DNA by hopping between adenine bases and by tunnelling.* Nature **412**, 318 (2001).

[114] F. Meinert, M. J. Mark, E. Kirilov, K. Lauber, P. Weinmann, M. Gröbner, A. J. Daley, and H.-C. Nägerl, *Quantum gases. Observation of many-body dynamics in long-range tunneling after a quantum quench.* Science **344**, 1259 (2014).

[115] R. Sánchez, G. Granger, L. Gaudreau, A. Kam, M. Pioro-Ladrière, S. A. Studenikin, P. Zawadzki, A. S. Sachrajda, and G. Platero, *Long-Range Spin Transfer in Triple Quantum Dots,* Physical Review Letters **112**, 176803 (2014).

[116] F. R. Braakman, P. Barthelemy, C. Reichl, W. Wegscheider, and L. M. K. Vandersypen, *Long-distance coherent coupling in a quantum dot array.* Nature Nanotechnology **8**, 432 (2013).

[117] T. A. Baart, M. Shafiei, T. Fujita, C. Reichl, W. Wegscheider, and L. M. K. Vandersypen, *Single-spin CCD,* Nature Nanotechnology **11**, 330 (2016).

[118] O. E. Dial, M. D. Shulman, S. P. Harvey, H. Bluhm, V. Umansky, and A. Yacoby, *Charge Noise Spectroscopy Using Coherent Exchange Oscillations in a Singlet-Triplet Qubit,* Physical Review Letters **110**, 146804 (2013).

[119] J. Medford, J. Beil, J. M. Taylor, S. D. Bartlett, A. C. Doherty, E. I. Rashba, D. P. Divincenzo, H. Lu, A. C. Gossard, and C. M. Marcus, *Self-consistent measurement and state tomography of an exchange-only spin qubit.* Nature Nanotechnology **8**, 654 (2013).

[120] F. A. Zwanenburg, A. S. Dzurak, A. Morello, M. Y. Simmons, L. C. L. Hollenberg, G. Klimeck, S. Rogge, S. N. Coppersmith, and M. A. Eriksson, *Silicon quantum electronics,* Reviews of Modern Physics **85**, 961 (2013).

[121] C. Kloeffel and D. Loss, *Prospects for Spin-Based Quantum Computing in Quantum Dots,* Annual Review of Condensed Matter Physics **4**, 51 (2013).

[122] J. R. Petta, A. C. Johnson, J. M. Taylor, E. A. Laird, A. Yacoby, M. D. Lukin, C. M. Marcus, M. P. Hanson, and A. C. Gossard, *Coherent Manipulation of Coupled Electron Spins in Semiconductor Quantum Dots,* Science **309**, 2180 (2005).

[123] H. O. H. Churchill, A. J. Bestwick, J. W. Harlow, F. Kuemmeth, D. Marcos, C. H. Stwertka, S. K. Watson, and C. M. Marcus, *Electron-nuclear interaction in 13C nanotube double quantum dots,* Nature Physics **5**, 321 (2008).

[124] Y.-Y. Liu, J. Stehlik, C. Eichler, M. J. Gullans, J. M. Taylor, and J. R. Petta, *Semiconductor double quantum dot micromaser,* Science **347**, 285 (2015).

[125] R. Thalineau, S. Hermelin, A. D. Wieck, C. Bäuerle, L. Saminadayar, and T. Meunier, *A few-electron quadruple quantum dot in a closed loop,* Applied Physics Letters **101**, 103102 (2012).

[126] T. Takakura, A. Noiri, T. Obata, T. Otsuka, J. Yoneda, K. Yoshida, and S. Tarucha, *Single to quadruple quantum dots with tunable tunnel couplings,* Applied Physics Letters **104**, 113109 (2014).

[127] J. Stehlik, Y.-Y. Liu, C. M. Quintana, C. Eichler, T. R. Hartke, and J. R. Petta, *Fast Charge Sensing of a Cavity-Coupled Double Quantum Dot Using a Josephson Parametric Amplifier,* Physical Review Applied **4**, 014018 (2015).

[128] *Python – Python Programming Language,* .

[129] E. Jones, T. Oliphant, P. Peterson, *et al.*, *SciPy: Open source scientific tools for Python,* (2001–), [Online; accessed 2015-04-14].

[130] Wikipedia, *Gabor filter — wikipedia, the free encyclopedia,* (2015), [Online; accessed 29-September-2015].

[131] J. G. Daugman, *Uncertainty relation for resolution in space, spatial frequency, and orientation optimized by two-dimensional visual cortical filters,* Journal of the Optical Society of America A **2**, 1160 (1985).

[132] B. Bertrand, S. Hermelin, S. Takada, M. Yamamoto, S. Tarucha, and A. Ludwig, *Long-range spin transfer using individual electrons,* (2015), arXiv:1508.04307 .

[133] K. Eng, T. D. Ladd, A. Smith, M. G. Borselli, A. A. Kiselev, B. H. Fong, K. S. Holabird, T. M. Hazard, B. Huang, P. W. Deelman, I. Milosavljevic, A. E. Schmitz, R. S. Ross, M. F. Gyure, and A. T. Hunter, *Isotopically enhanced triple-quantum-dot qubit,* Science Advances **1**, e1500214 (2015).

[134] S. Amasha, K. MacLean, I. P. Radu, D. M. Zumbühl, M. A. Kastner, M. P. Hanson, and A. C. Gossard, *Spin-dependent tunneling of single electrons into an empty quantum dot,* Physical Review B **78**, 41306 (2008).

[135] M. Busl, G. Granger, L. Gaudreau, R. Sanchez, A. Kam, M. Pioro-Ladriere, S. A. Studenikin, P. Zawadzki, Z. R. Wasilewski, A. S. Sachrajda, and G. Platero, *Bipolar spin blockade and coherent state superpositions in a triple quantum dot,* Nature Nanotechnology **8**, 261 (2013).

[136] L. P. Kouwenhoven, N. C. V. D. Vaart, A. T. Johnson, W. Kool, C. J. P. M. Harmans, J. G. Williamson, A. A. M. Staring, and C. T. Foxon, *Single electron charging effects in semiconductor quantum dots,* Zeitschrift fur Physik B Condensed Matter **85**, 367 (1991).

[137] M. R. Delbecq, T. Nakajima, P. Stano, T. Otsuka, S. Amaha, J. Yoneda, K. Takeda, G. Allison, A. Ludwig, A. D. Wieck, and S. Tarucha, *Quantum dephasing in a gated GaAs triple quantum dot due to non-ergodic noise,* Physical Review Letters **116**, 046802 (2016).

[138] M. Friesen, M. A. Eriksson, and S. N. Coppersmith, *Magnetic field dependence of valley splitting in realistic Si/SiGe quantum wells,* Applied Physics Letters **89**, 202106 (2006).

[139] A. G. Fowler, A. M. Stephens, and P. Groszkowski, *High-threshold universal quantum computation on the surface code,* Physical Review A **80**, 052312 (2009).

[140] M. Serina, L. Trifunovic, C. Kloeffel, and D. Loss, *Long-Range Interaction between Charge and Spin Qubits in Quantum Dots,* (2016), arXiv:1601.03564v1 .

[141] C. Echeverria-Arrondo and E. Y. Sherman, *Relaxation of flying spin qubits in quantum wires by hyperfine interaction,* Physical Review B **87**, 081410 (2013).

[142] Z. Shi, C. B. Simmons, J. R. Prance, J. K. Gamble, T. S. Koh, Y. P. Shim, X. Hu, D. E. Savage, M. G. Lagally, M. A. Eriksson, M. Friesen, and S. N. Coppersmith, *Fast hybrid silicon double-quantum-dot qubit,* Physical Review Letters **108**, 140503 (2012).

[143] K. C. Nowack, *Electrical manipulation and detection of single electron spins in quantum dots*, Ph.D. thesis, Delft University of Technology (2009).

CURRICULUM VITÆ

Timothy Alexander BAART

Born in Rotterdam, The Netherlands.

EDUCATION

Secondary School at the Wolfert van Borselen, Rotterdam.

2006–2009 BSc Physics (with distinction), Delft University of Technology

2009–2011 MSc Physics (with distinction), Delft University of Technology

Graduate research project in the group of prof. dr. J.M. van Ruitenbeek, Leiden University.
"Transition Voltage Spectroscopy and the Nature of Vacuum Tunneling"

Graduate research project in the group of prof. dr. M.D. Lukin, Harvard University.
"Measuring Brownian motion of MFM-tips & Characterizing mechanical properties of mono-crystalline diamond resonators"

Graduate research project in the group of prof. dr. ir. L.M.K. Vandersypen, Delft University of Technology.
"Quantum dots on bilayer graphene made on a substrate of boron nitride using spit gates"

2011–2016 PhD Research at Delft University of Technology
under supervision of prof. dr. ir. L.M.K. Vandersypen:
CCD operation and long-range coupling of spins in quantum dot arrays

LIST OF PUBLICATIONS

1. Nanosecond-timescale spin transfer using individual electrons in a quadruple-quantum-dot device
   T.A. Baart, N. Jovanovic, C. Reichl, W. Wegscheider and L.M.K. Vandersypen,
   Manuscript in preparation

2. *Coherent spin-exchange via a quantum mediator*
   T.A. Baart[*], T. Fujita[*], C. Reichl, W. Wegscheider and L.M.K. Vandersypen,
   Manuscript submitted, arXiv:1603.03433

3. *Computer-automated tuning of semiconductor double quantum dots into the single-electron regime*
   T.A. Baart, P.T. Eendebak, C. Reichl, W. Wegscheider and L.M.K. Vandersypen,
   Manuscript submitted, arXiv:1603.02274

4. *Quantum dot circuit and a method of operating*
   P.T. Eendebak, **T.A. Baart** and L.M.K. Vandersypen,
   Patent pending (European patent application No. 16158810.8)

5. *Single-spin CCD*
   T.A. Baart[*], M. Shafiei[*], T. Fujita, C. Reichl, W. Wegscheider and L.M.K. Vandersypen,
   Nature Nanotechnology **11**, 330-334 (2016)

6. *Gate-defined confinement in bilayer graphene-hexagonal boron nitride hybrid devices*
   A.M. Goossens, S.C.M. Driessen, **T.A. Baart**, K. Watanabe, T. Taniguchie and L.M.K. Vandersypen,
   Nano Letters **12**, 4656-4660 (2012)

7. *Transition voltage spectroscopy and the nature of vacuum tunneling*
   M.L. Trouwborst, C.A. Martin, R.H.M. Smit, C.M. Guédon, **T.A. Baart**, S.J. van der Molen and J.M. van Ruitenbeek,
   Nano Letters **11**, 614-617 (2011)

[*] These authors contributed equally to this work.